

Dark matter halos of galaxies studied with weak gravitational lensing

Dissertation
zur
Erlangung des Doktorgrades (Dr. rer. nat.)
der
Mathematisch-Naturwissenschaftlichen Fakultät
der
Rheinischen Friedrich-Wilhelms-Universität Bonn

vorgelegt von
MARTINA KLEINHEINRICH
aus
Rheda-Wiedenbrück

Bonn 2003

Angefertigt mit Genehmigung
der Mathematisch-Naturwissenschaftlichen Fakultät
der Rheinischen Friedrich-Wilhelms-Universität Bonn

1. Referent: Prof. Dr. P. Schneider
2. Referent: Prof. Dr. H.-W. Rix

Tag der Promotion:

Contents

1	Introduction	1
2	Galaxies	3
2.1	Classification of galaxies	3
2.2	Scaling relations	5
2.2.1	The Tully-Fisher relation	5
2.2.2	The Faber-Jackson relation	5
2.3	Dark matter	7
2.3.1	Dark matter in spiral galaxies	7
2.3.2	Dark matter in elliptical galaxies	7
2.3.3	Modified Newtonian dynamics	9
2.4	Current theory of galaxy formation and related open questions	10
2.5	Modeling of the density profiles of galaxies	11
2.5.1	Singular isothermal sphere	11
2.5.2	Truncated singular isothermal sphere	12
2.5.3	Navarro-Frenk-White profile	12
3	Gravitational lensing	19
3.1	General principles	19
3.2	Weak gravitational lensing	23
3.3	Lens models	26
3.3.1	Singular isothermal sphere	27
3.3.2	Truncated singular isothermal sphere	28
3.3.3	Navarro-Frenk-White halo	28
3.4	Galaxy-galaxy lensing	29
3.4.1	Theory	29
3.4.2	Methods to measure galaxy-galaxy lensing	32
4	Observations of dark matter halos of galaxies	35
4.1	Satellite dynamics	35
4.2	Galaxy-galaxy lensing	38
4.3	Summary on galaxy properties at large radii	44
4.4	COMBO-17 compared to previous studies	44

4.4.1	Lensing measurements in comparison to satellite dynamics	44
4.4.2	COMBO-17 in comparison to other lensing data sets	45
5	The COMBO-17 survey	47
5.1	Observations	47
5.2	Data reduction	49
5.2.1	Data reduction pipeline, part I: Image Processing	49
5.2.2	Data reduction pipeline, part II: Object detection and flux measurements	54
5.3	Multi-colour classification	57
5.3.1	The object libraries	57
5.3.2	Template fitting	60
5.4	Resulting object catalogs	61
5.5	Contribution to COMBO-17 from this thesis	62
6	Shape measurements of faint objects	65
6.1	Proper sumframes for shape measurements and object detection	66
6.2	Measuring and correcting shapes of faint objects	67
6.3	The reliability of shape measurements	72
6.3.1	The data	73
6.3.2	Influence of exposure time and seeing	75
6.3.3	Scatter in the shape measurements between all independent sumframes	76
6.3.4	Shape measurements from the deep sumframe	78
6.3.5	Galaxy-galaxy lensing measured from the different sumframes	81
6.3.6	Summary	87
7	Galaxy-galaxy lensing measurements from COMBO-17	91
7.1	Detection of a galaxy-galaxy lensing signal	91
7.1.1	Measurement of $\langle \epsilon_t(\theta) \rangle$	94
7.1.2	Tests of the galaxy-galaxy lensing signal	95
7.2	Quantitative measurements of galaxy-galaxy lensing	98
7.2.1	Combined object catalogs from COMBO-17 and shape catalogs	98
7.2.2	The measurement	101
7.2.3	Influence of foreground galaxy clusters in the fields	105
7.2.4	Fitting the SIS model with σ_* and η	106
7.2.5	Using the SIS model to constrain the radial profile	109
7.2.6	Fitting the truncated SIS model	114
7.2.7	Fitting the NFW profile	117
7.2.8	Mass estimates and comparison of the models	120
7.2.9	Summary	122
8	Outlook	125

<i>CONTENTS</i>	III
Bibliography	129
Acknowledgements	137
Zusammenfassung	139
Lebenslauf	143

Chapter 1

Introduction

The main goal of this thesis is to investigate the dark matter halos of galaxies. Current theories of galaxy formation predict that galaxies are embedded in large dark matter halos with much larger extents than the visible parts of the galaxies. Testing this prediction from observations is challenging because – by definition – the dark matter halos do not emit any radiation. Therefore, they can only be studied using gravity. Only two methods are currently known to perform such studies on scales of $100h^{-1}$ kpc or more – satellite galaxy dynamics and weak gravitational lensing. These large scales are interesting because simulations show that dark matter halos of galaxies have sizes of some hundred kpc. Further, at such large scales, the gravitational effect from the luminous matter in the galaxies becomes unimportant so that it is possible to study just the dark matter density profile.

We choose weak gravitational lensing for our studies. The method is also known as *galaxy-galaxy lensing*. Lensing has the advantage over satellite studies that no assumptions concerning the dynamical state of the galaxies have to be made but that the dark matter distribution can be probed directly. However, galaxy-galaxy lensing puts strong requirements on the data so that it was detected first only in 1996. We will use data from the COMBO-17 survey¹ which is ideally suited for this kind of investigation. The most important advantage of COMBO-17 is that it combines deep observations with a large field-of-view. This will eventually allow us to study lens galaxies at redshifts around $z = 0.5$ in four fields adding up to 1 square degree total area. However, only half the area is used here. Additionally, COMBO-17 provides us with photometric redshifts from a total of 17 optical filters that also give spectral classification of the galaxies. Very deep *R*-band observations at the best seeing conditions are used for measuring shapes of source galaxies accurately. This special data set is the first deep data set from a representative part of the sky that is suitable for lensing studies and that also gives redshift and spectral information. So far, this kind of information has been available only for shallow surveys. Therefore, we will be able to extend existing studies of the local population of lens galaxies to higher redshifts. The most interesting questions in these studies concern not only the density profiles of dark matter halos of galaxies but also the connection between the luminous parts of galaxies

¹Classifying Objects by Medium-Band Observations in 17 filters

and their dark matter halos. We will investigate how the dark matter halos depend on luminosity and spectral type of the galaxies.

In weak lensing studies, shapes of source galaxies have to be measured accurately. Usually, these galaxies are small and cover only a few pixels on the CCD images. Further, they are distorted by e.g. defocussing, guiding errors and, most important for ground-based observations, the atmosphere. Special software is available to correct for these distortions. However, so far it has not been tested on observational data how well the corrections work and if galaxy shapes can be recovered reliably. We will use multiple observations from one of the COMBO-17 fields to compare the shape measurements from independent sumframes and thus test the reliability of shape measurements.

The thesis is organized as follows: In Chapt. 2 we give an overview over the basic properties of galaxies and their dark matter halos. In Sect. 2.4 we review briefly the current ideas on galaxy formation and related observational challenges. Further, we present in that Chapter the most important density profiles which are typically used to fit the density distributions. Chapter 3 deals with gravitational lensing. After a general introduction to lensing and in particular to weak gravitational lensing, we derive the shear for the density distributions introduced in Chapt. 2. Then, the theory of galaxy-galaxy lensing is summarized.

Chapter 4 gives an overview of previous results on dark matter halos of galaxies which are derived from satellite studies and galaxy-galaxy lensing. At the end of the Chapter, we will introduce briefly the COMBO-17 data set and explain its strength for galaxy-galaxy lensing studies. The survey will then be described in detail in Chapt. 5.

Our results are given in the next two Chapters. In Chapt. 6 we present our measurements of shapes of galaxies as well as our investigation of the reliability of these measurements. The galaxy-galaxy lensing analysis with its results then follows in Chapt. 7. The thesis ends with an outlook in Chapt. 8.

Chapter 2

Galaxies

In this Chapter the basic properties of galaxies are summarized, as far as they are needed for this thesis. First, in Sect. 2.1, the different morphological types of galaxies and their classification are described. In Sect. 2.2 the Tully-Fisher and Faber-Jackson relations are introduced which provide an important link between the mass and luminosity of galaxies. Section 2.3 deals with dark matter which is a basic ingredient of the current theory of galaxy formation. This theory of galaxy formation by hierarchical clustering is presented in Sect. 2.4. That Section also raises some still open questions that are a motivation for this thesis. Finally, in Sect. 2.5, some models that are used to parametrize galaxies and their dark matter distributions are described.

2.1 Classification of galaxies

Galaxies are fundamental building blocks in the Universe. On the one hand they are huge accumulations of stars, gas and dust while on the other hand galaxies themselves form groups or large clusters of galaxies. Their extragalactic nature was established in 1923 by Edwin Hubble. Galaxies come in a large variety of types and sizes. From their optical appearance they are classified into elliptical galaxies, spiral galaxies or irregular galaxies according to Hubble's *tuning-fork diagram* (Fig. 2.1). Galaxies with a smooth brightness distribution and elliptical appearance are classified as *elliptical galaxies* E0 to E7 where the number is 10 times the ellipticity $1 - b/a$ with a the major axis and b the minor axis. Galaxies with a disk-like structure and spiral arms are called *spiral galaxies* S; those that have also a bar are called *barred spirals* SB. Spiral galaxies have also a spheroidal component in the center, the *bulge*. According to the resolution into stars, the tightness of the spiral arms and the size of the bulge or bar relative to the disk, subclasses Sa, Sb, Sc and Sd are defined. From Sa to Sd the spiral arms become more resolved into stars and wider while the bulge or bar becomes less prominent. Intermediate between ellipticals and spirals are the S0 or *lenticular galaxies*. They consist of a disk and a bulge but without spiral arms. Finally, galaxies without dominating nuclei or rotational symmetry are classified as *irregular galaxies*. Elliptical and S0 galaxies are also called *early-type* galaxies while spiral

and irregular galaxies are called *late-type* galaxies. However, these terms do not refer to ages of the galaxies or evolutionary stages in galaxy evolution (e.g. Longair, 1998).

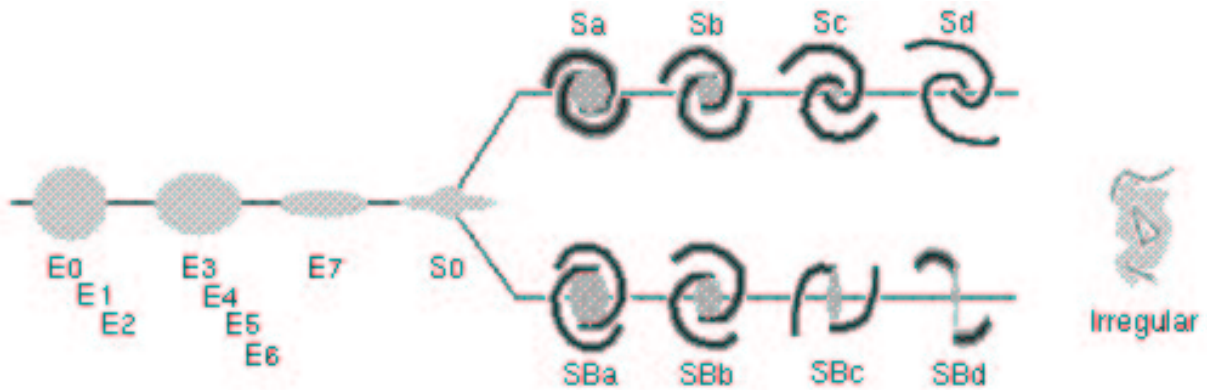


Figure 2.1: Hubble's tuning-fork diagram of galaxies. This classification is purely based on the morphology of galaxies. The picture is taken from the webpage <http://www.astronomynotes.com/galaxy/s3.htm> created by Nick Strobel.

The Hubble classification only refers to the morphology of galaxies and was originally set up for 'normal' galaxies like the Milky Way in contrast to dwarf or giant galaxies which can nonetheless be classified according to the same scheme. So within the same Hubble type a large range in sizes or magnitudes can be observed. For elliptical and S0 galaxies the diameters D_{25} range from 0.1 to 1000 kpc from dwarf to giant galaxies. D_{25} is just twice the radius at which a surface-brightness level of 25 mag arcsec⁻² in B is reached. In absolute B-magnitudes M_B these galaxies range from -8 to -25 . Spiral and irregular galaxies range from $D_{25} = 0.5$ kpc to $D_{25} = 100$ kpc and in M_B from -13 to -23 (Carroll and Ostlie, 1996).

We will later distinguish galaxies of different Hubble types and try to derive a relation between the properties of the dark matter halo and the galaxy type. The dark matter halo is a further component of galaxies that is not associated with light emission and does therefore not play a role in the morphological classification. In Sect. 2.3 we will present evidence for its existence. In our later investigation we will not use a morphological definition of the different galaxy types as presented here but one based on spectral properties of the galaxies, instead. The spectral types of galaxies are defined from averaged spectra of elliptical, S0 and spiral galaxies but additionally a class of *starburst galaxies* with special spectral features is introduced. The motivation for a spectral classification is that a morphological classification is not possible for very small and faint galaxies. The spectral classification will be introduced in Chapt. 5.

2.2 Scaling relations

Empirically, relations between the dynamics within a galaxy and its luminosity have been established. For relaxed galaxies, the dynamics are closely related to the mass distribution regardless of the nature of matter, visible or not. Therefore, such scaling relations are an important tool to study the distribution of dark matter in galaxies, especially when regions are probed where the dark matter halo is the dominating component which we will do in our analysis.

2.2.1 The Tully-Fisher relation

For spiral galaxies, Tully and Fisher (1977) introduced the now so-called *Tully-Fisher relation*

$$L \propto (\Delta v)^\alpha \quad (2.1)$$

where Δv is the width of the 21-cm line of neutral hydrogen and L the luminosity of the galaxy. Both, Δv and L , are corrected for the inclination of the galaxy. The linewidth is due to the rotation of the galaxy because at the approaching side of the disk the 21-cm line is blueshifted while at the receding side it is redshifted. Often the Tully-Fisher relation is given as a relation between absolute magnitude M and linewidth Δv . Equation (2.1) is equivalent to

$$M = -\frac{5}{2}\alpha \log \Delta v + \text{const} . \quad (2.2)$$

Figure 2.2 shows the correlation between linewidth and absolute magnitude.

$\alpha \approx 4$ is typically quoted in the literature. The relation is somewhat dependent on the type of spiral galaxies and on the waveband in which the luminosity is measured. For infrared luminosities, Aaronson and Mould (1983) find a slope corresponding to $\alpha = 4.8$, but $\alpha = 3.5$ when luminosities are measured in B. The scatter in the relation is reduced in the infrared. A small type dependence of α seems to exist only when using optical luminosities. Then, early-type spirals have a smaller α than late-type spirals. However, using the infrared, no clear type dependence is found (Aaronson and Mould, 1983; Carroll and Ostlie, 1996).

2.2.2 The Faber-Jackson relation

For elliptical galaxies, a relation similar to the Tully-Fisher relation holds, the *Faber-Jackson relation* introduced by Faber and Jackson (1976)

$$L \propto \sigma^\alpha \quad (2.3)$$

where σ is the central velocity dispersion of the galaxy. Just as for the Tully-Fisher relation, $\alpha \approx 4$, but values ranging from 3 to 5 can be found in the literature (Longair, 1998). In terms of magnitudes, Eq. (2.3) is equivalent to

$$M = -\frac{5}{2}\alpha \log \sigma + \text{const} . \quad (2.4)$$

Figure 2.2 illustrates the Faber-Jackson relation.

Later it has been found that the scatter in the Faber-Jackson relation can be reduced by introducing the effective radius r_e that encloses half of the light as additional parameter. Early-type galaxies are only found on the so-called *Fundamental Plane* within this three-parameter space. However, for our purposes, the Faber-Jackson relation will be sufficient. Using the Faber-Jackson relation instead of the Fundamental Plane has the further advantage that we can use very similar relations for early- and late-type galaxies. In spiral galaxies the linewidth Δv corresponds to a rotation velocity v_{rot} . Observations show that the rotation curves are flat (see Sect. 2.3.1) so that the rotation velocity can be related to a velocity dispersion by $\sigma_v = v_{\text{rot}}/\sqrt{2}$. Because α has very similar values in Eqs. (2.1) and (2.3) we can use $L \propto \sigma_v^\alpha$ for all galaxies, but we will also investigate the dependence of α on galaxy type.

The Tully-Fisher and Faber-Jackson relations have been derived from the luminous parts of the galaxies. Therefore, they are only known on scales of a few tenth of kpc and it is not known if these relations also hold on larger scales of hundreds of kpc. This will be investigated in this thesis. The origin of both relations has to be explained by theories of galaxy formation and evolution, especially if they should also hold on large scales.

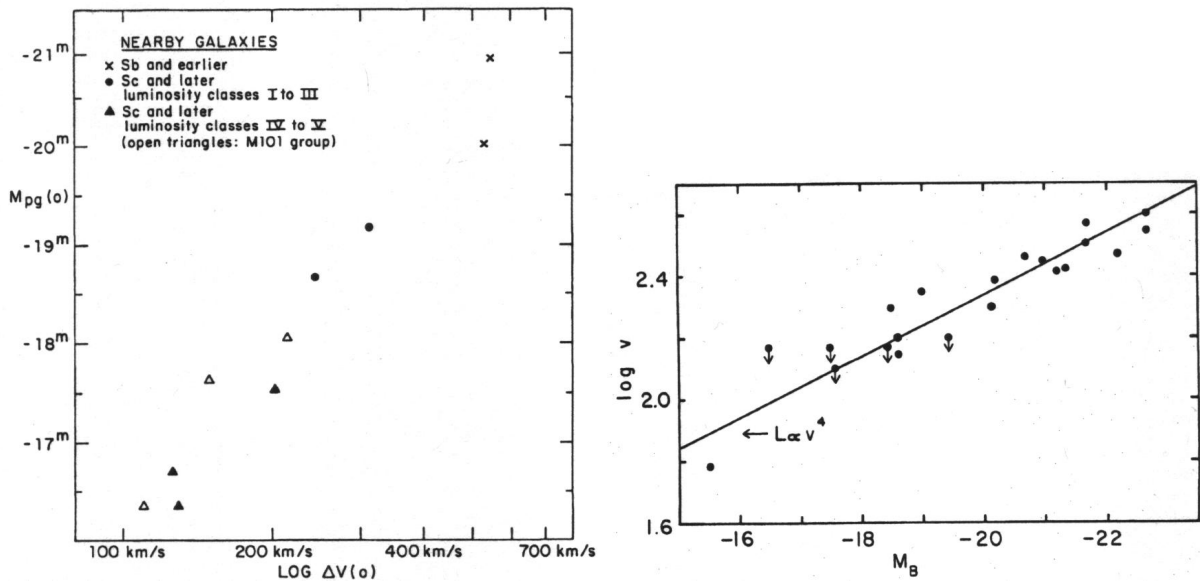


Figure 2.2: Left panel: Tully-Fisher relation for spiral galaxies; shown is the relation between HI linewidth and absolute magnitude; Figure taken from Tully and Fisher (1977). Right panel: Faber-Jackson relation for early-type galaxies; shown is the relation between absolute magnitude and line-of-sight velocity dispersion; Figure taken from Faber and Jackson (1976).

2.3 Dark matter

There is evidence that most – if not all – galaxies do not just consist of their luminous parts but are embedded in dark matter halos. The notation *dark matter* is due to the fact that this matter has not been detected by its radiation but only by its gravitational potential. In Sect. 2.3.1 and Sect. 2.3.2 the evidence for dark matter in spiral and elliptical galaxies is presented. Then, in Sect. 2.3.3, an alternative explanation for the findings that led to the postulate of dark matter is given.

2.3.1 Dark matter in spiral galaxies

Rotation curves of spiral galaxies provide the most striking evidence for dark matter around individual galaxies. From the dynamics of luminous tracers like stars, HI gas or HII regions at different distances from the center, the rotation velocity as function of radius can be obtained. The expectation is that beyond the optical parts of the galaxy the rotation curve should decline with $r^{-0.5}$ if one assumes that no significant amount of matter lies outside the visible parts of the galaxy. However, the surprising result is that for most spiral galaxies the rotation curves rise in the innermost parts and then essentially stay flat. Most striking are HI observations which are possible out to radii much larger than the extent of the stellar disk, out to about 30 kpc, see Fig. 2.3 (Sofue and Rubin, 2001; Bertin, 2000). Already before the observation of rotation curves, theoretical arguments were used in the 1970s to postulate the existence of massive halos around spiral galaxies (Bertin, 2000). Analytic calculations and numerical simulations had shown that disks would not be stable but would form a bar if the mass distribution in the galaxies followed the light distribution. The presence of a massive halo on the other hand was found to stabilize the disk against bar formation. Because at that time in the majority of spirals no bars were found this was interpreted as argument in favour of massive halos. Although today more and more bars are found in spiral galaxies, the existence of dark matter halos is well established now from the rotation curves.

2.3.2 Dark matter in elliptical galaxies

Elliptical galaxies are dynamically more complicated systems than spiral galaxies. Unlike spirals, they do not have a dominant disk in which stars and gas rotate on almost circular orbits, but consist of stars on highly noncircular orbits. Because the amount of anisotropy in these orbits is not known and because only the radial velocity component of individual tracers or the overall velocity dispersion can be measured, the modeling of elliptical galaxies requires in general more parameters than that of spirals. Additionally, individual tracers like gas clouds are rare in ellipticals. Therefore, it has taken longer for ellipticals than spirals to establish the existence of dark matter halos.

For ellipticals, a larger variety of methods is available to investigate the mass distribution than in spirals, see e.g. Danziger (1997). However, not all of these methods are applicable to any galaxy. Some galaxies contain gas, e.g. neutral hydrogen, that can be used similarly

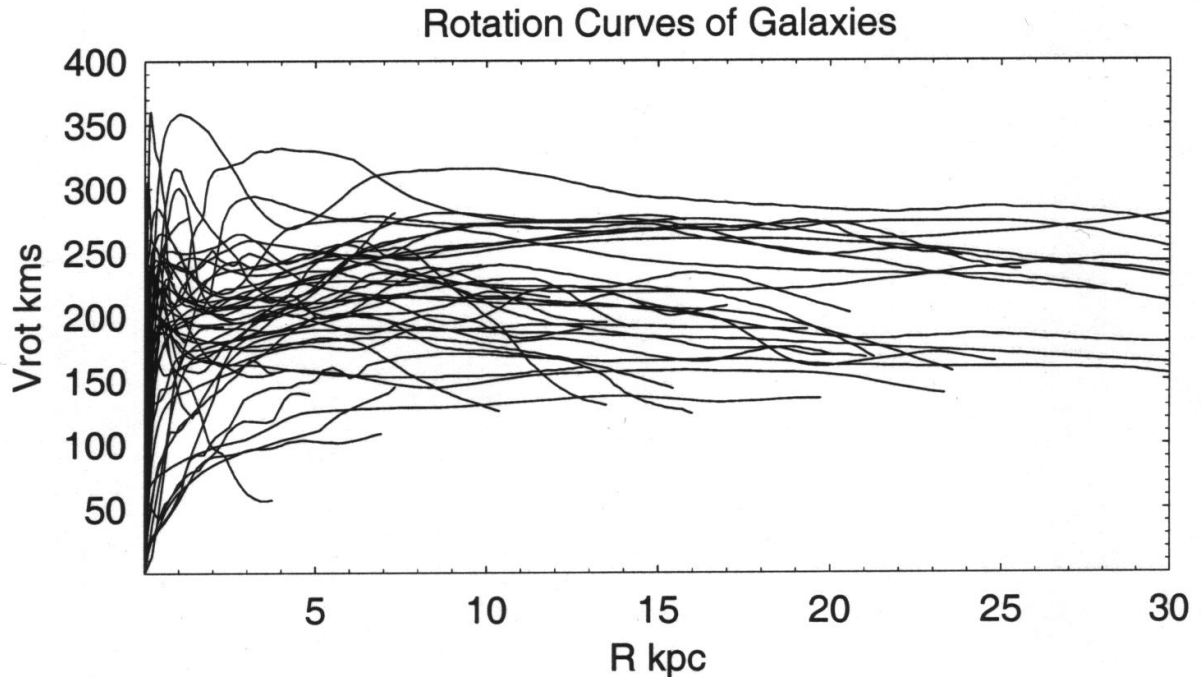


Figure 2.3: Rotation curves of Sb and Sc galaxies measured from CO, H α and HI data. Figure taken from Sofue et al. (1999).

to that in spirals for dynamical studies. However, more important as tracer is hot gas in some ellipticals that is X-ray luminous. Like in galaxy clusters, the density and temperature gradient of this hot gas can be used to constrain the mass profile. In some galaxies, the dynamics of planetary nebulae or globular clusters but also of individual stars have been used. The integrated stellar velocity profile from the whole stellar population can also be used. Further, the statistics of gravitationally lensed quasars have been applied to put constraints on the mass models of early-type galaxies.

Application of the various methods has led to independent evidence for dark matter halos in elliptical galaxies. Although in several cases the uncertainties in the modeling do not allow one to firmly establish the existence of dark matter in these galaxies, these galaxies are typically consistent with dark matter halos or even better fitted by models requiring dark matter than by constant mass-to-light ratios which would indicate that no extended dark matter halos are required. Further, if constant mass-to-light ratios are consistent with the data, these are often too high to be accounted for by normal stellar populations and thus also hint at the existence of dark matter. Stronger evidence comes from those elliptical galaxies for which constant mass-to-light ratios can indeed be ruled out (e.g. Rix et al., 1997; Kronawitter et al., 2000; Bertin, 2000). The lensing statistics of quasars have also shown that elliptical galaxies must be embedded in dark matter halos (Maoz and Rix,

1993). From the existence of dark matter halos in spiral galaxies it is further not surprising to find them also in ellipticals because it is generally believed that elliptical galaxies form from mergers of spiral galaxies.

Additional evidence for extended dark matter halos of spiral and elliptical galaxies comes from the study of the dynamics of satellite galaxies and from weak gravitational lensing. Both methods probe the dark matter halos at large distances of hundreds of kpc. Because this is the scale we want to probe here, we will summarize in more detail in Chapter 4 what is already known about dark matter halos on these larger scales.

2.3.3 Modified Newtonian dynamics

Dark matter is believed to amount to about 90% of the total matter content in the Universe. From Big Bang nucleosynthesis it is known that dark matter cannot be baryonic so it cannot just be made of faint stars like white dwarfs or neutron stars or of diffuse gas. Its presence is not only required in the outer parts of galaxies but also around galaxy clusters. Although the evidence for a substantial fraction of dark matter is several decades old now, its nature remains mysterious. This has led to the alternative theory that flat rotation curves are not due to the presence of dark matter but that the law of gravity is wrong for small accelerations as they are found in the outer parts of galaxies. Milgrom (1983a,b,c) proposed a theory of Modified Newtonian Dynamics (MOND) in which the Newtonian gravitational acceleration is changed for small accelerations. This theory is reviewed by Sanders and McGaugh (2002). The gravitational acceleration predicted by MOND is given by

$$g_{\text{MOND}} = \begin{cases} g_{\text{N}} & \text{for } g_{\text{N}} \gg a_0 \\ \sqrt{g_{\text{N}} a_0} & \text{for } g_{\text{N}} \ll a_0 \end{cases}, \quad (2.5)$$

where g_{N} denotes the Newtonian acceleration and g_{MOND} the acceleration in MOND. a_0 is a characteristic acceleration.

From Eq. (2.5) one can derive

$$v_{\text{rot}}^4 = GM a_0 \quad \text{for } g_{\text{N}} \ll a_0, \quad (2.6)$$

which shows that rotation curves must become asymptotically flat in MOND. This is just how the modification was made. Secondly, the modification was introduced such that the Tully-Fisher relation is reproduced with a slope of $\alpha = 4$ for all galaxies. In fact, Eq. (2.6) shows that strictly speaking only

$$M \propto v_{\text{rot}}^4 \quad (2.7)$$

is required. Therefore, MOND can be tested by measuring rotation curves and by investigating the mass-velocity relation (2.7).

Adopting some mass-to-light ratio, Eq. (2.6) can be converted into a relation between the luminosity and rotation velocity that can in turn be compared to the observed Tully-Fisher relation. Such comparison yields $a_0 \approx 10^{-8} \text{cm s}^{-1}$.

We will not be able to directly apply MOND to our analysis. This is because gravitational lensing is a prediction from General Relativity rather than from Newton's theory of gravity.

Therefore, one needs a modification of General Relativity with MOND as weak-field limit to derive a theory of gravitational light deflection in MOND. Currently, no such generalization is available. Therefore, we will stick to the framework of Newtonian physics and General Relativity and interpret our findings as results on dark matter halos of galaxies.

2.4 Current theory of galaxy formation and related open questions

Since the first detection of dark matter in the 1930's by Zwicky from observations of the velocities of galaxies within clusters, it has become clear in the last decades that dark matter is actually the dominating matter component in the Universe, at least on scales above a few tenth of kiloparsec. Therefore, dark matter must play a dominant role in structure formation. The picture of hierarchical clustering in a cold dark matter (CDM) Universe has today become the favorite picture. In this picture, dark matter consists of cold particles, that means of particles with nonrelativistic velocities. Structures form first on small scales, and from mergers of smaller mass clumps larger structures like big galaxies or galaxy clusters are formed. The opposite idea would be to have hot dark matter where the particles have relativistic velocities, and a Universe in which large structures form first and then fragment into smaller mass clumps. Observations of e.g. the clustering properties of galaxies highly favour the CDM picture and hierarchical clustering (e.g. Peacock et al., 2001).

Despite its successes, the CDM picture also has to face challenges from contradicting observations. These observations refer to the distribution of dark matter on galactic scales. One problem is known as *satellite problem*: CDM simulations predict a larger number of satellites to galaxies like the Milky Way than are observed (e.g. Moore et al., 1999). Further, the distribution of satellites in the simulations extends further inwards than in observations. A potential solution is that these satellites indeed exist but do not contain baryons or have at least not been able to form stars. In that case these satellites are basically invisible. However, satellites of galaxies that act as strong lenses and thus produce multiple images of background quasars, would behave as additional lenses and cause the so-called *microlensing* that can change the flux ratios between the quasar images in a way that cannot be understood from simple lens models without substructure. Thus, satellites should be detectable with strong lensing (e.g. Mao and Schneider, 1998).

A second problem is the *cusp problem*: In the central parts of low-surface brightness (LSB) galaxies, the density profiles do not agree with those found from CDM simulations but agree much better with isothermal profiles (see Sect. 2.5.1). CDM simulations have shown that structures on very different mass scales can be equally well fit by a universal density profile, the so-called Navarro-Frenk-White or NFW profile (Navarro et al., 1995, 1996, 1997), see also Sect. 2.5.3. Because LSB galaxies are dominated by dark matter, the expectation was that their density profiles should be well reproduced by the CDM simulations. However, observations of these galaxies are difficult and thus the derived density profiles are quite

uncertain. Some debate is going on whether observational biases in the derivation of the density profiles can reconcile the observed profiles with the NFW profile or not (Swaters et al., 2003; de Blok et al., 2003).

Also on larger scales, it turns out to be extremely difficult to test the NFW profile observationally. The reason is that differences from the isothermal profile become – apart from the central regions - only visible at large scales at which it is difficult to probe the potential of galaxies and clusters. Weak gravitational lensing has been used in recent years to try to distinguish these two profile for galaxy clusters (e.g. Clowe and Schneider, 2002). For galaxies, the derivation of a density profile is even harder due to their smaller mass. Therefore, for galaxies, attempts to determine the density profile have just started and will also be pursued in this work.

2.5 Modeling of the density profiles of galaxies

There is quite some debate on how density profiles of galaxies can be best parametrized. The observation of flat rotation curves has led to the conclusion that dark matter halos of galaxies are isothermal. Therefore, they are generally described by the *singular isothermal sphere* (SIS) (see Sect. 2.5.1) which is an especially simple model because it has only one parameter. Several modifications have been proposed to allow for deviations from an isothermal profile at small or large radii. Because we are interested in the properties of dark matter halos at large radii we will only mention modifications related to the outer parts of the profile, see Sect. 2.5.2. In simulations of dark matter halos, however, the NFW profile instead of the SIS has been found as good description of the data. The debate about the correct density profile is far from being settled and, indeed, we will try to constrain the density profile of dark matter halos in this thesis.

All mass models described here have circular symmetry. Although it is quite likely that dark matter halos are not circular but rather elliptical as can be seen from dark matter simulations, mass models without circular symmetry are often not considered. This is because studies of the density profiles of galaxies at large scales are not yet sensitive enough to consider more complicated models, see also Chapt. 4.

2.5.1 Singular isothermal sphere

For the SIS, the density profile is given by

$$\rho(r) = \frac{v_{\text{rot}}^2}{4\pi G} \frac{1}{r^2}, \quad (2.8)$$

where v_{rot} is the rotation velocity. That the rotation curve is indeed flat can be derived from Eq. (2.8) by

$$v_{\text{rot}}^2(R) = \frac{GM(r \leq R)}{R} \quad (2.9)$$

using

$$M(r \leq R) = \int_0^R 4\pi r^2 \rho(r) dr = \frac{v_{\text{rot}}^2 R}{G}. \quad (2.10)$$

The mass of the SIS rises linearly with radius and is thus infinite, $M(r \leq R) \rightarrow \infty$ for $R \rightarrow \infty$.

2.5.2 Truncated singular isothermal sphere

We will use the model of a truncated isothermal sphere introduced by Brainerd et al. (1996). This model has a mass distribution of the form

$$\rho(r) = \frac{v_0^2 s^2}{4\pi G r^2 (r^2 + s^2)}, \quad (2.11)$$

where s is an outer scale. By v_0 we denote the rotation velocity of a corresponding SIS which for the truncated SIS is the central rotation velocity. The density depends on radius in the following way

$$\rho(r) \propto \begin{cases} r^{-2} & \text{for } r \ll s \\ r^{-4} & \text{for } r \gg s \end{cases}. \quad (2.12)$$

For $s \rightarrow \infty$ the truncated isothermal sphere becomes the SIS. The mass inside an aperture is given by

$$M(r \leq R) = \frac{v_0^2 s}{G} \arctan \frac{R}{s}. \quad (2.13)$$

For $R \rightarrow \infty$ one gets the total mass which is finite

$$M(R \rightarrow \infty) = \frac{\pi v_0^2 s}{2G}. \quad (2.14)$$

Using Eqs. (2.9) and (2.13) one can calculate the rotation velocity

$$v_{\text{rot}}^2(R) = v_0^2 \frac{\arctan(R/s)}{R/s}. \quad (2.15)$$

Figure 2.4 shows the density profile $\rho(R)$, aperture mass $M(r \leq R)$ and rotation velocity $v_{\text{rot}}(R)$ for the SIS model and the truncated SIS with different values of s .

2.5.3 Navarro-Frenk-White profile

Navarro et al. (1996, 1997) have used N-body simulations of dark matter particles to study the density profiles of halos over a large mass range. They found a universal, spherically averaged profile that fits all halos equally well. This is the so-called Navarro-Frenk-White profile or NFW profile. It is given by

$$\rho(r) = \frac{\delta_c \rho_m}{(r/r_s)(1 + r/r_s)^2}, \quad (2.16)$$

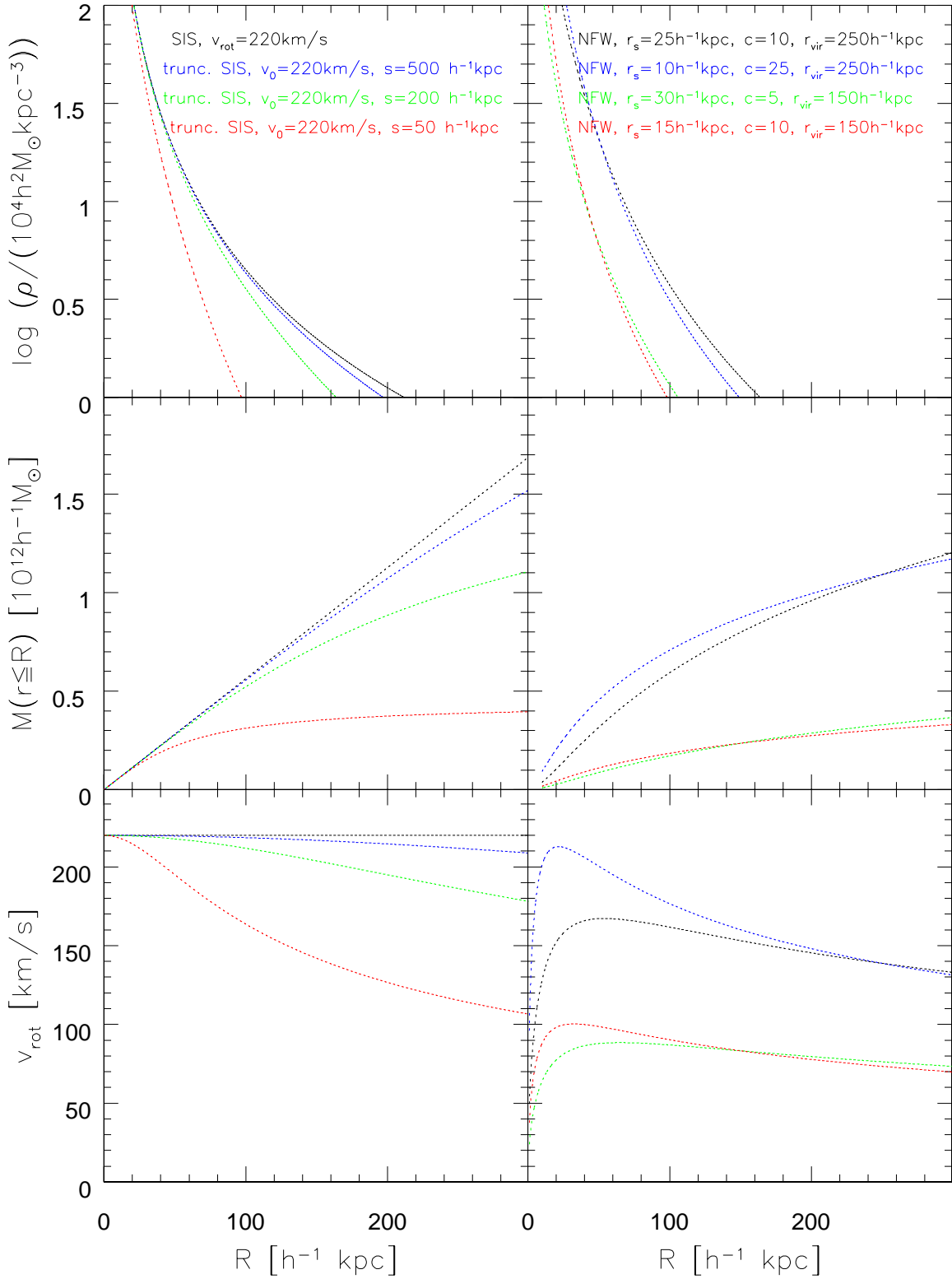


Figure 2.4: Density profiles (upper panels), aperture masses (middle panels) and rotation velocities (lower panels). The left panels are for the SIS and truncated SIS models while the right panels correspond to the NFW profile.

where δ_c is a characteristic density, ρ_m is the mean matter density of the universe and r_s is a scale radius. The NFW profile has the following dependence on radius

$$\rho(r) \propto \begin{cases} r^{-1} & \text{for } r \ll r_s \\ r^{-3} & \text{for } r \gg r_s \end{cases} . \quad (2.17)$$

For each halo, a *virial radius* r_{vir} is defined. This is the radius inside which the mean density equals the *virial overdensity* Δ_{vir} times the mean density of the Universe at that redshift. The virial overdensity is given by the spherical collapse model (Eke et al., 1996), often $\Delta_{\text{vir}} = 200$ is used. The mass inside the virial radius is the *virial mass* M_{vir} . The exact value of Δ_{vir} is dependent on the formation redshift of the halo and on the cosmology. Bryan and Norman (1998) have provided simple formulae for Δ_{vir} which are accurate to 1% for $\Omega_m(z) = 0.1 - 1$, where $\Omega_m(z)$ is the mean matter density of the Universe at a given redshift in units of the critical density $\rho_{\text{crit}} = \frac{3H^2}{8\pi G}$. For flat cosmologies one has

$$\Delta_{\text{vir}} = 18\pi^2 + 82 \times (\Omega_m(z) - 1) - 39 \times (\Omega_m(z) - 1)^2 . \quad (2.18)$$

In an Einstein-de Sitter Universe $\Omega_m \equiv 1.0$ and hence $\Delta_{\text{vir}} = 18\pi^2 \approx 178$ which is close to the commonly used value of $\Delta_{\text{vir}} = 200$. However, for $\Omega_m(z=0) = 0.3$, as found for the current standard cosmological model, Eq. (2.18) yields only $\Delta_{\text{vir}} = 101$ at $z = 0$. But on the other hand, $\Omega_m(z)$ at the formation redshift of a halo has to be used and $\Omega_m(z) \rightarrow 1.0$ for increasing z . Therefore, the use of $\Delta_{\text{vir}} = 200$ is reasonable.

A concentration parameter c of a halo is defined by

$$c = r_{\text{vir}}/r_s . \quad (2.19)$$

Because the mass within a radius R is given by

$$M(r \leq R) = 4\pi\delta_c \rho_m r_s^3 \left[\ln \left(1 + \frac{R}{r_s} \right) - \frac{R/r_s}{1 + R/r_s} \right] , \quad (2.20)$$

and the virial mass can also be expressed as

$$M_{\text{vir}} = \frac{4}{3}\pi\Delta_{\text{vir}}\rho_m r_{\text{vir}}^3 , \quad (2.21)$$

the following relation between the characteristic density δ_c and the concentration c must hold:

$$\delta_c = \frac{\Delta_{\text{vir}}}{3} \frac{c^3}{\ln(1+c) - c/(1+c)} \quad (2.22)$$

From Eq. (2.20) and $v_{\text{rot}}^2(R) = GM(r \leq R)/R$, the rotation velocity can be calculated. With $x = r/r_{\text{vir}}$ it is given by

$$\left(\frac{v_{\text{rot}}(x)}{v_{\text{vir}}} \right)^2 = \frac{1}{x} \frac{\ln(1+cx) - \frac{cx}{1+cx}}{\ln(1+c) - \frac{c}{1+c}} , \quad (2.23)$$

where v_{vir} is the rotation velocity at the virial radius r_{vir} . The rotation velocity peaks at about $2.16 r_s$. Figure 2.4 shows the rotation velocity as function of radius for different choices of the parameters as well as the corresponding density profiles and aperture masses $M(r \leq R)$.

Navarro et al. (1996, 1997) find that dark matter halos ranging from dwarf galaxies to rich galaxy clusters can all be well fitted by Eq. (2.16), but have different values of their parameters. A strong correlation between the mass of a halo and its characteristic density is seen in the simulations – less massive halos have larger characteristic densities. This can be explained by the fact that less massive halos form earlier in the simulations when the mean density of the Universe is larger. Therefore, halos have to be denser in order to be able to collapse. Although Eq. (2.16) has formally two parameters, δ_c and r_s , this correlation implies that dark matter halos can be described by just one parameter. This can be any of the quantities δ_c , c , r_s , r_{vir} , v_{vir} or M_{vir} and it is a matter of convenience which quantity is chosen.

Bullock et al. (2001) use a more recent and larger simulation of dark matter halos than Navarro et al. (1997) to study in more detail the relation between virial mass, concentration and scale radius. Unlike Navarro et al. (1997), they do not have to resimulate halos with larger resolution after their identification but can simulate a large sample of halos of masses $(10^{11} - 10^{14})h^{-1}M_{\odot}$ and their evolution directly. This further allows them to include subhalos which are defined as halos with centers inside the virial radius of another, larger halo and to study the influence of the environment of halos. These simulations reproduce the findings of Navarro et al. (1997) for halos at $z = 0$ but reveal a different redshift dependence.

We will first summarize their findings for $z = 0$. They find a mild variation of the concentration c with mass M_{vir} of the halos, see Fig. 2.5. The relation is well-fitted by

$$c(M_{\text{vir}}, z \equiv 0) = 9 \left(\frac{M_{\text{vir}}}{1.5 \times 10^{13} h^{-1} M_{\odot}} \right)^{-0.13}. \quad (2.24)$$

Including the $1\text{-}\sigma$ limits, all halos in the investigated mass range have concentrations between $c = 5$ and $c = 30$. However, for subhalos a stronger dependence of the concentration on halo mass is found, see left panel of Fig. 2.6. For subhalos, the $c - M_{\text{vir}}$ relation can be fitted by $c(M_{\text{vir}}, z \equiv 0) \propto M_{\text{vir}}^{-0.3}$ and the concentration can become as large as $c = 50$. The concentration of a halo further depends on its environment. Indeed, the dependence on environment is found to be even stronger than that on mass, see right panel of Fig. 2.6. No fit to the relation is given by Bullock et al. (2001) but from the Figure it can be seen that the concentration in dense environments is about twice the concentration in low-density environments.

Figure 2.7 gives the dependence of the concentration c on redshift z . The left panel shows that for each redshift bin the slope of the $c - M_{\text{vir}}$ relation remains unchanged but that halos of same mass have smaller concentrations at larger redshifts. The right panel shows the change of concentration with redshift directly for halos with $M_{\text{vir}} = (0.5 - 1.0) \times 10^{12} h^{-1} M_{\odot}$. It is fitted by $c(z) \propto (1 + z)^{-1}$. So, combining the mass and redshift dependence, the

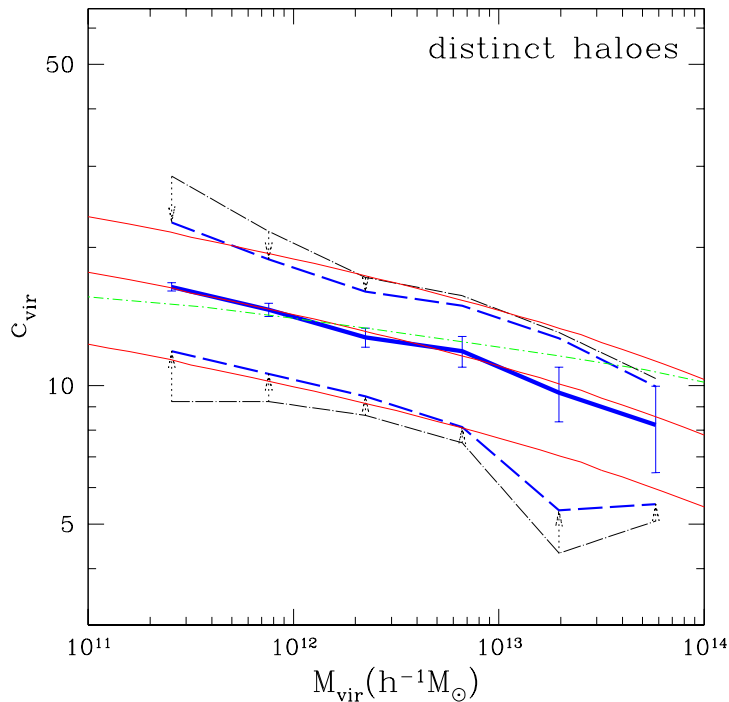


Figure 2.5: Variation of the concentration c with mass M_{vir} of dark matter halos. The thick solid line gives the median concentration for given M_{vir} . The errorbars correspond to Poisson errors due to the finite number of halos per mass bin. The dot-dashed and dashed curves give the $1\text{-}\sigma$ limits measured in two different ways. The thin solid lines represent the fit to the $c - M_{\text{vir}}$ relation and its $1\text{-}\sigma$ limits. Subhalos are excluded in this plot. The Figure is taken from Bullock et al. (2001).

concentration is given by

$$c(M_{\text{vir}}, z) = 9 \left(\frac{M_{\text{vir}}}{1.5 \times 10^{13} h^{-1} M_{\odot}} \right)^{-0.13} (1+z)^{-1}. \quad (2.25)$$

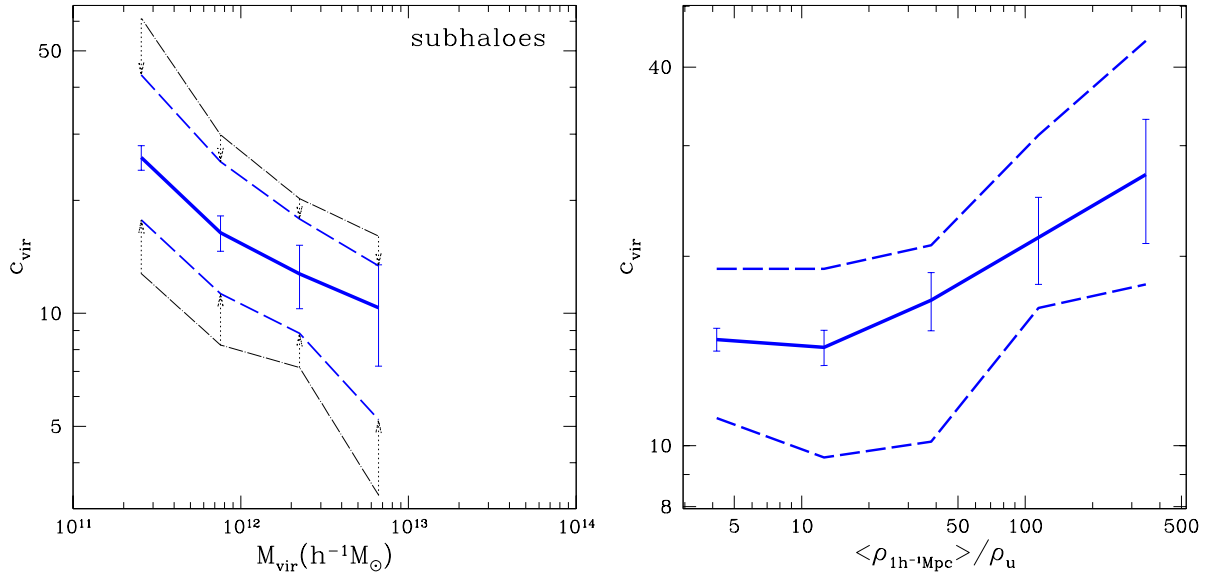


Figure 2.6: Left panel: Same as Fig. 2.5 but now for subhalos. Right panel: Dependence of the concentration c on local density ρ measured within a sphere of radius 1 Mpc. ρ_{u} is the average density of the Universe in the simulations. All halos, including subhalos, with $M_{\text{vir}} = (0.5 - 1.0) \times 10^{12} h^{-1} M_{\odot}$ have been used for the plot. Both Figures are taken from Bullock et al. (2001).

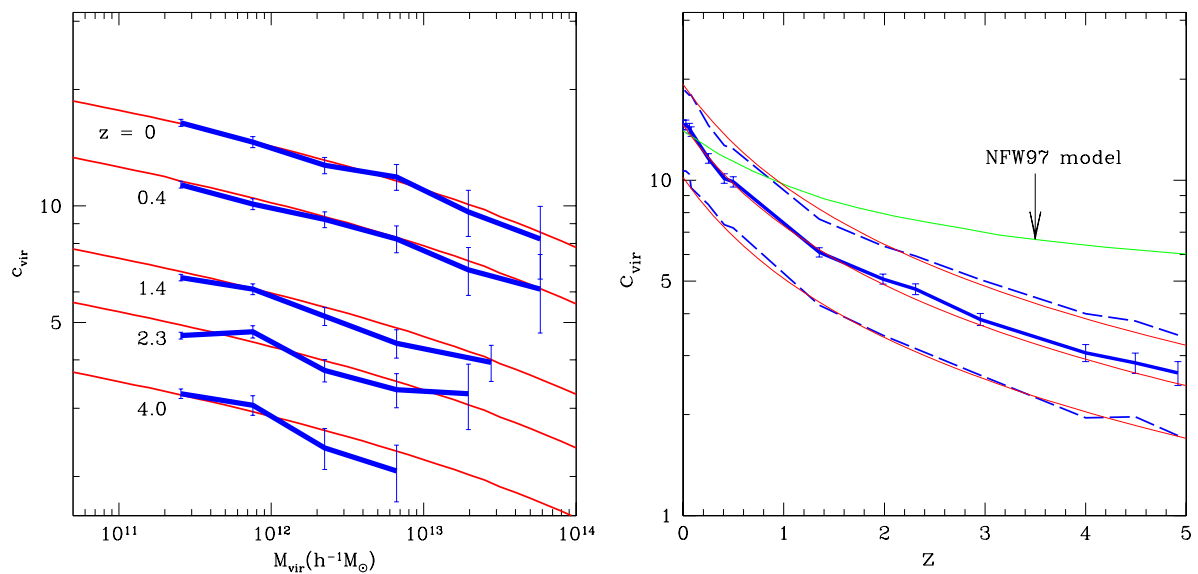


Figure 2.7: Left panel: Median concentration as function of halo mass for different redshift bins. Right panel: Concentration as function of redshift for all halos with $M_{\text{vir}} = (0.5 - 1.0) \times 10^{12} h^{-1} M_{\odot}$. The thick solid line shows the median value and the dashed lines the 1- σ limits. The upper thin line shows the predictions from Navarro et al. (1997). Both Figures are taken from Bullock et al. (2001).

Chapter 3

Gravitational lensing

We use weak gravitational lensing to study the mass profiles of dark matter halos of galaxies. The topic of weak lensing in general and its applications to astrophysical and cosmological problems is described in Bartelmann and Schneider (2001). We will introduce the basic principles of gravitational lensing in Sect. 3.1 and the special regime of weak lensing in Sect. 3.2. The gravitational shear for different lens models is derived in Sect. 3.3. Finally, in Sect. 3.4 we describe galaxy-galaxy lensing which we will use for our measurements.

3.1 General principles

Gravitational lensing is a consequence of General Relativity. Fortunately, in the case of weak fields, the linearized theory can be used. The weak field limit applies when the impact parameter ξ of a light ray is much larger than the Schwarzschild radius $R_S = \frac{2GM}{c^2}$ of the deflector, $\xi \gg R_S$, where G is the gravitational constant, M the mass of the deflector and c the speed of light. Because only light rays can be observed that pass a lens outside its most luminous parts, this condition is fulfilled for deflectors which are normal stars, galaxies or galaxy clusters but not necessarily for compact objects like e.g. neutron stars or black holes. In the weak field limit the deflection angle $\hat{\alpha}$ is given by

$$\hat{\alpha} = \frac{4GM}{c^2\xi} . \quad (3.1)$$

From the condition $\xi \gg R_S$ and $R_S = \frac{2GM}{c^2}$ follows also $\hat{\alpha} \ll 1$.

Figure 3.1 illustrates a gravitational lens system. A source is located at position S and could be seen by the observer at O under an angle β relative to some optical axis if there was no lens. However, in the presence of the lens, the light rays emitted by the source and passing the lens will be deflected. The light ray shown in the Figure that passes the lens at a minimum distance ξ is deflected by the angle $\hat{\alpha}$ such that it hits the observer. The observer then views the source under the angle θ . The *scaled deflection angle* α by which

Equation (3.3) applies for *thin lenses*, that is for lenses which are much less extended along the line-of-sight than the total length of the light path between source and observer. This condition is true for stars, galaxies or galaxy clusters, but not for the large-scale structure. For thin lenses, one can integrate the three-dimensional density profile along the line-of-sight to get the two-dimensional *surface mass density*

$$\Sigma(\vec{\xi}) = \int dr_3 \rho(\vec{\xi}, r_3) . \quad (3.4)$$

The deflection angle then becomes

$$\hat{\alpha} = \frac{4G}{c^2} \int d^2\xi' \Sigma(\vec{\xi}') \frac{\vec{\xi} - \vec{\xi}'}{|\vec{\xi} - \vec{\xi}'|^2} . \quad (3.5)$$

Figure 3.1 shows how for a given lens geometry and deflection angle $\hat{\alpha}$ the image position is related to the source position. If the source is located under an angle $\vec{\beta}$ with respect to some optical axis then an image of that source will be seen under the angle $\vec{\theta}$. These angles are related by

$$\vec{\beta} = \vec{\theta} - \frac{D_{\text{ds}}}{D_{\text{s}}} \hat{\alpha}(\theta) \equiv \vec{\theta} - \vec{\alpha}(\theta) , \quad (3.6)$$

where Eq. (3.2) has been used. Equation (3.6) is only true for small angles. However, this condition is fulfilled in the weak field limit and for suitably chosen optical axes, that is the optical axis should be chosen towards the lens. If appropriate, it will be most convenient to choose it through the center of the lens. More than one solution of Eq. (3.6) can exist which means that multiple images will be seen.

A *critical surface mass density* Σ_{crit} can be defined by

$$\Sigma_{\text{crit}} = \frac{c^2}{4\pi G} \frac{D_{\text{s}}}{D_{\text{d}} D_{\text{ds}}} \quad (3.7)$$

as well as a *dimension-less surface mass density* κ

$$\kappa(\vec{\theta}) = \frac{\Sigma(\vec{\theta})}{\Sigma_{\text{crit}}} ; \quad (3.8)$$

κ is also referred to as *convergence*. κ quantifies the strength of a lens. A rough distinction is to call a lens *strong* if $\kappa > 1$ and *weak* if $\kappa < 1$.

Using Eqs. (3.3), (3.6), (3.7) and (3.8) together with $\vec{\xi} = D_{\text{d}} \vec{\theta}$, the scaled deflection angle $\vec{\alpha}$ can be also expressed as

$$\vec{\alpha}(\theta) = \frac{1}{\pi} \int d^2\theta' \kappa(\vec{\theta}') \frac{\vec{\theta} - \vec{\theta}'}{|\vec{\theta} - \vec{\theta}'|^2} . \quad (3.9)$$

This can be written as

$$\vec{\alpha} = \nabla \Psi , \quad (3.10)$$

where Ψ is the *deflection potential*

$$\Psi(\vec{\theta}) = \frac{1}{\pi} \int d^2\theta' \kappa(\vec{\theta}') \ln |\vec{\theta} - \vec{\theta}'| . \quad (3.11)$$

Ψ is the two-dimensional analogue to the Newtonian gravitational potential. It satisfies the Poisson equation

$$\nabla^2 \Psi(\vec{\theta}) = 2\kappa(\vec{\theta}) . \quad (3.12)$$

The image positions of point sources can be calculated from Eq. (3.9). This can, in principle, also be done for extended sources which will yield, in addition to the image positions, the shapes of the images. Because for each point of an extended source the impact parameter $\vec{\xi}$ and thus the deflection angle $\hat{\alpha}$ is slightly different, the image will have a different shape than the source. This can be described by a lens mapping from the source plane to the lens plane. This mapping can be locally linearized if the deflection angle $\hat{\alpha}$ does not change too much for the points inside a source, that is if the source is small enough. The distortion of the images is described by the Jacobian matrix

$$\mathcal{A}(\vec{\theta}) = \frac{d\vec{\beta}}{d\vec{\theta}} = \left(\delta_{ij} - \frac{d^2\Psi(\vec{\theta})}{d\theta_i d\theta_j} \right) = \begin{pmatrix} 1 - \kappa - \gamma_1 & -\gamma_2 \\ -\gamma_2 & 1 - \kappa + \gamma_1 \end{pmatrix} \quad (3.13)$$

where the Eqs. (3.6), (3.10) and (3.12) have been used and the components of the *shear*

$$\gamma = \gamma_1 + i\gamma_2 = |\gamma| e^{2i\phi} \quad (3.14)$$

have been introduced. From Eq. (3.13) follows

$$\gamma_1 = \frac{1}{2}(\Psi_{,11} - \Psi_{,22}) , \quad \gamma_2 = \Psi_{,12} , \quad (3.15)$$

\mathcal{A} can be decomposed into a diagonal and a trace-less part

$$\mathcal{A}(\vec{\theta}) = (1 - \kappa) \begin{pmatrix} 1 & 0 \\ 0 & 1 \end{pmatrix} - \begin{pmatrix} \gamma_1 & \gamma_2 \\ \gamma_2 & -\gamma_1 \end{pmatrix} = (1 - \kappa) \begin{pmatrix} 1 & 0 \\ 0 & 1 \end{pmatrix} - |\gamma| \begin{pmatrix} \cos 2\phi & \sin 2\phi \\ \sin 2\phi & -\cos 2\phi \end{pmatrix} . \quad (3.16)$$

This shows that the convergence causes an isotropic focussing of the light rays from the source making it larger without changing its shape, see also Fig. 3.2. The shear distorts the image; the image of an intrinsically round source with unit radius becomes an ellipse with major and minor axis $(1 - \kappa \pm \gamma)^{-1}$. The area of the image is $\frac{1}{\det \mathcal{A}}$ times the area of the source. Because in lensing the surface brightness is conserved, the change in area directly corresponds to a change in magnitude; images are magnified by

$$\mu = \frac{1}{\det \mathcal{A}} = \frac{1}{(1 - \kappa)^2 - |\gamma|^2} . \quad (3.17)$$

For axially-symmetric lenses, the strength of the distortion $|\gamma|$ can be calculated directly from the convergence κ using

$$|\gamma|(\theta) = \bar{\kappa}(\theta) - \kappa(\theta) , \quad (3.18)$$

where $\bar{\kappa}(\theta)$ is the mean dimension-less surface mass density inside a circle with radius θ around the center of the lens.

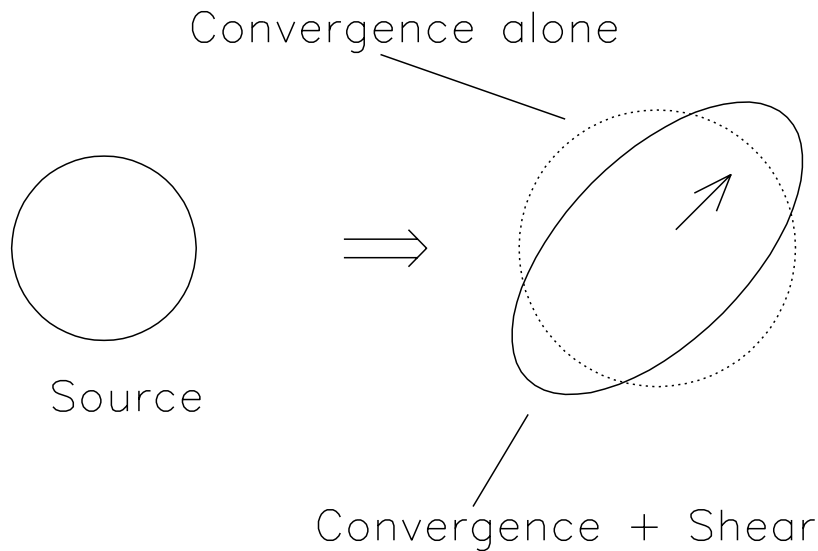


Figure 3.2: Due to lensing the size and shape of an extended source are changed. The convergence makes the source larger while the shear is responsible for distortions. The Figure is taken from Narayan and Bartelmann (1999).

3.2 Weak gravitational lensing

When dealing with extended sources and their distortions, two regimes of lensing can be distinguished, the *strong* and *weak* lensing regime. Of course, there is no sharp transition from strong to weak lensing, and therefore the definitions of the two regimes can vary. A qualitative distinction is that in the strong lensing regime the distortions are large and can already be seen by eye or for individual sources while in the weak lensing regime the distortions are small and can only be detected statistically from several sources. This means that the distortions in weak lensing are much smaller than typical intrinsic ellipticities of galaxies. Strong lensing only appears in massive galaxy clusters or in special lens geometries where lens and source are well aligned such that strong distortions or multiple images occur. However, these situations are rare. Weak lensing, on the other side, occurs basically everywhere. We will use only the effect of weak lensing.

Weak lensing can be measured if somehow the distortion can be quantified. This first requires to have a measure of shapes of galaxies. This issue is not straightforward because images of galaxies can be quite irregular or clumpy, especially those of spiral or irregular galaxies. Photon noise and pixelization add further complications. A commonly used definition of the shape of a galaxy uses the second brightness moments

$$Q_{ij} = \int d^2\theta \theta_i \theta_j I(\theta) , \quad i, j \in \{1, 2\} . \quad (3.19)$$

Here $\vec{\theta}$ denotes the position with respect to the object center and $I(\vec{\theta})$ the surface brightness at position $\vec{\theta}$. A *complex ellipticity* $\chi = \chi_1 + i\chi_2$ can then be defined as

$$\chi_1 = \frac{Q_{11} - Q_{22}}{Q_{11} + Q_{22}} , \quad \chi_2 = \frac{2Q_{12}}{Q_{11} + Q_{22}} . \quad (3.20)$$

For an image with elliptical isophotes and major and minor axes a and b this definition yields the ellipticity $\chi = \frac{a^2 - b^2}{a^2 + b^2}$. Figure 3.3 shows the shapes and orientations of images with different complex ellipticities χ .

Using Eq. (3.13), the second moments $Q_{ij}^{(s)}$ and the complex ellipticity $\chi^{(s)}$ of the source are related to those of the image by

$$Q^{(s)} = \mathcal{A}Q\mathcal{A}^T = \mathcal{A}Q\mathcal{A} \quad (3.21)$$

and

$$\chi^{(s)} = \frac{\chi - 2g + g^2\chi^*}{1 + |g|^2 - 2\text{Re}(g\chi^*)} , \quad (3.22)$$

where χ^* is the complex conjugate of χ and g the *reduced shear*

$$g(\vec{\theta}) = \frac{\gamma(\vec{\theta})}{1 - \kappa(\vec{\theta})} . \quad (3.23)$$

A second definition of the complex ellipticity $\epsilon = \epsilon_1 + i\epsilon_2$ that is more convenient for theoretical considerations is widely used:

$$\epsilon_1 = \frac{Q_{11} - Q_{22}}{Q_{11} + Q_{22} + 2(Q_{11}Q_{22} - Q_{12}^2)^{1/2}} , \quad \epsilon_2 = \frac{2Q_{12}}{Q_{11} + Q_{22} + 2(Q_{11}Q_{22} - Q_{12}^2)^{1/2}} . \quad (3.24)$$

For an image with elliptical isophotes and major and minor axes a , b this definition yields the ellipticity $\epsilon = \frac{a-b}{a+b}$. The ellipticities of the source and its image are related by

$$\epsilon^{(s)} = \begin{cases} \frac{\epsilon - g}{1 - g^*\epsilon} & \text{for } |g| \leq 1 \\ \frac{1 - g\epsilon^*}{\epsilon^* - g^*} & \text{for } |g| > 1 \end{cases} . \quad (3.25)$$

The two complex ellipticities are related by

$$\epsilon = \frac{\chi}{1 + (1 - |\chi|^2)^{1/2}} , \quad \chi = \frac{2\epsilon}{1 + |\epsilon|^2} . \quad (3.26)$$

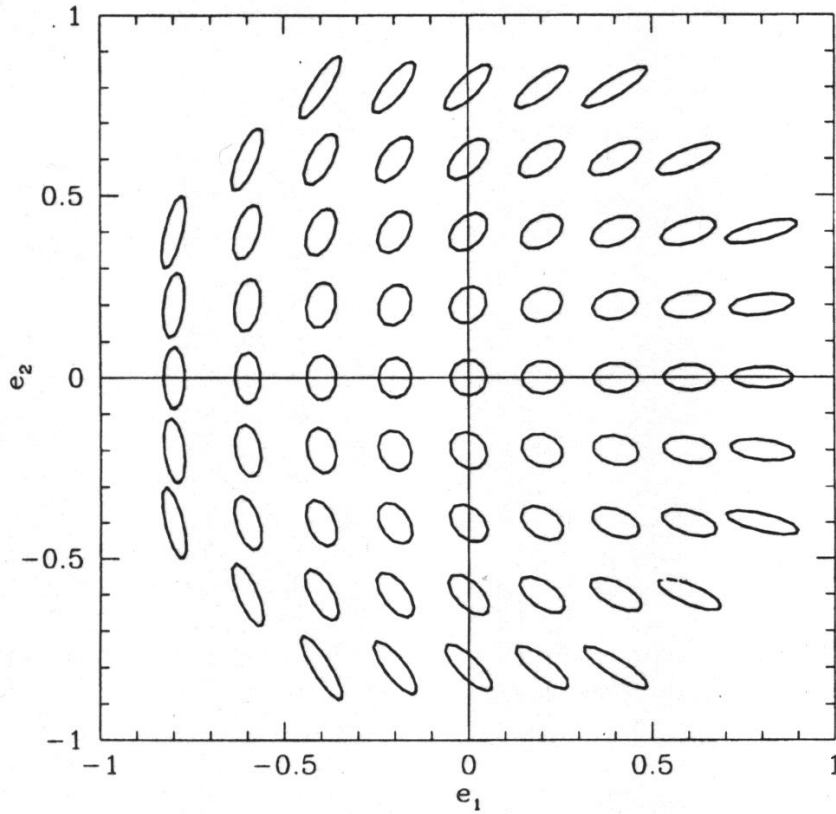


Figure 3.3: Shapes and orientations of ellipses with different complex ellipticities. e_1 and e_2 correspond to our definition of χ_1 and χ_2 , see Eq. (3.20). The Figure is taken from Kaiser et al. (1995).

The actual measurement of the shapes of objects from observational data is a far more complicated task than presented here, mainly because the images of small and faint galaxies are distorted by seeing. Elaborate techniques have been developed to correct for additional distortions which are not due to lensing. In Chapt. 6 we will describe in detail how to do the shape measurement and will test its reliability.

The distortion from lensing and thus the gravitational shear γ can in principle be measured by a comparison of the lensed and unlensed image. One can define the regime of weak lensing where distortions are small by $\kappa \ll 1$ or $\gamma \ll 1$. Then Eq. (3.23) yields $g \approx \gamma \ll 1$ and Eqs. (3.22) and (3.25) reduce to

$$\chi^{(s)} \approx \chi - 2g \approx \chi - 2\gamma \quad (3.27)$$

and

$$\epsilon^{(s)} \approx \epsilon - g \approx \epsilon - \gamma. \quad (3.28)$$

In practice, however, the shear cannot be measured like this because the shape of the unlensed source is not known. But what is generally assumed is that galaxies are randomly oriented and therefore the expectation values of their complex ellipticities is zero,

$$E(\chi^{(s)}) = 0 = E(\epsilon^{(s)}) . \quad (3.29)$$

In particular, it is assumed that – without lensing – the orientations of the sources not correlated with the orientations or positions of the lenses. Lensing introduces such a correlation from which the strength of the shear can be inferred. The most simple case is that several source galaxies are distorted by the same shear. Then one can obtain the shear by simply averaging over the ellipticities of the source galaxies

$$\gamma \approx \langle \epsilon \rangle \approx \frac{\langle \chi \rangle}{2} \quad (3.30)$$

where Eqs. (3.27), (3.28) and (3.29) have been used. From Eqs. (3.29) and (3.30) it becomes clear that, in the weak lensing regime, the shear γ can only be measured from a sufficiently large number of source galaxies.

The assumption of uncorrelated orientations of galaxies has been seriously questioned (e.g. Heavens et al., 2000; Jing, 2002; Heymans and Heavens, 2003). However, it is only argued that physically close galaxies could have correlated orientations. For galaxies at different redshifts, the assumption is not questioned. Because we have accurate photometric redshifts available for our analysis that allow us to use only lens-source pairs with sufficiently large differences in redshift, we are not concerned about intrinsic alignments.

With lensing, the orientations of the images of background galaxies are not random anymore but they are correlated with the positions of the lenses. The most simple and first studied case is that of lensing by galaxy clusters. There the shear is strong enough so that a reasonable number of source galaxies is sufficient for the detection. In that case one can use all sources within a small area on the sky close to the cluster where all galaxies are distorted by approximately the same shear and measure their mean ellipticity to get an estimate of the shear γ . In Sect. 3.4 we will describe how the shear is measured for galaxy-galaxy lensing.

In principle, one could also use the magnification of the sources [see Eq. (3.17)] to measure the lensing effect. The magnification will change the source counts behind lenses and the luminosity function. However, this effect is difficult to measure because one needs to know the expected source counts and shape of the luminosity function without lensing which are hard to determine, especially in view of field-to-field variations. Therefore, the effect of magnification is mostly used for strong lenses, mainly galaxy clusters. We will only use the distortion of the images of background galaxies.

3.3 Lens models

In this subsection we derive the strength of the shear for the different density profiles that have been introduced in Sect. 2.5. Because all models are circularly symmetric, we use Eq.

(3.18) to calculate the shear. The resulting shear profiles for the different lens models are shown in Fig. 3.4.

3.3.1 Singular isothermal sphere

From the density distribution $\rho(r) = \frac{\sigma_v^2}{2\pi G} \frac{1}{r^2}$ [see Eq. (2.8) with $\sigma_v = v_{\text{rot}}/\sqrt{2}$] and Eq. (3.4), the surface mass density can be derived

$$\Sigma_{\text{SIS}}(r) = \frac{\sigma_v^2}{2\pi G} \frac{1}{r}. \quad (3.31)$$

Then, κ is given by [see Eq. (3.8)]

$$\kappa_{\text{SIS}}(r) = \frac{2\pi\sigma_v^2 D_{\text{ds}}D_{\text{d}}}{c^2} \frac{1}{D_{\text{s}} r} \quad (3.32)$$

and

$$\bar{\kappa}_{\text{SIS}}(r) = \frac{4\pi\sigma_v^2 D_{\text{ds}}D_{\text{d}}}{c^2} \frac{1}{D_{\text{s}} r} = 2\kappa_{\text{SIS}}. \quad (3.33)$$

From Eq. (3.18) with $\theta = r/D_{\text{d}}$ then follows the shear

$$\gamma_{\text{SIS}}(r) = \bar{\kappa}_{\text{SIS}}(r) - \kappa_{\text{SIS}}(r) = \kappa_{\text{SIS}}(r) = \frac{2\pi\sigma_v^2 D_{\text{ds}}D_{\text{d}}}{c^2} \frac{1}{D_{\text{s}} r} = \frac{\sigma_v^2}{2G\Sigma_{\text{crit}}} \frac{1}{r}. \quad (3.34)$$

In weak lensing measurements the shear cannot be measured from a single lens galaxy, only the averaged shear from many galaxies can be obtained. The velocity dispersion from fitting the measured shear will thus only be an average over the lens galaxies used. Because it is known that galaxies have different velocity dispersions at least in their inner regions and that these scale with the luminosity following the Tully-Fisher and Faber-Jackson relations, these scaling relations are often used in the galaxy-galaxy lensing analysis. One models the velocity dispersions of the lens galaxies by

$$\frac{\sigma_v}{\sigma_{\star}} = \left(\frac{L}{L_{\star}}\right)^{\eta} \quad (3.35)$$

where L_{\star} is a characteristic luminosity and σ_{\star} the velocity dispersion of these galaxies. η is related to α in Eqs. (2.1) and (2.3) by $\eta = 1/\alpha$. Using the relation (3.35), the velocity dispersion σ_{\star} of L_{\star} galaxies becomes the fitting parameter. From the Tully-Fisher and Faber-Jackson relations one expects $\eta \approx 0.25$, but η can also be taken as additional parameter. Given sufficiently large data sets it is also possible to parametrize the dependence of the velocity dispersion on other quantities like redshift or type of the galaxy.

The (aperture) mass-to-light ratio of the lenses is determined by η . From Eqs. (2.10) and (3.35) it follows

$$\frac{M(r \leq R)}{L} = \frac{2\sigma_{\star}^2 (L/L_{\star})^{2\eta} R}{GL} \propto L^{2\eta-1}. \quad (3.36)$$

So for $\eta = 0.25$ one has $M/L \propto L^{-0.5}$ inside a fixed aperture while $M/L \propto L^0 = \text{const}$ requires $\eta = 0.5$.

3.3.2 Truncated singular isothermal sphere

The density distribution is given by $\rho(r) = \frac{\sigma_v^2}{2\pi G r^2} \frac{s^2}{(r^2 + s^2)}$ [Eq. (2.11) and $\sigma_v = v_0/\sqrt{2}$]. Similar to the SIS, the surface mass density Σ , the dimensionless mass density κ and the strength of the shear γ can be calculated.

$$\Sigma_{\text{trSIS}}(r) = \frac{\sigma_v^2}{2\pi G} \frac{1}{r} \left(1 - \frac{r}{\sqrt{r^2 + s^2}} \right), \quad (3.37)$$

$$\kappa_{\text{trSIS}}(r) = \frac{2\pi\sigma_v^2}{c^2} \frac{D_{\text{ds}}D_{\text{d}}}{D_{\text{s}}} \frac{1}{r} \left(1 - \frac{r}{\sqrt{r^2 + s^2}} \right), \quad (3.38)$$

$$\bar{\kappa}_{\text{SIS}}(r) = \frac{4\pi\sigma_v^2}{c^2} \frac{D_{\text{ds}}D_{\text{d}}}{D_{\text{s}}} \frac{1}{r} \left(\frac{r+s}{r} - \frac{\sqrt{r^2 + s^2}}{r} \right), \quad (3.39)$$

$$\gamma_{\text{trSIS}}(r) = \frac{2\pi\sigma_v^2}{c^2} \frac{D_{\text{ds}}D_{\text{d}}}{D_{\text{s}}} \frac{1}{r} \left(\frac{r+s}{r} - \frac{\sqrt{r^2 + s^2}}{r} \right) = \frac{\sigma_v^2}{2G\Sigma_{\text{crit}}} \frac{1}{r} \left(\frac{r+s}{r} - \frac{\sqrt{r^2 + s^2}}{r} \right). \quad (3.40)$$

Just as for the SIS, the scaling relation (3.35) is often used for the truncated isothermal sphere. Additionally, one can also use a scaling relation between the outer scale s and the luminosity L of an lens

$$\frac{s}{s_{\star}} = \left(\frac{L}{L_{\star}} \right)^{\eta_s}. \quad (3.41)$$

The mass-to-light ratio is dependent on η_s and η . It is given by [see Eqs. (2.13) and (3.41)]

$$\frac{M}{L} = \frac{\pi\sigma_{\star}^2(L/L_{\star})^{2\eta} s_{\star}(L/L_{\star})^{\eta_s}}{2GL} \propto L^{2\eta+\eta_s-1}. \quad (3.42)$$

Therefore, for $\eta = 0.25$ one can still obtain constant mass-to-light ratios by setting $\eta_s = 0.5$.

3.3.3 Navarro-Frenk-White halo

The shear for lenses that can be described by NFW profiles has been derived by Wright and Brainerd (2000) and Bartelmann (1996). The surface mass density for the NFW profile

$\rho(r) = \frac{\delta_c \rho_m}{r/r_s(1+r/r_s)}$ [Eq. (2.16)] is

$$\Sigma_{\text{NFW}}(x) = \begin{cases} \frac{2r_s\delta_c\rho_m}{x^2-1} \left[1 - \frac{2}{\sqrt{1-x^2}} \operatorname{arctanh} \sqrt{\frac{1-x}{1+x}} \right] & \text{for } x < 1 \\ \frac{2r_s\delta_c\rho_m}{3} & \text{for } x = 1 \\ \frac{2r_s\delta_c\rho_m}{x^2-1} \left[1 - \frac{2}{\sqrt{x^2-1}} \operatorname{arctan} \sqrt{\frac{x-1}{1+x}} \right] & \text{for } x > 1 \end{cases}, \quad (3.43)$$

where the dimensionless radius $x = r/r_s$ has been introduced. The mean surface mass density inside the dimensionless radius x is then given by

$$\bar{\Sigma}_{\text{NFW}}(x) = \begin{cases} \frac{4r_s\delta_c\rho_m}{x^2} \left[\frac{2}{\sqrt{1-x^2}} \operatorname{arctanh}\sqrt{\frac{1-x}{1+x}} + \ln\left(\frac{x}{2}\right) \right] & \text{for } x < 1 \\ 4r_s\delta_c\rho_m \left[1 + \ln\left(\frac{1}{2}\right) \right] & \text{for } x = 1 \\ \frac{4r_s\delta_c\rho_m}{x^2} \left[\frac{2}{\sqrt{x^2-1}} \operatorname{arctan}\sqrt{\frac{x-1}{1+x}} + \ln\left(\frac{x}{2}\right) \right] & \text{for } x > 1 \end{cases} \quad (3.44)$$

The strength of the shear can be calculated from

$$\gamma_{\text{NFW}}(x) = \frac{\bar{\Sigma}_{\text{NFW}}(x) - \Sigma_{\text{NFW}}(x)}{\Sigma_{\text{crit}}} \quad (3.45)$$

which is equivalent to Eq. (3.18). One obtains

$$\gamma_{\text{NFW}}(x) = \begin{cases} \frac{r_s\delta_c\rho_m}{\Sigma_{\text{crit}}} g_{<}(x) & \text{for } x < 1 \\ \frac{r_s\delta_c\rho_m}{\Sigma_{\text{crit}}} \left[\frac{10}{3} + 4 \ln\left(\frac{1}{2}\right) \right] & \text{for } x = 1 \\ \frac{r_s\delta_c\rho_m}{\Sigma_{\text{crit}}} g_{>}(x) & \text{for } x > 1 \end{cases} \quad (3.46)$$

where $g_{<}(x)$ and $g_{>}(x)$ are given by

$$g_{<}(x) = \frac{8\operatorname{arctanh}\sqrt{(1-x)/(1+x)}}{x^2\sqrt{1-x^2}} + \frac{4}{x^2} \ln\left(\frac{x}{2}\right) - \frac{2}{x^2-1} + \frac{4\operatorname{arctanh}\sqrt{(1-x)/(1+x)}}{(x^2-1)(1-x^2)^{1/2}} \quad (3.47)$$

and

$$g_{>}(x) = \frac{8\operatorname{arctan}\sqrt{(x-1)/(1+x)}}{x^2\sqrt{1-x^2}} + \frac{4}{x^2} \ln\left(\frac{x}{2}\right) - \frac{2}{x^2-1} + \frac{4\operatorname{arctan}\sqrt{(x-1)/(1+x)}}{(x^2-1)^{3/2}} \quad (3.48)$$

3.4 Galaxy-galaxy lensing

3.4.1 Theory

The aim of galaxy-galaxy lensing is to study the dark matter halos of the lens galaxies. One is interested in the density profiles of these halos, their extent and mass, and how these quantities depend on properties of the galaxies like type, luminosity, environment or redshift. Gravitational lensing induces correlations between the ellipticities and orientations of background galaxies and the positions of lens galaxies. In the absence of lensing, the images of the background galaxies are randomly oriented and not affected by the foreground

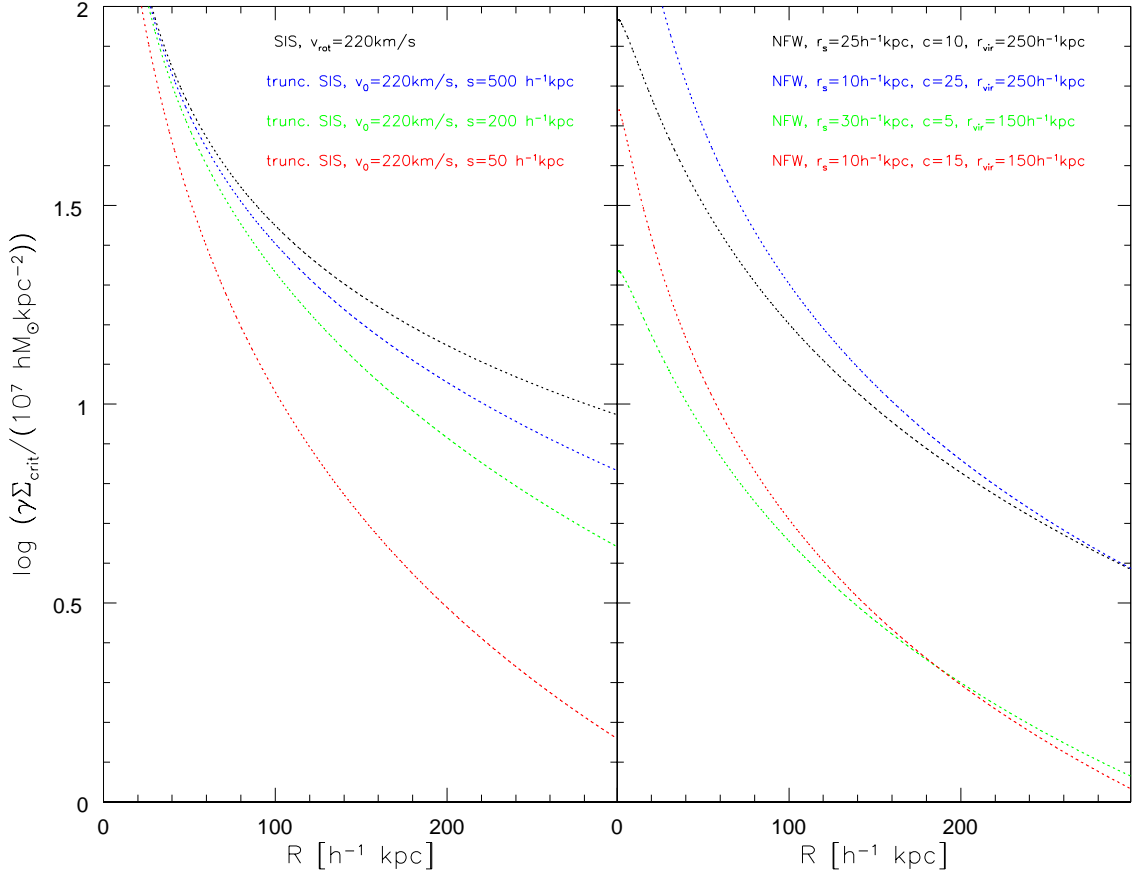


Figure 3.4: Shear profiles for the SIS and truncated SIS models (left panel) and the NFW profile (right panel).

galaxies. Therefore, no correlation should be measured. With lensing, however, images of background galaxies will be slightly stretched tangentially with respect to the lenses. So the images of background galaxies will be, on average, tangentially aligned with respect to the lens galaxies. Figure 3.5 illustrates this effect for intrinsically round background galaxies, where we refer to the projected shapes of unlensed galaxies.

Unfortunately, galaxies are not intrinsically round. Typical intrinsic ellipticities are much larger than ellipticities induced by weak lensing. For example, for a SIS lens, the shear is given by Eq. (3.34)

$$|\gamma| = 0.035 \left(\frac{\sigma_v}{155 \text{ km s}^{-1}} \right)^2 \left(\frac{\theta}{10''} \right)^{-1} \frac{D_{\text{ds}}}{D_s}, \quad (3.49)$$

while the width of the intrinsic ellipticity distribution in our sample is around 0.35. So for a typical lens with $\sigma_v = 155 \text{ km s}^{-1}$ and in only $10''$ distance from its center, corresponding e.g. to $38 h^{-1} \text{ kpc}$ at $z = 0.4$ (for $\Omega_m = 0.3$ and $\Omega_{\Lambda} = 0.7$), the shear and thus the change in

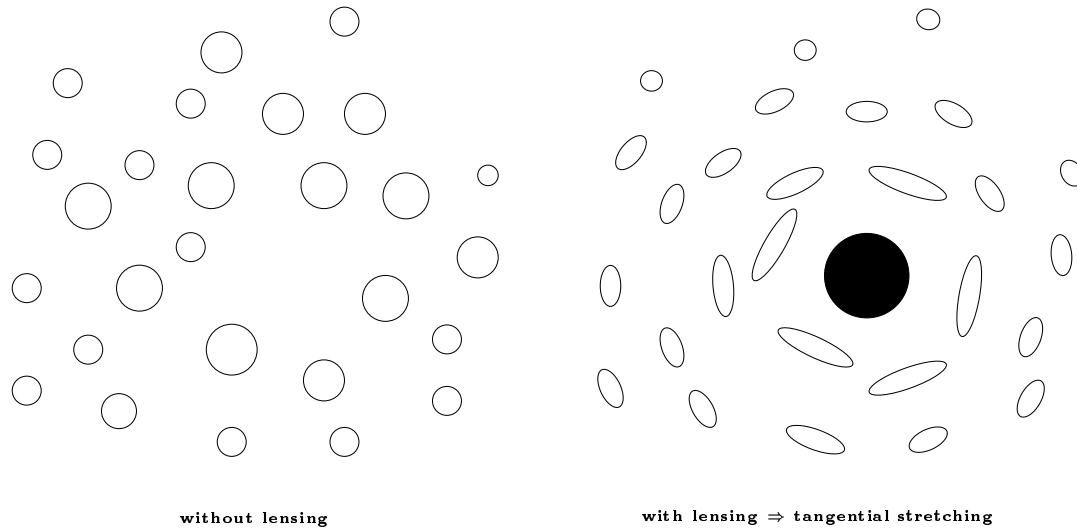


Figure 3.5: Lens effect on intrinsically round background galaxies

ellipticity is one order of magnitude smaller than typical ellipticities. Because the intrinsic ellipticity for an individual background galaxy is not known, the effect of lensing cannot be measured for a single lens-source pair. Any detection or non-detection of an alignment of the source with respect to the lens can be due to the random orientation of the source galaxy. Only when averaging over thousands of background galaxies can the alignment be measured. This, however, has the consequence that one also has to average over at least hundreds of lens galaxies. Therefore, galaxy-galaxy lensing can measure dark matter halos of galaxies only statistically.

Due to the statistical nature of the measurement, only averaged halo profiles can be measured. But galaxies are intrinsically different in their optical properties. Therefore, it should be investigated if the dark matter halos are also different and how these depend on e.g. luminosity or spectral type of the galaxies. A first step is to split the lens galaxy sample into different subgroups according to the parameter one wants to study. With a sufficiently large data set one can then use a parametrized lens model that contains the extra parameter. This explains why very large data sets are needed for galaxy-galaxy lensing.

However, not only the area, geometry and depth of a data set determines its suitability for galaxy-galaxy lensing. Most important, the shapes of the images of source galaxies have to be measured accurately. This requires best seeing conditions, proper coaddition of individual frames, correction for distortions in the atmosphere or telescope and a weighting scheme that allows one to quantify the reliability of shape measurements of individual galaxies. Further, redshift information is needed when combining the shear measurements from different lens-source pairs. This is because the strength of the lens effect is dependent not only on the masses of the lenses but also on the distances between lens, source and

observer. In the absence of accurate spectroscopic redshifts, redshift probability functions can be applied that are derived from only a magnitude or multi-colour photometry. The more accurate the redshifts can be estimated, the smaller will be the noise due to uncertainties in the distances or due to false lens-source pairs where the source is actually in front of the assumed lens. Finally, detailed knowledge of redshifts, spectral types or clustering of galaxies is needed if the dependence on luminosity, type, environment or redshift is studied. Our measurement of galaxy shapes will be described in Sect. 6.2 while in Chapt. 5 we will explain how we obtain redshifts and spectral classification for the galaxies.

3.4.2 Methods to measure galaxy-galaxy lensing

Galaxy-galaxy lensing makes the images of background galaxies aligned with respect to the lenses. Therefore, the most direct way to measure galaxy-galaxy lensing is to investigate for all lens-source pairs the *tangential ellipticity* ϵ_t of the source with respect to the lens and to average in radial bins over ϵ_t . Given a lens at position (x_d, y_d) and a source at position (x_s, y_s) , ϵ_t is defined as

$$\epsilon_t = -[\epsilon_1 \cos(2\alpha) + \epsilon_2 \sin(2\alpha)] , \quad (3.50)$$

where $\alpha = \arctan[(y_s - y_d)/(x_s - x_d)]$.

Because ϵ_t is directly related to the shear $\gamma = \langle \epsilon_t \rangle$, ϵ_t can be used to infer the average density profile of the lens galaxies. Unfortunately, the interpretation of such an averaged profile will not be straightforward because the halo profile could be very different for galaxies of different types. Further, typically a source galaxy is lensed by more than a single lens galaxy. Especially when two or more lens galaxies are physical neighbours or lie along the same line-of-sight, their individual shear contributions will stretch the source image in similar directions making it hard to disentangle the different contributions.

A much better way is to use the maximum-likelihood method developed by Schneider and Rix (1997). The basic idea is to identify for each source galaxy all lens galaxies and to calculate the combined shear from all lenses together using a parametrized lens model. Then, the likelihood that the calculated shear leads to the observed shapes of the source images is calculated. Finally, the parameters of the lens model are varied to find those which give the maximum likelihood.

In more detail the method works as follows: First, potential source galaxies are identified. These are all galaxies within a certain magnitude range $R_{s,\min} < R_s \leq R_{s,\max}$ and a certain redshift range $z_{s,\min} < z_s \leq z_{s,\max}$ and that have a half-light radius greater than the size of the PSF. We will later consider all lens-source pairs where the source lies within a projected physical separation smaller than $r_{p,\max}$ from the center of the lens. The corresponding angular separation $\theta_{p,\max}$ is dependent on the distance $D_d(z)$ of the lens. It is greatest for the smallest lens redshift $z_{d,\min}$. Therefore only source galaxies that have a distance $\theta > \frac{r_{p,\max}}{D_{d,\min}}$ from the edge of the field can be considered, because otherwise potential lenses would lie outside the field. In small fields or fields with unfavorable geometry this can be a serious limitation. In such cases one can use simulations of the galaxy distribution outside

the field and thus statistically take the shear from these galaxies into account. This allows one to use all source galaxies within the field. For more details we refer to Hudson et al. (1998) who used this approach for a galaxy-galaxy lensing analysis of the Hubble Deep Field North. We will not use such simulations here because we want to use our large fields to study the dark matter halos of galaxies with as little extra assumptions as possible. We note that we can still somewhat increase our number of sources by decreasing $r_{p,\max}$ or increasing $z_{d,\min}$.

The minimum angular separation $\theta_{\text{neighbour}}$ between a source and a projected neighbour must be large enough such that the shape measurement of the source galaxy is not affected by the light of the neighbouring galaxy. We choose $\theta_{\text{neighbour}} = 10 \text{ pixel} = 2.38''$, see also Sect. 7.1.

For each pair of a lens galaxy i and a source galaxy j the shear γ_{ij} can be calculated according to one of the models described in Sect. 2.5 and Sect. 3.3. The total shear γ_j that acts on the source galaxy j is to first order $\gamma_j = \sum_i \gamma_{ij}$. An estimator for the intrinsic ellipticity $\epsilon_j^{(s)}$ is therefore

$$\epsilon_j^{(s)} = \epsilon_j - \gamma_j . \quad (3.51)$$

Assuming that the intrinsic ellipticity distribution of the source galaxies can be described by a Gaussian with width σ_{ϵ_1} and σ_{ϵ_2} for each ellipticity component, the probability for this intrinsic ellipticity is

$$P(\epsilon_j^{(s)}) = \frac{1}{2\pi\sigma_{\epsilon_1}\sigma_{\epsilon_2}} \exp \left[- \left(\frac{(\epsilon_{1,j}^{(s)})^2}{2\sigma_{\epsilon_1}^2} + \frac{(\epsilon_{2,j}^{(s)})^2}{2\sigma_{\epsilon_2}^2} \right) \right] . \quad (3.52)$$

If $\sigma_{\epsilon_1} = \sigma_{\epsilon_2}$ with $\sigma_{\epsilon}^2 = \sigma_{\epsilon_1}^2 + \sigma_{\epsilon_2}^2$, this simplifies to

$$P(\epsilon_j^{(s)}) = \frac{1}{\pi\sigma_{\epsilon}^2} \exp \left[- \frac{|\epsilon_j^{(s)}|^2}{\sigma_{\epsilon}^2} \right] . \quad (3.53)$$

Note that $P(\epsilon_j^{(s)})$ is not normalized because $\epsilon_j^{(s)}$ is restricted to $|\epsilon_j^{(s)}| < 1$. However, this is of no concern because the normalization does not enter into the following considerations.

The likelihood function \mathcal{L} is the product of the probabilities for all source galaxies. The log-likelihood function ℓ then becomes

$$\ell = \ln \mathcal{L} = \sum_j \left(- \frac{|\epsilon_j^{(s)}|^2}{\sigma_{\epsilon}^2} - \ln(\pi\sigma_{\epsilon}^2) \right) . \quad (3.54)$$

The best-fit parameters for a given lens model are determined by maximizing the log-likelihood ℓ . Error estimates on the best-fit parameters can also be obtained directly from the log-likelihood function because, in the limit of a large number of events, it is related to the χ^2 statistics by

$$\chi^2 = -2 \ln \ell + \text{const} . \quad (3.55)$$

So for e.g. two parameters one can obtain the 1- σ limits from $\ell_{\max} - \ell = 1.15$, the 2- σ limits from $\ell_{\max} - \ell = 3.085$ and the 3- σ limits from $\ell_{\max} - \ell = 5.90$ (Bevington and Robinson, 1992; Press et al., 1992).

Chapter 4

Observations of dark matter halos of galaxies

Only two methods are currently used to investigate dark matter halos of galaxies on large scales of a few hundred kpc. Apart from gravitational lensing, the study of the dynamics of satellite galaxies is the only promising technique. In this Chapter the results from satellite dynamics and from galaxy-galaxy lensing made by other groups will be presented. At the end of the Chapter we will examine how the data set from COMBO-17 will compare to the previous studies.

4.1 Satellite dynamics

The study of satellite dynamics uses satellite galaxies as tracers of the potential of brighter and thus probably more massive central galaxies. The satellites can then be regarded as test particles that do not disturb the potential of the primary. This method extends the measurements of rotation curves from e.g. HI clouds to larger radii. However, although these two techniques are similar in principle, the study of satellite dynamics encounters additional problems which are not, or to a lesser degree, present in the study of rotation curves from HI data. Like any dynamical measurement, the use of satellites as tracers yields only reliable results if the assumed satellites are actually bound to the primary galaxy. However, at larger distances from the centers of the galaxies, this assumption becomes less justified. Galaxies, which are only chance projections but not physically associated with the central galaxy, can heavily bias the results. They are called *interlopers*. The analysis of the dynamics of satellites gets complicated because typically only the velocity difference between primary and satellite is known while the orbital parameters like inclination or eccentricity are unknown. A further limitation of the method is that, like in lensing studies, dark matter halos of galaxies can only be studied statistically because central galaxies typically have only 1-2 satellites in the required magnitude range, that is bright enough for detection and spectroscopy but faint enough such that the satellites are most probably much less massive than the primaries. Therefore, several central galaxies have to be stacked

and thus only averaged density profiles can be obtained.

Results on spiral galaxies

Zaritsky et al. (1993, 1997) concentrated on spiral galaxies as central galaxies. They further restrict their sample of primary galaxies to the Hubble types Sb and Sc and to galaxies with absolute magnitudes $-22.4 < M_B < -18.8$ with slightly different selection criteria in the two publications. The motivation for this strong selection is the fact that central rotation velocities are type- and luminosity-dependent. Because primary galaxies have to be stacked, a homogeneous sample of primary galaxies makes the interpretation of the results less complicated. Isolation of the primary galaxies is further required, meaning that primaries are excluded from the analysis if they have neighbours within 500 kpc that are not at least 2.2 mag fainter or a neighbour within 1 Mpc that is not at least 0.7 mag fainter than the primary. Satellite galaxies are defined as galaxies within a projected distance of 500 kpc that are at least 2.2 mag fainter than the primary and that have a velocity difference of $\Delta v < 500 \text{ km s}^{-1}$ relative to the primary. The minimum magnitude difference assures that satellites are much less massive than the primary and can thus be regarded as test particles. The maximum velocity difference excludes galaxies that are only in projection close to the primary but that are physically unbound. Zaritsky et al. (1993) end up with a total of 69 satellites around 45 primaries. Taking three radial bins they find that the velocity difference of the satellites relative to the primaries stays constant out to about 500 kpc ($H_0 = 75 \text{ km s}^{-1} \text{ Mpc}^{-1}$) which implies that the primaries have constant rotation velocities out to these large radii. They are constant even if the most probable interlopers are excluded. For a typical halo, a rotation velocity of about 200 km s^{-1} is derived which is in good agreement with the value in the inner parts. Most surprisingly, there is no correlation between the rotation velocity and the luminosity of the primary galaxies. This is different from the behaviour in the inner parts where rotation velocity and luminosity are connected by the Tully-Fisher relation (see Sect. 2.2). Therefore, the large-scale properties of galaxies seem to be independent of the properties on smaller scales. Zaritsky et al. (1997) reproduce these findings with a larger data set of 115 satellites around 69 primaries.

Early- and late-type galaxies from the SDSS

McKay et al. (2002) use data from the not yet completed Sloan Digital Sky Survey (SDSS) for studies of satellite dynamics. Their primary galaxies are brighter than $r' = 16.3$ corresponding to redshifts $z < 0.05$ for most of the galaxies. They further require that primary galaxies are at least two times more luminous than any neighbouring galaxy within a projected distance of $2h^{-1} \text{ Mpc}$ that have a velocity difference below $\pm 1000 \text{ km s}^{-1}$. McKay et al. (2002) estimate from the $u' - r'$ colour that about 75% of the primary galaxies are early-type galaxies and only 25% are late-type galaxies. Therefore, their sample of primary galaxies differs significantly from that used by Zaritsky et al. (1993, 1997). Satellite galaxies are all galaxies within projected distances below $500h^{-1} \text{ kpc}$ from

a primary and that are at least 1.5 mag fainter than the primary and have a velocity difference below $\pm 1000 \text{ km s}^{-1}$ relative to it. On average, every primary galaxy has about two satellites. Primary galaxies having many satellites with combined luminosities above that of the primary are excluded because these are rather central galaxies of groups. In total, the sample contains 618 primary galaxies and 1225 satellites.

McKay et al. (2002) also do not find evidence for a declining rotation velocity. However, their main objective is to confirm mass-to-light scaling laws for luminosities measured in different wavebands that were reported from a galaxy-galaxy lensing analysis of the same data set (McKay et al., 2001), see also Sect. 4.2. This somehow limits their analysis because they do not fit mass-to-light scaling relations $M \propto L^\beta$ to the satellite data but merely point out the consistency with the previous lensing analysis which gave $M \propto L$ or $\beta = 1$ for all but the u' -band. This differs from the results of Zaritsky et al. (1993, 1997) who find no correlation of the rotation velocity and thus the aperture mass with luminosity of the primaries. However, unlike Zaritsky et al. (1993, 1997), McKay et al. (2002) do not investigate a homogeneous sample of primary galaxies but a mix of early- and late-type galaxies. At low luminosity the late-type galaxies are dominating while at high luminosity the early-type galaxies are more abundant. It does not become clear how much the changing morphological mix affects their results. Further, because no errors on β are quoted in the different satellite dynamics studies, it is not clear if the different results are inconsistent with each other at all or if it is maybe just due to the better statistics in the SDSS data set that McKay et al. (2002) find a correlation of rotation velocity with luminosity of the primary.

Improved removal of interlopers

Prada et al. (2003) also use the SDSS but supplement it with data from the RC3 catalog (de Vaucouleurs et al., 1991) which allows them to check for close neighbours outside the area covered by the SDSS which consists of thin stripes. Further, for large and bright galaxies, magnitudes are taken from the RC3 catalog which turned out to be more accurate than the photometry provided within the SDSS for these galaxies. Prada et al. (2003) restrict primary galaxies to those having absolute magnitudes $M_B \leq -19$ and apply additionally three different selection criteria, one of which mimicks those applied by McKay et al. (2002). The first two only differ in the allowed redshift range for primaries, $z \leq 0.03$ and $z \leq 0.2$. Apart from this, the primaries must have no neighbour within $500h^{-1}\text{kpc}$ with a velocity difference below 1000 km s^{-1} and which are not at least 2 magnitudes fainter. The satellites for these two samples are defined as galaxies within $350h^{-1}\text{kpc}$ which are at least 2 magnitudes fainter than the primary and have a velocity difference relative to it below 500 km s^{-1} . The third sample takes all galaxies with $z \leq 0.2$ which have no neighbour within $2h^{-1}\text{Mpc}$, a magnitude difference below 0.75 mag, and a velocity difference below 1000 km s^{-1} as primaries. Prada et al. (2003) argue that this third sample should contain more primary galaxies which lie actually in groups instead of being isolated compared to the first two samples. The requirements for satellite galaxies for the third sample are that they are 1.5 mag fainter than the primary, lie within a projected distance of $500h^{-1}\text{kpc}$ and

have a velocity difference below 1000 km s^{-1} . For the different samples they find between 453 and 2734 satellites around 283 to 1107 primaries.

Prada et al. (2003) pay special attention to the removal of interlopers. They test their description for the removal on simulated data and compare the results from the real data with and without removal. For all three samples, they find a declining velocity dispersion when they remove the interlopers which is consistent with the NFW profile. Interestingly, without removal of interlopers or when applying the fitting description of McKay et al. (2002) they find flat or even rising velocity dispersions. From the tests of the different techniques of removal of interlopers on simulated data Prada et al. (2003) argue that their result of a declining velocity dispersion is more reliable than the previous findings of McKay et al. (2002) of a flat rotation curve.

Finally, Prada et al. (2003) test the dependence of halo mass or velocity dispersion on luminosity of the primary. They use four luminosity bins and calculate the velocity dispersion inside $120h^{-1}\text{kpc}$. The results are consistent with a dependence of the form $\sigma \propto L^{0.3}$ agreeing very well with the Tully-Fisher and Faber-Jackson relations on smaller scales (see Sect. 2.2) but being at variance with the findings of McKay et al. (2001, 2002) who find constant mass-to-light ratios ($\sigma \propto L^{0.5}$). Using the velocity dispersion at a larger radius of $350h^{-1}\text{kpc}$ instead, Prada et al. (2003) are able to reproduce the finding of McKay et al. (2001, 2002). This can explain the differences to the McKay et al. (2001, 2002) results who used a radius of $260h^{-1}\text{kpc}$ in both of their analyses.

4.2 Galaxy-galaxy lensing

Since the initial detection by Brainerd et al. (1996), galaxy-galaxy lensing has been measured from various data sets. These data sets are very different, ranging from the very deep but small Hubble Deep Field North to shallow but large ground-based data sets like the SDSS. The population of lens galaxies that can be probed is correspondingly very different. Further, some measurements were obtained with photometric or even spectroscopic redshifts whereas some focused only on a special type of lens galaxies. The applied analysis techniques are also different. All of this makes it very difficult to compare the different results reported and to draw a comprehensive picture of dark matter halos of galaxies from them. Clearly, these measurements can only be regarded as the beginning of a series of galaxy-galaxy lensing studies. In the following, the main results obtained so far will be summarized.

The first detection

The first detection of galaxy-galaxy lensing was made by Brainerd et al. (1996). They used about 90 square arcminutes of deep R-band data taken with the 5 m Hale telescope, Palomar. The total exposure time is 24 ks, yielding a $1\text{-}\sigma$ surface brightness limit of $\mu_r = 28.8 \text{ mag arcsec}^{-2}$ at a seeing of $0.87''$ FWHM. For the selection of lens and source galaxies, a simple magnitude cut of $R = 20 - 23$ for the lenses and $R = 23 - 24$ for the

sources is used. Brainerd et al. (1996) also use fainter source galaxies but find that their inclusion does not improve the result, probably because their shape measurements are too noisy. The estimated redshift range covered by the lens galaxies is $z = 0.2 - 0.8$. Brainerd et al. (1996) then correlate the orientations of the source galaxies with the positions of lens galaxies lying within projected separations of $\theta = 5'' - 34''$. They find that the source galaxies are preferentially tangentially aligned with respect to the lenses, as predicted for galaxy-galaxy lensing. After several successful tests like correlating the orientations of the source galaxies with random points or with the positions of stars, or splitting the field into two subsamples in several ways, they conclude that the observed alignment is indeed due to lensing.

To quantify their findings Brainerd et al. (1996) model the halos of the lens galaxies by the truncated isothermal sphere (see Sects. 2.5.2 and 3.3.2) and use the Tully-Fisher/Faber-Jackson relations as well as a scaling relation between the outer scale s and the luminosity of the lenses, see Eq. (3.41). Additionally, they adopt a redshift probability distribution that relates the magnitudes of galaxies to their redshifts. This probability distribution was obtained from redshift surveys but it has to be extrapolated by about one magnitude for the faintest source galaxies. From Monte Carlo simulations of artificial data sets, Brainerd et al. (1996) determine the best fitting model parameters (rotation velocity $v_{\text{rot},\star}$ and outer scale s_\star for L_\star galaxies) with their uncertainties. In these simulations they use different values of the model parameters to calculate the expected signal which they then compare to the measured one. The rotation velocity $v_{\text{rot},\star}$ can be well constrained to $v_{\text{rot},\star} = (220 \pm 80) \text{ km s}^{-1}$ (90% confidence). On the characteristic scale only a lower limit of $s_\star > 25h^{-1} \text{ kpc}$ ($1-\sigma$) can be obtained.

Data sets from the Hubble Space Telescope

Three publications use data from the Hubble Space Telescope (HST) for galaxy-galaxy lensing studies, two of these use the Hubble Deep Field North (HDFN) (Griffiths et al., 1996; dell'Antonio and Tyson, 1996; Hudson et al., 1998). Advantages of HST data are the good image quality and, in case of the HDFN, the depth while the small field of view is a clear disadvantage and makes it hard to get a sufficiently large galaxy sample. The most concise results are obtained by Hudson et al. (1998) who made use of spectroscopic and photometric redshifts and used the method by Schneider and Rix (1997) (see Sect. 3.4.2) for their analysis. The redshift distribution of their lens galaxies extends to $z = 0.85$. Hudson et al. (1998) parametrize the lens galaxies by the truncated isothermal sphere model with a Tully-Fisher/Faber-Jackson relation. Further, they allow for evolution of the rotational velocity of L_\star galaxies with redshift. Although they try to constrain four parameters (rotation velocity of L_\star galaxies, outer scale s_\star of the halos, Tully-Fisher/Faber-Jackson index η , and ζ which describes the evolution) they only arrive at meaningful constraints for the rotation velocity for which they obtain $v_{\text{rot},\star} = (210 \pm 40) \text{ km s}^{-1}$. For η they obtain a lower limit of about $\eta > 0.35$ ($1-\sigma$).

Probing the evolution of halos of early-type galaxies

To probe the evolution of halos of galaxies with redshift it is necessary to have a deep data set such that lens galaxies at different redshifts can be identified. Further, redshift estimates have to be available and the data set has to be large enough so that the lens galaxy sample can be split into different subsamples. Redshift estimates from measurements in only two filters can be obtained for early-type galaxies because these are the reddest and brightest galaxies at all redshifts. Wilson et al. (2001) use 1.5 square degrees of deep data in V and I taken at the Canada France Hawaii Telescope (CFHT) to select early-type galaxies at redshifts $z = 0.1 - 0.9$ with luminosities around L_* as lens galaxies. The source galaxy sample consists roughly of galaxies with $I = 21 - 25$ for which they model a redshift probability distribution using deep redshift surveys which still have to be extrapolated to $I = 25$. All lens-source pairs with projected separations $\theta = 20'' - 60''$ are used to measure the tangential shear in radial bins. This separation corresponds to physical radii $r = (26 - 77)h^{-1}$ kpc at $z = 0.1$ and $r = (105 - 315)h^{-1}$ kpc at $z = 0.9$, correspondingly. Wilson et al. (2001) find no clear evidence for evolution in the velocity dispersion and thus in the mass of dark matter halos. The corresponding rotation velocity they find is $v_{\text{rot},*} = 238_{-30}^{+27}$ km s $^{-1}$ for early-type lens galaxies with $z = 0.25 - 0.75$.

An upper limit on the extent of halos of galaxies

Hoekstra et al. (2002) reported for the first time an upper limit on the outer scale s_* in the truncated isothermal sphere model. They used data from the Canadian Network for Observational Cosmology Field Galaxy Redshift Survey (CNOC2) covering about 530 arcmin 2 down to about $R = 24.4$ (90% completeness limit). For 1125 out of a total of about 11000 lens galaxies, spectroscopic redshifts are available; the median redshift of these galaxies is $z = 0.36$. Using only lens galaxies with spectroscopic redshifts and adopting a Tully-Fisher/Faber-Jackson relation ($\sigma \propto L_B^{0.25}$) and a constant outer scale $s = s_*$, they find $\sigma_* = 125_{-16}^{+14}$ km s $^{-1}$ and $s_* = 432_{-106}^{+181}h^{-1}$ kpc where the uncertainties are 1- σ limits. Using a scaling relation $s \propto \sigma^2$ they find $s_* = 350_{-90}^{+152}h^{-1}$ kpc. Brainerd et al. (1996) and Hudson et al. (1998) could – due to the small sizes of their fields – only give confidence regions for $s_* < 200h^{-1}$ kpc and $s_* < 100h^{-1}$ kpc, respectively. This can explain that an upper limit on s_* is not seen in their results. On the other hand, Fischer et al. (2000) use early commissioning imaging data from the SDSS to investigate $s_* < 900h^{-1}$ kpc without detecting an upper limit on s_* . They have no redshifts available and probe lens galaxies which are apparently brighter and thus probably at smaller redshift than in the Hoekstra et al. (2002) data set. McKay et al. (2001) use a larger area from the SDSS as Fischer et al. (2000), having also spectroscopic redshifts for the lens galaxies. Using a deconvolution technique to separate the halo profile of individual galaxies from the contribution of neighbours they also find no upper limit on the outer scale s . However, they do not use any scaling of the velocity dispersion σ_v or the outer scale s with lens luminosity L , which makes a direct comparison even harder. Clearly, the question of the extent of dark matter halos of galaxies is not settled yet.

First investigation of the dependences of halos of galaxies on galaxy type, luminosity and environment

McKay et al. (2001) use about 400 square degrees of imaging data from the SDSS and select only those galaxies as lens galaxies that have spectroscopic redshifts available. This allows them to derive luminosities of the lenses as well as to characterize their environment. The peak of the lens redshift distribution is around $z = 0.2$. From morphological information, colour and concentration of the light distribution they further classify the lens sample into early and late types. First, they fit a power-law model to the shear as function of radius without adopting a Tully-Fisher/Faber-Jackson relation. They find a shear profile that is declining as $r^{-0.8 \pm 0.2}$ ($1-\sigma$) which is even shallower than for the SIS model. However, the fit extends from 20 kpc to 980 kpc so that the contribution of neighbouring galaxies will dominate the fit at large radii. The normalization of the power-law fit would – if the slope was exactly -1 as for the SIS model – correspond to a velocity dispersion of 139 km s^{-1} .

When splitting the lens sample into four bins in luminosity, McKay et al. (2001) find a strong dependence of the strength of the shear on luminosity such that more luminous galaxies produce larger shear and are thus more massive. This relation holds when using the luminosities measured in g' , r' , i' and z' but not in u' where they find that the shear is independent of lens luminosity. Their explanation for this observation is that the u' -luminosity is determined mainly by the most recent star formation which is not related to the overall properties of the lenses, while the flux in the redder bands is related to the integrated star formation history which is much more dependent on the total mass of the lenses. McKay et al. (2001) also determine aperture mass-to-light ratios inside $260h^{-1}$ kpc using now the SIS model. This yields a constant mass-to-light ratio, $M \propto L$, for all bands except u' . This contradicts the Tully-Fisher/Faber-Jackson relation which – at scales of a few tenth of kpc – gives $M \propto L^{0.5}$.

Further findings are that early-type galaxies produce a shear that has a 3 times larger normalization in the power-law fit than late-type galaxies. This result is obtained by splitting the lens galaxies into two subsamples. McKay et al. (2001) claim that the radial profile is the same for early- and late-type galaxies. However, when looking at their data points, the visual impression is more that the shear from early-type galaxies extends out to larger radii. For this subsample the shear is still detectable at the largest radii that have been probed ($\approx 1h^{-1}$ Mpc) while for late-type galaxies the shear is detectable out to only about $400h^{-1}$ kpc.

In a next step, McKay et al. (2001) investigate two subsamples according to the environment of the lens galaxies. There they find that lens galaxies in overdense environments produce larger shear that also extends out to larger radii while galaxies in underdense environments are associated with smaller shear that extends out to about the same distance as for the late-type galaxy sample. McKay et al. (2001) further note that, on average, the galaxies in under- or overdense environment have very similar luminosities and morphological types.

Improved analysis of the dependence of halos of galaxies on galaxy type, luminosity and environment

The SDSS data set was also analyzed by Guzik and Seljak (2002) who apply the NFW profile to the data set and include the contribution from groups and clusters in their modeling. Especially in dense environments, this contribution is not negligible. An analysis of only those lens galaxies that lie in underdense regions allows one to estimate the lensing signal that is (almost) purely due to the lens galaxies.

Guzik and Seljak (2002) distinguish three components which contribute to the shear: the lens galaxies themselves, the surrounding galaxies, and the group or cluster halos in which the lenses reside. They show that the second contribution is negligible on scales below $1h^{-1}$ Mpc. To model the third contribution, Guzik and Seljak (2002) have to make several assumptions like the halo mass function for the group and cluster halos which describes the number density of halos as a function of their masses, and a halo occupation function that gives the average number of galaxies residing in a halo of given mass. Further, they assume a relation between luminosity and mass of halos of the form $M/M_{\star} = (L/L_{\star})^{\beta}$.

Before applying their model to the SDSS data set, Guzik and Seljak (2002) test the dependences on the different parameters. The lensing signal is mostly affected by the virial masses of the lens galaxies. Only a small dependence on the concentration index c in the NFW profile is found. For $c = 3 - 16$ they find differences only at radii below about $150h^{-1}$ kpc. However, at a scale of $50h^{-1}$ kpc, the difference in the density contrast is about 100% between $c = 3$ and $c = 16$ but then decreases rapidly towards larger radii. They also compare the difference in the shape of the lensing signal from a lens population of the same halo mass and a population with a distribution in halo masses. Remarkably, they find hardly any difference in the resulting density contrast if the mean halo mass is the same in both populations and if all galaxies are at the centers of the halos. We will refer to these galaxies as *central galaxies*. Therefore, the averaged density profile can reliably be measured for a population of central galaxies with different masses. Because field galaxies are mainly central galaxies, these allow one to derive the density profiles and virial masses of galaxies. The contribution from the groups or clusters in which the lens galaxies are residing is negligible at small radii. It peaks around $250h^{-1}$ kpc depending on the exact modeling of the halo occupation. Beyond that radius, the contribution declines again. At $1h^{-1}$ Mpc, the absolute group/cluster contribution to the density contrast is the same as at scales of $(50 - 100)h^{-1}$ kpc. If all lens galaxies reside in groups or clusters, then the group/cluster contribution at its peak radius is about 3-4 times larger than that of a central galaxy of mass $10^{12}M_{\odot}$.

When applying their model to the SDSS data, Guzik and Seljak (2002) investigate three items: the dependence on luminosity measured in the same filters as used by McKay et al. (2001), the fraction α of galaxies residing in larger group or cluster halos, and the dependence on morphology. To investigate the luminosity dependence they split the sample into four luminosity bins for which they fit M_{\star} and β . They use two different assumptions for the group/cluster contribution, first assuming that the contribution is negligible for all but the lowest luminosity bin and second assuming that it is the same for all bins. The

main result here is that their model does not reproduce the finding of McKay et al. (2001) of a constant mass-to-light ratio. Guzik and Seljak (2002) find instead that the mass-to-light ratio increases with luminosity with $\beta \approx 1.5$ for all but the u' -filter. However, McKay et al. (2001) fit aperture mass-to-light ratios while Guzik and Seljak (2002) fit virial mass-to-light ratios. The virial mass of an L_* -galaxy is around $9 \times 10^{11} h^{-1} M_\odot$ for each of the measured filters. Next, they fix the value of β and fit M_* and α . The best fit gives a group/cluster contribution of about 20%. The χ^2 in this fit is substantially reduced compared to the fit before where M_* and β were varied. Splitting the lens sample according to the environment into a low- and high-density one, $\alpha = 0.45$ for the high-density environment and $\alpha = -0.07$ for the low-density one, which is consistent with $\alpha = 0$, is found. This result gives confidence that the model works well. Guzik and Seljak (2002) further find very similar M_* for the low- and high-density samples. From this they conclude that there seems to be no evidence for halo stripping in dense environments or for different star formation efficiencies.

Finally, Guzik and Seljak (2002) investigate the dependence on morphology. They find that for the late-type sample the group/cluster contribution is significantly smaller than for the early-type sample. This is independent evidence for the morphology-density relation according to which early-type galaxies are more abundant in dense environments while late-type galaxies are preferentially found in the field. Further, early-type L_* galaxies have larger virial masses than late-type L_* galaxies. The discrepancy can be as large as a factor of 10 in u' and drops to about 2 in i' and z' . The mass-to-light ratios are significantly larger for early-type galaxies. Therefore, the fitted values of β could be just due to the changing mix of galaxy types at the bright and faint ends of the luminosity distribution. Guzik and Seljak (2002) estimate that in the red bands $\beta = 1.4 \pm 0.2$ for early-type galaxies. An independent estimate of β for the late-type sample is not possible with the current data set.

The density profiles of halos of galaxies

Wilson et al. (2001) compared the velocity dispersions for L_* early-type galaxies found from galaxy-galaxy lensing to those found from the Faber-Jackson relation. This gives two estimates for the corresponding rotation velocity, 360 km s^{-1} on scales of a few tenth of kpc and 240 km s^{-1} on larger scales of $(50 - 200)h^{-1} \text{ kpc}$. Thus, the rotation velocity is not constant and therefore the density declines more steeply than $\rho \propto r^{-2}$.

Seljak (2002) also compares estimates of the velocity dispersion on small scales from the Tully-Fisher and Fundamental Plane relations to those obtained from galaxy-galaxy lensing from the SDSS data set. This comparison is done for early- and late-type galaxies with luminosities around L_* separately. For early-type galaxies, Seljak (2002) finds that the rotation velocity is decreasing from the optical radius to the virial radius by a factor of 1.68 while for late-type galaxies the decrease is a factor of 1.8. To reconcile these findings with the theoretically expected NFW profile either requires larger concentrations than expected from simulations or a significant contribution from baryonic matter in the central parts of the galaxies. Using reasonable values for the stellar mass-to-light ratios in early-

and late-type galaxies, Seljak (2002) finds that concentrations of $8 < c < 15$ for late-type galaxies and $c \approx 10$ for early-type galaxies provide reasonable fits of the NFW profile to the data.

4.3 Summary on galaxy properties at large radii

Although the various studies presented in Sects. 4.1 and 4.2 are all quite different in the techniques and data sets used, some firm conclusions can already be drawn from them.

- Galaxies are surrounded by large dark matter halos that extend to radii much larger than the optical parts of the galaxies.
- The density profile of the galaxies seems to decline more steeply than isothermal. No study investigated if the truncated isothermal sphere or the NFW profile provides a better fit. However, due to the success of the NFW profile in numerical simulations, this profile seems to become now the preferred one in modeling observations of dark matter halos of galaxies.
- At radii above about $(200-250)h^{-1}$ kpc, the contribution from a possible group/cluster environment becomes important.
- A relation between the velocity dispersion of galaxies measured at large radii and their luminosity exists such that more luminous galaxies have larger velocity dispersions. However, the exact relation between luminosity and velocity dispersion remains somewhat undetermined and seems to depend on the radial range over which the velocity dispersion is measured.
- The density profiles of early- and late-type galaxies are different. Early-type galaxies are more massive than late-types and might extend out to larger radii.

4.4 COMBO-17 compared to previous studies

After having presented in some detail previous studies on dark matter halos of galaxies, the question is what COMBO-17 will be able to contribute to the topic. In Sect. 4.4.1 we will briefly compare the potential of galaxy-galaxy lensing to that of the study of satellite dynamics. Then, in Sect. 4.4.2, we will discuss how COMBO-17 compares to other data sets used for galaxy-galaxy lensing so far.

4.4.1 Lensing measurements in comparison to satellite dynamics

The data requirements for galaxy-galaxy lensing are quite different from those for satellite studies. Lensing requires high-quality imaging data from which shapes of background galaxies can be measured, while satellite studies need mostly spectroscopic data from

which velocities and velocity differences can be obtained. The COMBO-17 data set that will be described in Chapt. 5 is clearly not suited for satellite studies while it is very well suited for lensing studies. But apart from the suitability of a given data set we think that there are good reasons to use galaxy-galaxy lensing which seems to have a larger potential than satellite studies. The main limitation of using satellite dynamics is that it is a dynamical study which has to rely on dynamical assumptions. However, at large distances from the centers of the primaries or at larger redshifts when satellite systems might still be in the formation process, these assumptions become quite uncertain. Further, satellite studies are so far restricted to isolated galaxies so that the connection between galaxies and surrounding groups cannot be studied. It is not clear whether it will be possible in the future to include brighter galaxies as satellites which cannot be regarded any more as test particles that do not perturb the potentials of the primaries. One can well imagine that detailed comparisons to simulations will allow one to study not only isolated galaxies. However, with galaxy-galaxy lensing, these cases are already studied now. Simulations show that with lensing, dark matter halos of galaxies and the group-cluster connection can be studied reliably. It seems that the proper modeling is already available and that all that is needed now are enough data to which it can be applied. However, it has to be stressed that it is desirable to have both kinds of studies because these provide independent probes and can thus confirm the results of the other method.

4.4.2 COMBO-17 in comparison to other lensing data sets

Since its first detection, galaxy-galaxy lensing has been applied to increasingly detailed modeling of dark matter halos of galaxies. After it has become clear that galaxies are surrounded by large dark matter halos, one now wants to investigate the density profiles and the dependence of dark matter halos on e.g. luminosity, morphology or environment of galaxies. These issues require detailed knowledge on the lens galaxies. For low-redshift galaxies this knowledge can be obtained from spectroscopy as in the SDSS. The huge data set of the SDSS will, once the survey is finished, probably answer most questions for the low-redshift galaxies. However, at larger redshifts, spectroscopic redshifts are currently not available for a sufficiently large data set so that one has to use photometric redshifts instead. The unique multi-colour classification from 17 optical filters in COMBO-17 allows us to derive detailed classification for galaxies at higher redshifts such that lens galaxies at redshifts up to about $z = 0.7$ can be studied. This redshift range with redshift information available has so far only been probed by the studies from the small HDFN (Hudson et al., 1998) and by Wilson et al. (2001) who had to restrict their analysis to early-type galaxies. The data set from COMBO-17 is much larger than the sample from the HDFN and not restricted to a special type of lens galaxies. It further provides us with redshifts for the source galaxies so that no redshift probability distributions and especially no extrapolations of these have to be used. This makes COMBO-17 an unprecedented data set for studying dark matter halos of galaxies at redshifts around $z \approx 0.5$.

Chapter 5

The COMBO-17 survey

In this Chapter we present the COMBO-17 survey from which we take the data for our galaxy-galaxy lensing studies. COMBO-17 is a deep extragalactic survey which is specialized on obtaining accurate photometric redshifts and spectral classification for objects as faint as $R = 24$. Deep R -band observations at the best seeing conditions make it also a unique data set for lensing studies. Its web page¹ gives a detailed overview of the various scientific applications which include mainly studies of the galaxy and quasar population. In Sects. 5.1 and 5.2 we present the observations and the data reduction. Then, in Sect. 5.3, we introduce the unique multi-colour approach used in COMBO-17 for deriving spectral classification and redshift estimates. Section 5.4 gives a brief overview over the fields for which data reduction has already been finished. However, the galaxy population in particular will only be investigated in more detail in Chapt. 7. The reason is that for our galaxy-galaxy lensing studies we will use an object list that is merged from those provided by COMBO-17 and additional ones which are based on sumframes that are better suited for shape measurements (see Chap. 6). Finally, Sect. 5.5 contains a summary of the parts of the work on the COMBO-17 data that have been carried out within this thesis.

5.1 Observations

The observations and the data reduction are already described in Wolf et al. (2001a, 2003a). All observations were obtained with the Wide Field Imager (WFI) (Baade et al., 1998a,b) at the MPG/ESO 2.2-m telescope on La Silla, Chile. The WFI is a mosaic camera that consists of eight $2k \times 4k$ CCDs amounting to about 67 million pixels in total. The pixel scale is $0.238''$ resulting in a field-of-view of $33' \times 34'$. Because of the gaps between the CCDs, a dither pattern with ten telescope pointings spread by $\Delta\alpha, \Delta\delta < \pm 72''$ has been applied such that all positions within the field are covered by at least eight exposures.

All observations were taken between January 1999 and May 2002 in eight different observing runs of 1 to 15 nights duration each. In total, 48.5 nights were spent on the survey with an outcome of about 80% usable time. The observations were taken on 4 different,

¹<http://www.mpia-hd.mpg.de/COMBO/>

non-contiguous fields in 17 optical filters yielding a total area of about 1 square degree. Additionally, in this time a fifth field has been observed only in *BVRI* together with the COMBO-17 fields. This field is usually not quoted as one of the survey fields but it has so far been used in the data reduction for creating superflats, see Section 5.2.1, and in a weak lensing analysis of the shear power spectrum (Brown et al., 2003). This field contains the FORS Deep Field (e.g. Heidt et al., 2003). The positions of the four survey fields are given in Table 5.1. The A901 field contains a supercluster consisting of the Abell clusters Abell 901a, Abell 901b and Abell 902. It has specifically been chosen for a weak lensing analysis of this supercluster (Gray et al., 2002). The CDFS field has been chosen because it contains the Chandra Deep Field South that is studied in X-rays and several other wavebands in addition to the optical. This will provide a unique data set for detailed studies of X-ray sources and their optical properties. The SGP field is centered on the South Galactic Pole which is also a prominent field. Finally, the S11 field is a random field which by chance overlaps with the 2dF Redshift Survey.

The filterset with exposure times and magnitude limits is given in Table 5.2. Figure 5.1 gives an overview over the filterset. The very deep R-band exposures were preferentially taken at the best seeing conditions (below $0.8''$ PSF). They are used for the object detection and for measuring shapes needed for lensing studies. The choice of this particular filterset with a unusually large number of medium-band filters will be explained in Sect. 5.3 where the method of deriving photometric redshifts and spectral classification from this data set will be outlined.

Besides the scientific exposures, calibration data were taken. These include twilight flat-fields that were taken with exposure times between 0.5 and 100 seconds per frame. At least three exposures with offsets of $10''$ were taken per observing run and filter from which then the final flatfields are created.

For each field and in each filter, at least three short exposures with exposure times of about 1 tenth or 1 twentieth of the ‘normal’ scientific exposures were taken. These allow one to establish a set of tertiary standard stars. Note that the primary standard star is Vega while those stars that have been calibrated using Vega directly are denoted as secondary standard stars (Wolf, 1999). The tertiary standard stars in the COMBO-17 fields are calibrated using secondary standard stars which do not necessarily lie within the COMBO-17 fields. The short exposures were calibrated using these stars, which are of spectral types G-F with magnitudes $B_J \approx 16$ and which would be close to the saturation limit and thus unusable on some of the long exposures, depending on the filter. Stars below the saturation limit and with good signal-to-noise on both the short and long exposures are then used to calibrate the long exposures. The accuracy of this calibration was estimated from comparing several spectra of the external calibrator HD 49798 and was found to be better than 10%.

Table 5.1: Positions of the four survey fields observed by COMBO-17 with the complete filterset. The last column gives the galactic reddening from Schlegel et al. (1998).

Field	α_{J2000}	δ_{J2000}	l_{gal}	b_{gal}	E_{B-V}
A901	09 ^h 56 ^m 17 ^s	-10°01'25"	248.0°	+33.6°	0.06
S11	11 ^h 42 ^m 58 ^s	-01°42'50"	270.5°	+56.8°	0.02
CDFS	03 ^h 32 ^m 25 ^s	-27°48'50"	223.6°	-54.5°	0.01
SGP	00 ^h 45 ^m 56 ^s	-29°35'15"	328.8°	-87.3°	0.02

5.2 Data reduction

A pipeline for the data reduction has been developed at the MPIA. This pipeline is based on the MIDAS package and makes use of routines that were already developed for the Calar Alto Deep Imaging Survey (CADIS). The pipeline consists of two parts of which the first includes all steps until the coaddition of final sumframes for each observing run and filter. The second part then starts with the creation of an object list from the deepest R-band sumframes. Next, flux measurements for all filters are performed. These are used to calculate colour indices for all objects which are the input for the classification and redshift estimation.

5.2.1 Data reduction pipeline, part I: Image Processing

Part I of the data reduction pipeline starts with the raw data and results in cosmic-corrected images and sumframes.

Input of files

The files of the scientific images and the flatfields are read in from a tape or disk and converted into the MIDAS image format. For each image, nine files are created, one header file and eight files corresponding to the eight individual CCDs.

Bias subtraction

All raw images contain a bias such that even at zero second exposure time the count rate is not zero. Thus, in all exposures, the number of counts is too high by this bias. This way it is guaranteed that the number of counts is always positive. Without bias it could otherwise become negative for exposures with very small counts (due to e.g. short exposure times or narrow filters) because of photon and read-out noise. The bias level is obtained from about forty columns on the right-hand side of each CCD which do not get exposed but which contain the bias. A one-dimensional image is calculated for each CCD from the average over these columns and then smoothed. This image is subtracted from every column of the exposed part of the CCD. Further, the counts are converted into electrons

Table 5.2: The COMBO-17 filterset. The listed exposure times and 10- σ detection limits for point sources are averages over the three fields (A901, S11, CDFS) for which the data reduction has already been finished.

$\lambda_{\text{cen}}/\text{fwhm}$ (nm)	Name	$t_{\text{exp}}/\text{sec}$	$m_{\text{lim},10\sigma}$
364/38	<i>U</i>	20000	23.7
456/99	<i>B</i>	14000	25.5
540/89	<i>V</i>	6000	24.4
652/162	<i>R</i>	20000	25.2
850/150	<i>I</i>	7500	23.0
420/30		8000	24.0
462/14		10000	24.0
485/31		5000	23.8
518/16		6000	23.6
571/25		4000	23.4
604/21		5000	23.4
646/27		4500	22.7
696/20		6000	22.8
753/18		8000	22.5
815/20		20000	22.8
856/14		15000	21.8
914/27		15000	22.0

that correspond to the actual number of photons that have hit the CCD. On average, only about every second photon is detected. For some of the CCDs, nonlinearities exist such that the number of counts does not depend linearly on the exposure level for high levels. The gain and the nonlinearities for each CCD are reported in the WFI User Manual².

Creation of a mosaic image

The eight subimages from the different CCDs are put together into a single image with gaps between the subimages corresponding to the sizes of the gaps between the CCDs. Some of the CCDs are not well aligned with respect to the others. Therefore, pixel shifts are applied to these subimages to mimick rotations. This is done by extracting stripes from the subimage and inserting these in a new image with the appropriate shifts. However, the rotations are small, about 1° or less for all CCDs. A mask is applied to the mosaic image that sets all pixel without information to a negative value of -100 . This allows one to distinguish later between pixel without information and those where no counts are measured but where this zero level actually contains information. Pixel without information are those in the gaps, but also bad columns or bad pixel from the CCDs.

²available from <http://www.ls.eso.org/lasilla/sciops/wfi/>

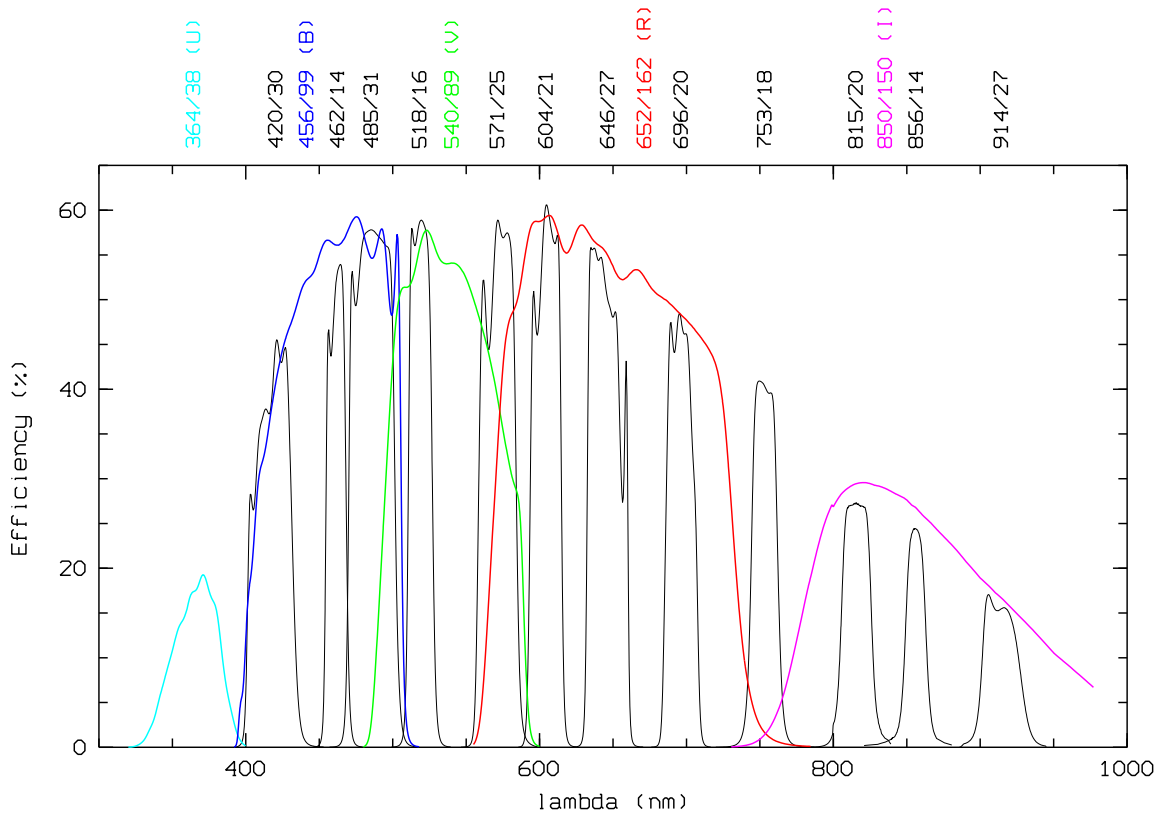


Figure 5.1: Filterset used by COMBO-17. Shown are the total efficiencies over wavelength including the filter, telescope and detector for an average atmosphere at La Silla. Given at top are central wavelength and FWHM of the filters.

Creation of flatfields

This refers only to the images of flatfields which have been processed until this step like the scientific exposures. It is necessary to correct scientific exposures by a flatfield that accounts for the varying illumination across the field-of-view as well as for different gains and sensitivities of the individual pixel of the CCDs. In the most simple case, the exposures are brighter in the center of the field and become fainter to the edges. This has to be corrected for to get proper flux measurements and uniform object detection criteria. To do so, twilight exposures are taken that show the same illumination pattern as the scientific exposures. Dividing the scientific exposures by these flatfields then results in the ideal case in a constant background level across the whole field. Flatfields have to be obtained for each filter separately because the illumination, gains and sensitivities are wavelength-dependent. A set (typically 3-5) of mosaic images is taken and normalized to an average flux value of 1. These images are then coadded into one flatfield by averaging for each pixel over

the counts from the individual images where outliers are excluded. These outliers can be caused by cosmics or stars which have to be removed from the final flatfield. Due to the dithering between the individual exposures for the flatfield, stars will appear on different locations on the frame.

Flatfielding science frames

The science images are divided by the corresponding flatfield. Because the flatfield has been normalized, the flux units are roughly conserved. The mask is applied again to mark all pixel without information.

Special treatment of images

For some filters, special treatment of the images has been necessary. These problems are caused by additional straylight or scattered light on the images which cannot be simply corrected for by the flatfields. So-called superflats are used to model the distribution of this extra light. These superflats are obtained by averaging the science images themselves pixel by pixel with a rejection of outliers. Because objects appear on different positions for dithered images, they will be regarded as outliers and thus disappear. However, very bright and saturated stars are typically so large that they are still visible on the superflats. Therefore, it is very helpful to have images from different fields that can be used for the superflat.

The best known example of where simple flatfielding is not sufficient are fringes which appear on images taken in red filters. Fringes have to be corrected for additively by subtracting a model of the fringe pattern from the images instead of a multiplicative correction as for the flatfielding.

In some filters, we also observed scattered light from the left side of the CCD mosaic. In such cases, one has to try to find the source of the additional light in order to decide if the correction has to be additive or multiplicative. If the additional light appears only on the science frames but not on the flatfields, the correction has to be additive. If the additional light appears on the flatfields, then the multiplicative correction of the flatfielding gets wrong and thus the correction must be multiplicative. If a chosen correction is appropriate or not can in the end only be judged from further quality checks of the photometry, see Sect. 5.2.2.

Some of the medium-band filters lie close to night sky emission lines. Depending on whether the emission lines are bluer or redder than the filter, additional light is let through the filter in the center of the image or in the outer parts. In both cases, a ring-like structure of additional light appears, but once becoming brighter and once becoming fainter towards the center. A special procedure is available within the pipeline that fits the background of images in shells around a given center. These background images are then used for an additive correction of the scattered light.

Cosmic correction and coaddition of sumframes

Finally, for each observing run and each filter, all scientific exposures are coadded into a deep sumframe. The coaddition has to take into account that the images are dithered and thus cannot be simply added pixel by pixel. First, transformations between the individual images have to be determined. This is done for 16 subareas individually of which each has about 2000×2000 pixel or half the size of a CCD. These smaller subareas keep the effects of field rotation small enough so that the derived offsets are accurate within less than 1 pixel across the whole subarea. A reference image is identified which can in principle be any image. However, for practical purposes, it is best to choose an image that has a central position within the dither pattern. On all images and in all subareas bright, unsaturated stars (defined as unresolved objects) are identified. Then, for each subarea, the offset relative to the reference frame is determined automatically. This offset includes only a translation but no rotation. Clearly, the automatic procedure only works if the offset between an image and the reference image is not too large which is fulfilled for images that lie within the dither pattern. Sometimes, too few stars are detected to determine accurate offsets. In that case it is possible to use resolved objects as well. The offsets determined for the 16 subareas should agree within about 2 pixel of their average.

Next, cosmics are removed from the images. This is again done for the 16 subareas individually. For each subarea, all images are compared pixel by pixel considering the proper offsets between the images. Cosmics are identified as pixels having significantly larger flux on only one of the images. They are then removed from this image and the corresponding pixel is assigned a flux value according to the other images that do not have a cosmic at this pixel. The 16 subareas are put together again into a single cosmic-corrected image. For each cosmic-corrected image, an additional image is created that marks the positions of all removed cosmics. These images will later be used in the flux measurement that is not performed on the sumframes but on the cosmic-corrected individual images. Further, they are valuable for checking the cosmic correction. Only images with comparable seeing and exposure time should be used in the cosmic correction. If necessary, the cosmic correction can be done on subsets of all available images, for example for the long and short exposures separately.

For each subarea, the different images are stacked into a deep image. For a proper coaddition one has to consider that the images have different background levels and were taken at different transmissivities of the sky. All images are normalized by first subtracting the background level, then scaling it to the transmissivity of the reference frame and finally adding the averaged background of all images. The proper scalings due to the transmissivities have already been obtained when the offsets relative to the reference frame were determined. These normalized images are then averaged and finally scaled to the sum of the backgrounds of all single images and the sum of the scalings due to the transmissivities. The gaps between the single CCDs vanish in the coadded sumframes.

5.2.2 Data reduction pipeline, part II: Object detection and flux measurements

The second part of the pipeline starts with the coadded sumframes and the cosmic-corrected individual frames and obtains object catalogs with flux and magnitude measurements and colour indices from them. Note that fluxes are not measured on the sumframes but on the cosmic-corrected individual images. Only the deep R -band images are used for the object detection. The sumframes from the other filters are not really needed but are created for the case that checks of e.g. the derived colour indices become necessary. The single steps are the following:

Object detection

The deepest R -band image for each field is used for the object detection. Because of the depth of the R -band, this will give the most complete object list. Only few very red objects should be detectable on redder images but not in the R -band. For the object detection, the software SExtractor (Bertin and Arnouts, 1996) is used. From the resulting object list we will use later the coordinates, the magnitude MAG-AUTO and the morphological parameters (major and minor axis). The object table from SExtractor will be referred to as *master table*.

Transformations between master table and individual frames

The coordinate system of the deep R -band sum image used for the object detection is not the same as the coordinate systems of the individual images due to the dithering and slight positional offsets between the different observing nights. Because the flux measurements are performed on the individual images rather than the deep sumframes, one has to determine transformations between the reference frame and thus the master table and the individual images. This is done in a way similar to the determination of transformations before the coaddition of images. The only difference is that now rotations and scalings between the coordinate systems are also taken into account to allow us an optimal mapping between the coordinate systems. From bright stars, the average PSF is determined.

Measurements of count rates

The next step is to determine for each filter and observing run individually the count rates. For each object in the master table, the corresponding position on the individual image is determined and the counts at this position are measured. If an object is not detectable on a given image then the measurement corresponds just to the background level. The results are stored in a separate table for each image. Taken the average size of the PSF for that image (determined in the step before), all images are smoothed such that the effective PSF is $1.5''$ for all images. This procedure assures that the final flux is measured in the same aperture around an object for all images and filters even if the different images were taken at varying seeing conditions. This is necessary for obtaining correct colour indices later.

Mark stars for calibration

The standard stars for the COMBO-17 fields which are observed by spectroscopy are sometimes brighter than the saturation limit for the long exposures so that the long exposures cannot be used for photometric calibration. Therefore, in each filter, exposures with shorter integration time are taken. These short exposures are calibrated using the spectroscopically observed standard stars. The long exposures are then calibrated using stars that have a high signal-to-noise on the short exposures but are still well below the saturation limit on the long exposures. In this step a routine is applied that automatically determines the reference stars for the calibration. All the routine needs is a minimum signal-to-noise, the saturation limit and the number of reference stars which should be identified. The program then tries to determine an internal minimum signal-to-noise above the given one such that the given number of reference stars is found and that these stars have maximum signal-to-noise but are still below the saturation limit.

Combine tables from individual images

Until this step the pipeline has worked on separate tables for each image from a given filter and observing run. Now these tables are combined into a single table that then contains count rates of the filter and observing run. These tables are referred to as *unite tables*.

Calibration for a given filter

The standard stars are marked in a given unite table. Then the measured count rates are transformed into physical flux measurements using the standard stars and the internal reference stars that were determined before. The flux measurements from the individual frames are averaged into a final flux measurement. The error on the final flux measurement is calculated from the scatter between the individual measurements and takes thus into account not only photon noise but also for example flatfield errors or CCD artifacts. To avoid unreasonably small errors from chance coincidences between the individual flux measurements, the photon noise is assigned whenever the scatter between the measurements would yield a smaller error.

Combine unite tables into final flux table

The unite tables from the different filters and observing runs are combined into one final flux table.

Calculation of colour indices

In this step, the colour indices that are input to the classification are calculated. From the broad-band filters these are the colours $U - B$, $B - V$, $V - R$ and $R - I$. The medium-band filters are combined with the closest broad-band filter, e.g. $420 - B$ or $R - 815$ for the 420/30-filter and the 815/20-filter, respectively.

Quality checks

Before the multi-colour classification is started, some quality checks on the final flux table are performed. First, the magnitude errors as function of magnitude are investigated for the different filters. This should result in a plot like the left panel in Fig. 5.2. The error should increase for fainter objects due to the photon noise. A few variable objects are allowed to have significantly larger magnitude errors than most other objects of comparable brightness. If too many objects have large errors, one must check the previous data reduction steps. Such problems can be caused e.g. by flatfield errors or by wrong transformations between the master table and the individual images on which the flux is measured. This quality check is done for each filter. It is also used to derive the completeness limits.

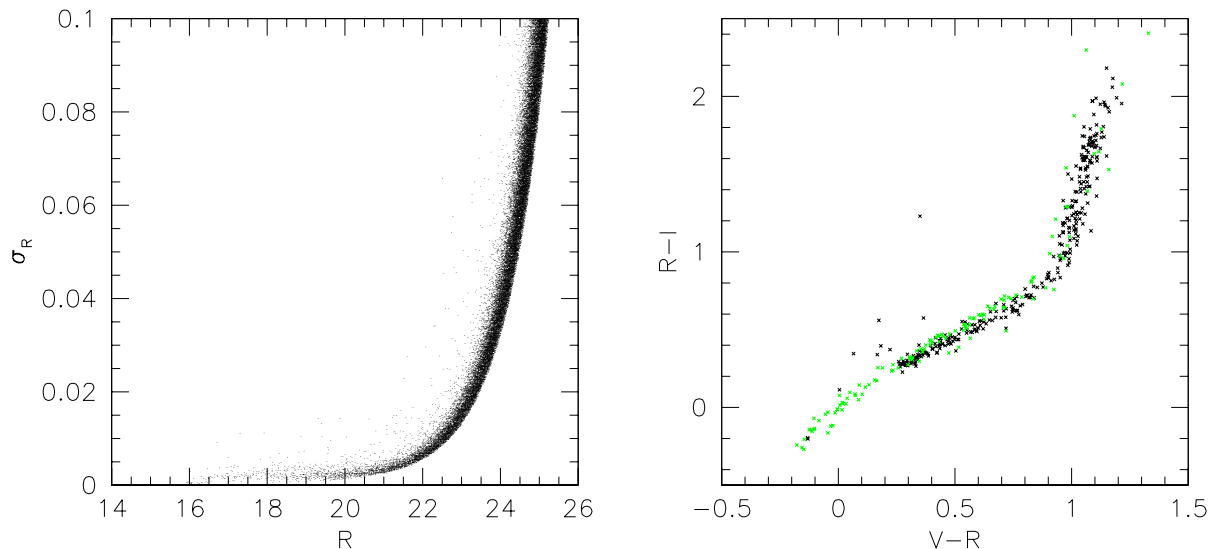


Figure 5.2: Left panel: Magnitude errors in dependence on the R -magnitude. Right panel: Colour-colour diagram of library stars (green) and star-like objects from the flux table (black).

The right panel of Fig. 5.2 shows the stellar main-sequence in a two-colour diagram for stars from the stellar library and for star-like objects from the flux table. If everything went right, the two main-sequences should match and there should be only few outliers which can be double-stars, compact galaxies or quasars. If the main-sequences do not match, one can use different colour combinations to figure out which filter causes the wrong colours. This quality check is done for combinations of all filters.

5.3 Multi-colour classification

In COMBO-17, a total of 17 optical filters (*UBVRI* and 12 medium-band filters) are used to derive spectral classification and redshift estimates. This approach is quite unusual and has thus been tested in simulations and compared to more common multi-colour surveys that only use broad-band filters or fewer medium-band filters (Wolf et al., 2001b). These simulations have been compared to the experience with CADIS (Wolf et al., 2001c) and aimed at developing an optimal survey strategy for the planned COMBO-17 survey. The possibly surprising result is that, when spending the same amount of telescope time on a survey including medium-band filters or on just broad-band filters, the survey including medium-band filters will yield the better classification. Although each filter does not reach as deep as when only using a few broad-band filters, the additional information due to the medium-band filters outweighs this loss and gives more detailed information that can discriminate between different possible object classes.

In Sect. 5.3.1 we will present the object libraries on which the classification is based. Section 5.3.2 then introduces how the different classes are assigned to the objects.

5.3.1 The object libraries

The heart of the classification in COMBO-17 are the object libraries. These are subdivided into three classes: stars, galaxies, quasars. We will present each library with special emphasis to the galaxy library because we are mostly concerned about galaxies in this thesis. Figure 5.3 shows some of the templates used. The libraries are already presented in Wolf (1999); Wolf et al. (2001b, 2003a,b) where also changes in the setup of the libraries are presented. A summary of the libraries finally used will be published after the classification has been finished for all survey fields.

The star library

The basis of the star library is the spectral atlas of Pickles (1998) which contains 131 stars with spectral types ranging from O5 to M8. Most spectra refer to main sequence stars, but some stars with different luminosity classes or metallicities are also included. Spectra of O, B and A stars are left out in the COMBO-17 library because these stars are not expected in an extragalactic survey and would thus more probably lead to wrong classifications than real detections. On the other hand, spectra of white dwarfs, subdwarfs and blue horizontal branch stars have been included.

The star library is not structured as a regular grid in stellar parameters like temperature, surface gravity or metallicity. Such a grid would be essential in a survey aiming at Galactic stars but is not necessary in COMBO-17 which focuses on galaxies and quasars.

The galaxy library

For the galaxy library, template spectra by Kinney et al. (1996) have been used. They used averaged spectra of nearby galaxies to create ten templates. Four templates refer

to quiescent galaxies that have been selected by morphology according to E, S0, Sa and Sb galaxies. Six templates were obtained for starburst galaxies and named SB6 to SB1. The template spectra are shown in Fig. 5.3. The templates cover the wavelength range $\lambda = (125 - 1000)$ nm. Figure 5.3 shows an extrapolation of the templates to the near-infrared (NIR) which has been introduced for CADIS that, unlike COMBO-17, also includes NIR filters. On the blue side, at $\lambda = (290 - 330)$ nm, the template spectra E, S0, Sa and Sb are quite noisy and have therefore been replaced by spectra obtained with the stellar synthesis code PEGASE (Fioc and Rocca-Volmerange, 1997) which have first been matched to the Kinney templates. By interpolation between the ten templates, the galaxy library has been blown up to 100 templates. The interpolation has been performed in a way that the templates are approximately evenly spread in colour-space. Table 5.3 gives the SED numbers that correspond to the original ten templates.

Table 5.3: SED-types of the galaxies. Galaxies are assigned an SED number ranging from 0 to 99. The upper line shows the SED numbers that correspond to the templates published by Kinney et al. (1996). The lower line gives the galaxy type. *B6 to *B1 are starburst galaxies.

SED number	0	15	30	45	75	80	85	90	95	99
template	E	S0	Sa	Sb	*B6	*B5	*B4	*B3	*B2	*B1

Finally, templates have been calculated for different redshifts on an equidistant grid in $\log(1+z)$ which was found to perform better than an equidistant grid in z . 470 steps from $z = 0.0$ to $z = 1.552$ are used. Because no reliable templates are available bluewards of the Lyman- α line and COMBO-17 uses only templates that cover the entire filter range, no redshifts larger than $z = 1.55$ can be assigned. This will probably lead to misclassifications of high-redshift galaxies. However, for statistical investigations of the large class of galaxies, this will be no serious limitation because the galaxy sample will contain mostly galaxies with $z < 1.5$.

The quasar library

The basis of the quasar library is the SDSS QSO template spectrum (Vanden Berk et al., 2001). The library was then constructed by varying three features of quasars: The overall slope of the continuum is changed by multiplying the template spectrum with different power-laws such that features of the template spectrum on small scales are retained. Further, the different strength of emission lines relative to the continuum and the absorption bluewards of the Lyman- α line are varied. Model spectra for quasars at redshifts $z = 0 - 6$ were calculated. As for the galaxies, the redshift grid is equidistant in $\log(1+z)$. It runs from $z = 0.3$ to $z = 5.96$ in 170 steps.

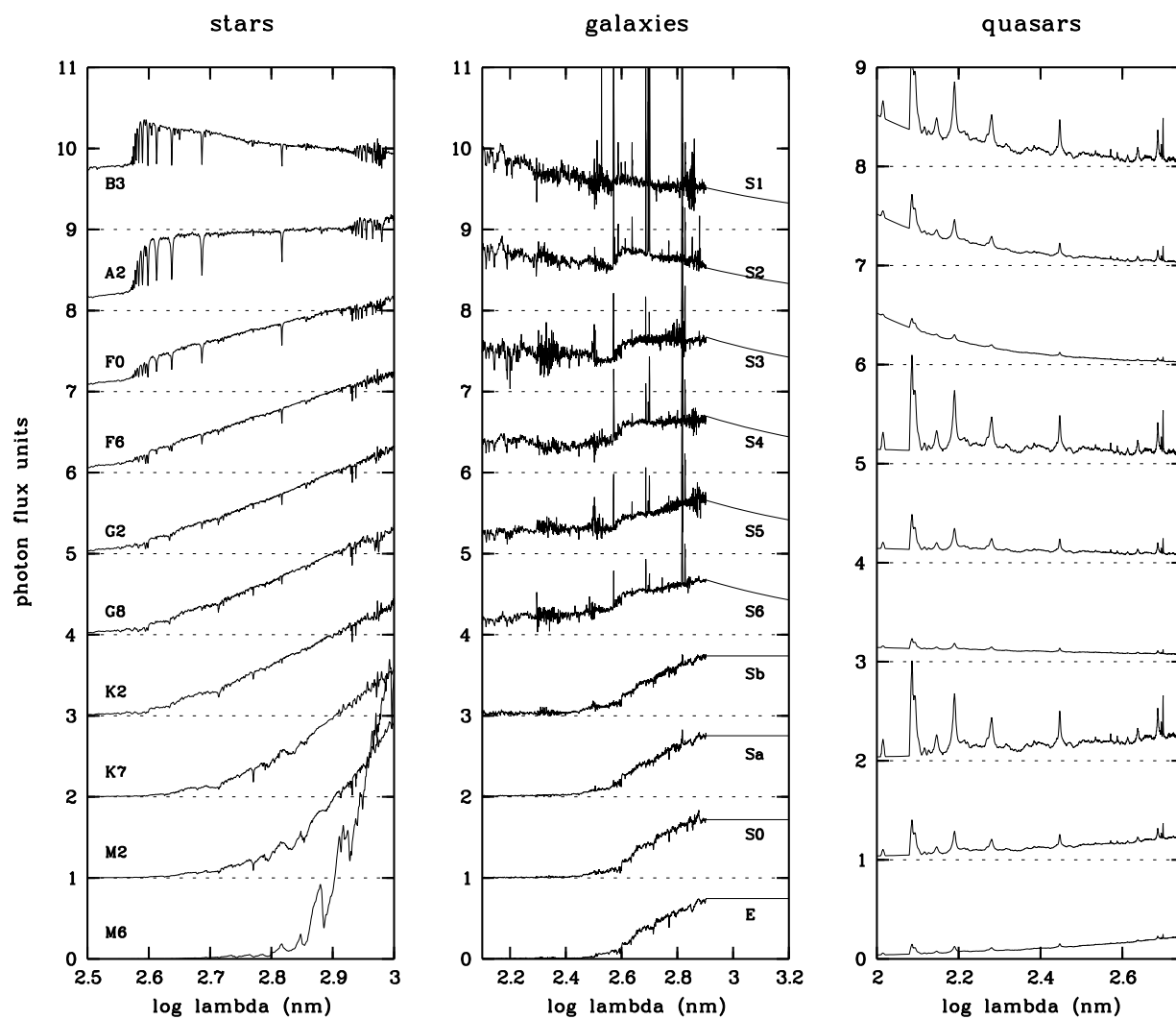


Figure 5.3: Some examples of templates for stars, galaxies and quasars. The Figure is taken from Wolf et al. (2001b).

5.3.2 Template fitting

From the given templates and the total transmission curves of the WFI (see Fig. 5.1), the colour indices that one expects to observe are calculated for all library objects. The classification process then basically consists of comparing the observed colour indices to the theoretical ones and to determine the probability for each template.

Each object is first assigned probabilities that it belongs to the stellar class, to the galaxies or the quasars. Based on these probabilities, nine discrete classes are assigned³

1. definite star: these objects have colours of a star and are unresolved
2. star (galaxy?): these objects are most probably stars but could as well be galaxies, e.g. because they appear extended
3. definite white dwarf (WD), blue horizontal branch (BHB) star or sdB star: these objects are unresolved and have unambiguous colours
4. WD, BHB, sbB (galaxy?): the colours indicate a WD, BHB star or sdB star, but the object is resolved
5. definite galaxy: the colours are those of a galaxy; the shape is irrelevant for this class
6. galaxy (unclassified!): from the colours, no decision is possible; however, statistically these objects are most probably galaxies
7. definite quasar: these objects have colours of quasars and are unresolved
8. quasar (galaxy?): the colours agree with quasars but the object is extended; such objects could be Seyfert 1 galaxies or quasars with a host galaxy
9. strange object: the colours are very strange and do not fit to any of the library templates; these could be interesting astrophysical objects or more probably result from strong photometric artifacts or uncorrected strong variability

To keep contaminants to rare classes like white dwarfs or quasars at a low level, a priori probabilities based on the magnitudes of the objects are incorporated into the assignment. Within a given class, the final assignment of one template is not based on the maximum-likelihood but on the method of minimum error variance (Wolf et al., 2001b). In this approach, the probabilities of all templates of a given class are considered and that template corresponding to the mean of the distribution is assigned. For example, if $P(z_i)$ is the probability that a given object has a redshift z_i , then this particular object is assigned the redshift $z = (\sum z_i P(z_i)) / (\sum P(z_i))$. This method also yields an error estimate on the redshift. However, if the error on the redshift is too large, no template is assigned.

³In the course of improvements, the definition of classes has slightly been changed for object catalogs that are more recent than the ones we use here. The most recent definition of classes is available from <http://www.mpia-hd.mpg.de/COMBO/>

The maximum allowed redshift error $(\Delta z)_{\max}$ is defined as a maximum uncertainty in grid points of the redshift grid; for the galaxies it is 56 grid points. Because the grid is logarithmic, $(\Delta z)_{\max}$ increases with z . For the galaxies, this results in $(\Delta z)_{\max}(z) = 0.118 \times (1 + z_{\max})^{\log(1+z)/\log(1+z_{\max})}$ with $z_{\max} = 1.552$, see also Fig. 7.5.

5.4 Resulting object catalogs

The catalogs used in this thesis are based on a classification from August 2002. However, work is still ongoing on improving the object libraries and thus the classification. Therefore, the catalogs used here will probably not be the final ones.

The data reduction has so far been finished for the A901, S11 and CDFS fields. The classification and redshift estimates have currently only been cross-checked by spectroscopy of a small set of X-ray sources in the CDFS field, some low-redshift galaxies in the A901 field for which spectroscopy has been taken to study the Abell clusters in this field and some objects in the S11 field that overlaps with the 2dF Redshift Survey, see Wolf et al. (2003a,b) for more details. However, as already mentioned, the classification in COMBO-17 is still subject to improvements and a thorough check is still pending.

To give a first idea of the contents of the fields, we give in Table 5.4 an overview of the abundances of the different classes. Figure 5.4 shows the number counts for some object classes as function of R -magnitude.

Table 5.4: Abundances of the different classes in the object tables of those fields for which data reduction has already been finished. Only objects with $R < 24$ are used. The classes are described in more detail in Sect. 5.3.2. Note that, due to varying completeness levels, this Table cannot be used to infer the physical abundances of the different object classes.

	Class	A901	S11	CDFS	all 3 fields
(1)	star	2435	1782	1171	5388
(2)	star (gal?)	615	905	903	2423
(3)	WD	18	12	12	42
(4)	WD (gal?)	0	1	4	5
(5)	galaxy	18326	15764	12485	46575
(6)	galaxy (uncl!)	1166	1084	1008	3258
(7)	QSO	82	58	73	213
(8)	QSO (gal?)	59	53	87	199
(9)	strange object	68	37	28	133
	all classes	22769	19696	15771	58236

Table 5.4 and Fig. 5.4 show that galaxies are the dominating population in the data set. The Figure also shows that stars are only more abundant than galaxies at bright magnitudes (about $R < 19$). For $R < 23$, basically all galaxies are assigned a redshift estimate while at fainter magnitudes the classification becomes incomplete. We note that for the different

scientific applications of COMBO-17, redshifts and spectral classification are only used for objects brighter than $R = 24$ because simulations have shown that at fainter magnitudes the classification becomes too unreliable.

In Sect. 7.2.1 we will present in more detail the properties of the galaxy population for the object catalogs which will finally be used for the galaxy-galaxy lensing measurements. These will be merged from the catalogs provided by COMBO-17 and additional ones obtained from new sum images, see also Sect. 6.1

5.5 Contribution to COMBO-17 from this thesis

A large project like COMBO-17 with almost 50 nights of observations on a wide-field camera can clearly only be carried out in a collaboration. At the beginning of this PhD project, the COMBO-17 project had just obtained its first observations and started with the data reduction. Therefore, I was actively involved in all steps of data acquisition, data reduction, quality checks and classification which was the main content of the first year of my PhD work. I participated in two observing runs in the year 2000 of which one was carried out solely by myself.

The data reduction pipeline is based on tools that were already developed for the similar CADIS project. I actively participated in the adaptation of the existing software to the special requirements of the COMBO-17 data set which included programming of routines in MIDAS, checks and error searches. In the first year of work on data reduction, I did a substantial fraction of it including reduction of broad-band filters and some medium-band filters which showed non-standard problems due to e.g. night-sky emission lines or scattered light from various origins. Because the data reduction just started, I was also involved in developing solutions for these problems.

The first runs of the different steps of the second part of the pipeline were carried out by myself including tests, search for potential problems and the development of a script that allows one to perform the steps automatically. After the first fully classified flux tables were available and most of the further data reduction and classification could be carried out more routinely, I stopped the intense work on it and started working on shape measurements and the actual lensing analysis. However, for quite some time I remained involved in the data reduction and helped with emerging problems.

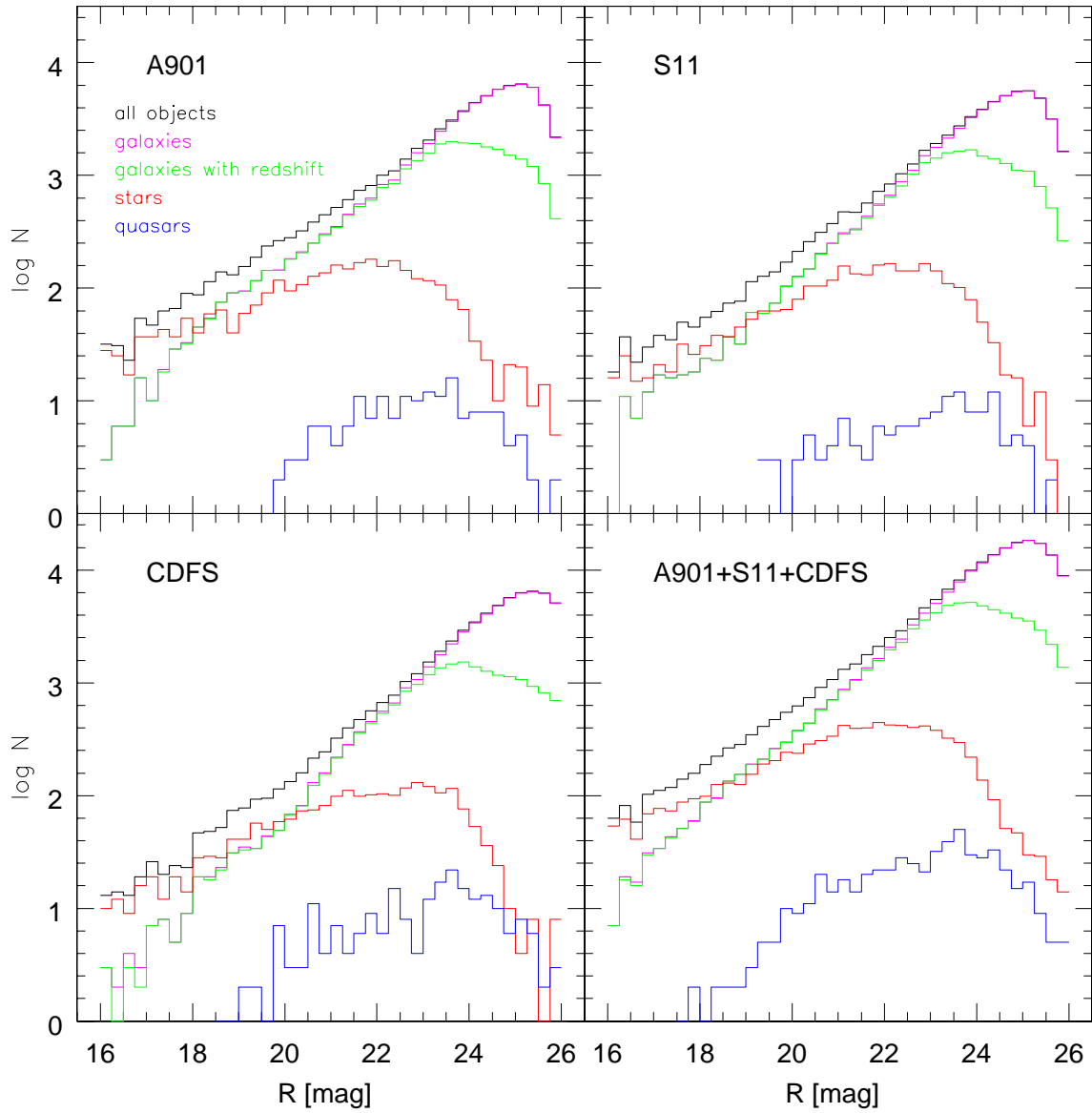


Figure 5.4: Number counts for some object classes as function of R -magnitude for the A901, S11 and CDFS fields individually and for all three fields together. ‘galaxies’ denotes the classes (5)+(6), ‘stars’ the classes (1)-(4) and ‘quasars’ the classes (7)+(8), see also Table 5.4.

Chapter 6

Shape measurements of faint objects

In Sect. 3.2 we introduced the measurement of shapes of galaxy images from the second moments of the light distribution. In practice, however, these measurements are complicated because images of detected objects appear for several reasons distorted on astronomical images. First, even in perfect observing conditions (e.g. no PSF, optimal focus and telescope optics) the images are affected by the pixelization which is unavoidable for CCD images. In particular, images of faint and small objects cover only a few pixels from which the shape parameters have to be derived. Further distortions arise in the telescope optics: the focus is not always perfect and for wide-field cameras the optimal focus is often dependent on the image position. The resulting defocussing and other defects in the telescope optics as well as guiding errors change the shapes of images in a complicated way. Of high importance for ground-based observations is also the blurring by the atmosphere which is called *seeing*. Due to this blurring, images of point-like sources (mostly stars) appear extended. The FWHM of a Gaussian fit to the stellar object quantifies the seeing, usually it is around $0.8''$ in our observations that are used for shape measurements. Extended objects are also affected by the seeing such that they appear rounder than without seeing. All these distortions are summarized in the point-spread function (PSF). Anisotropies in the PSF produce coherent elongations of objects and can thus mimic gravitational shear. Images of unresolved objects that should ideally be point-like can be used to trace the shape of the PSF across the field-of-view and to derive corrections. Because the PSF varies smoothly, it can be fitted by a low-order polynomial across the whole field. The size of the PSF is wavelength-dependent, it is smaller for longer wavelengths. Therefore, typically observations in red filters, in which galaxies also appear smoother and more compact, are used for weak lensing studies.

In the following we will refer to the distortions just described as *observational distortions* and thus distinguish them from the *gravitational distortions* which are due to lensing. The goal of the shape measurement is to correct for the observational distortions which then allows one to measure the gravitational distortions. How we measure shapes and correct for the observational distortions is presented in Sect. 6.2.

An important precondition for accurate shape measurements is to have a proper sumframe available that introduces as little extra distortion in the process of coaddition as possible.

The sumframes from COMBO-17 which were described in Sect. 5.2.1 are not optimal for that purpose because they do not allow for subpixel shifts or rotation between the individual frames. Therefore, for each field, a new sumframe from the R -band exposures has been produced using a pipeline that is optimized for shape measurements of faint galaxies. The pipeline will be presented in Sect. 6.1. Using this pipeline has the additional advantage over the coaddition in COMBO-17 that, for multiple observing runs, frames from all runs can be coadded into one even deeper sumframe. For COMBO-17 this was not possible because between some observing runs the instrument was slightly rotated during service works on the telescope.

For the CDFS field, observations from six different epochs by three different collaborations are available. This provides a unique data set for a thorough check of the quality and reliability of the shape measurements because it is possible to compare the shape measurements of individual objects from several independent sumframes with very different exposure times and seeing conditions. In Sect. 6.3 we present this comparison and its results.

6.1 Proper sumframes for shape measurements and object detection

Typically, shapes are measured on deep coadded sumframes which have a better signal-to-noise than individual images with shorter exposure times. To not introduce additional distortions, it is important to do the coaddition of the single images in a way that is optimized for shape measurements. A pipeline has been developed within the lensing group at the University of Bonn and was used to create sumframes from the deep R -band data of COMBO-17. It was specifically developed for data from multi-chip cameras like the WFI with 2×4 chips. Schirmer et al. (2003) describe the pipeline in detail, so we will only summarize the most important steps here.

The raw data are processed in a standard way including debiasing and flatfielding using skyflats. These steps are performed on the single chips. From the images of each observing run superflats are calculated. When available, images from other COMBO-17 fields that were observed at the same time are also used which improves the quality of the superflats in the regions around saturated stars. The superflats are then used for an illumination correction and fringe subtraction.

Before the coaddition, an astrometric solution has to be obtained that determines the offsets and orientations of the different chips relative to some coordinate system and that is needed for combining the single images. Objects detected on more than one chip due to the dithering are used to calculate the astrometric solution for the CCD mosaic. The USNO-A2 astrometric reference catalog is then used to determine the position of the field with respect to absolute sky coordinates. The transformations between the chips can be determined very accurately with residuals of only 0.1 pixel while the global coordinate system with respect to absolute sky coordinates is only accurate to about 1 pixel due to

the lower accuracy of the reference catalog.

Using the astrometric solution, individual images are stacked into sum images. This is done with the *EIS drizzle* algorithm¹ that allows matching of the individual frames on a subpixel scale and thus accounts for rotation between frames or misalignment of chips. Additionally, a weight image is produced which contains, for each pixel of the coadded image, information on the noise properties as they can be derived from the individual images that contribute to the flux determination of this pixel. Due to e.g. saturated stars, gaps between the chips, satellite tracks or bad pixels the noise properties vary across the field.

To create an object list we run SExtractor on the sum images. The weight images are used to trace the local noise properties. This suppresses spurious detections in the regions around bright stars very efficiently, see Fig. 6.1. We do not apply further masking of objects. The object list from SExtractor is then used as input to routines which measure the shapes of the objects, see Sect. 6.2. From SExtractor, only the positions, magnitudes and radii of the objects will be used. We will refer to these object lists as *shape catalogs* and thus distinguish them from the COMBO-17 catalogs that were introduced in Sect. 5.4.

6.2 Measuring and correcting shapes of faint objects

For the detected objects we measure shapes using the so-called KSB algorithm developed by Kaiser et al. (1995) with some modifications and corrections provided by Luppino and Kaiser (1997); Hoekstra et al. (1998) and Hudson et al. (1998). The algorithm is summarized in Bartelmann and Schneider (2001). In the following we will only describe the most important steps and illustrate them for the CDFS sum image as an example. We use the implementation of the KSB algorithm in the software *imcat*².

Ellipticities are calculated from weighted second order moments Q_{ij} of the light distribution $I(\theta)$

$$Q_{ij} = \int d^2\theta W(\theta)\theta_i\theta_j I(\theta) \quad (6.1)$$

Here θ denotes the position angle with respect to the object center, W is a weight function and $I(\theta)$ the surface brightness at position θ . This differs from the definition of the second moments in Eq. (3.19) where no weights are used. The reason for using a weight function is that the integrals in Eqs. (3.19) and (6.1) extend formally to infinity. However, at some distance from the center of an object, one will only measure sky noise which gets down-weighted in Eq. (6.1). Further, objects are not isolated on CCD images so that the integral without weight function will be influenced by (in projection) neighbouring objects. Although the weight function will not completely eliminate the contribution from neighbouring objects, it will reduce this contamination substantially. We use a Gaussian with the half-light radius of an object (determined by SExtractor) as window scale.

¹<http://www.eso.org/science/eis>

²available at <http://www.ifa.hawaii.edu/~kaiser/imcat>

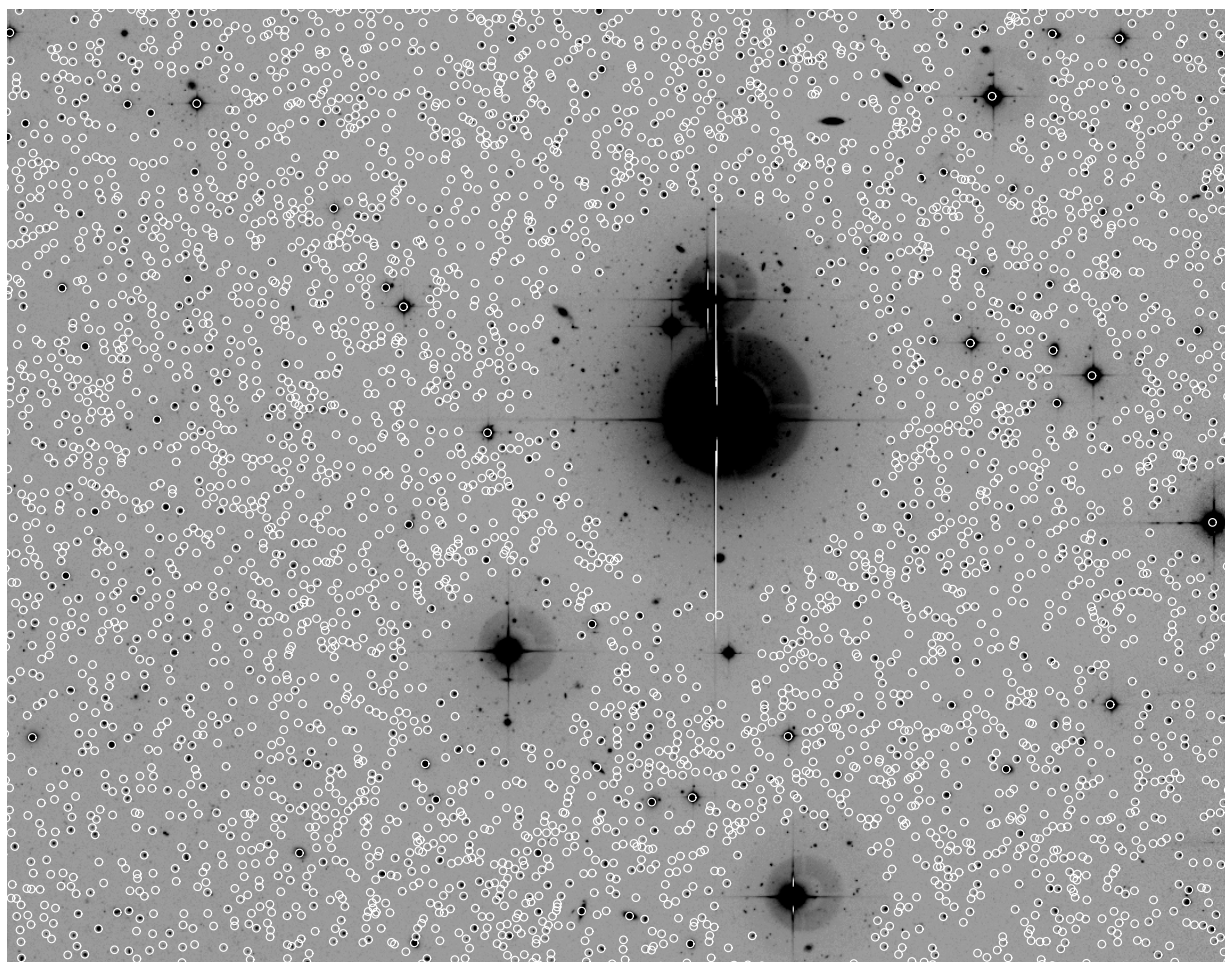


Figure 6.1: Region around a bright star. Marked are all objects in that region that are detected by SExtractor when the weight map is used to trace the noise properties of the sumframe.

The complex ellipticity $\chi = \chi_1 + i\chi_2$ is calculated from the second order moments Q_{ij} as in Eq. (3.20), but due to the weighting in Eq. (6.1) the relations derived for the complex ellipticities in Sect. 3.2 do not hold for the complex ellipticities used here. It is possible to correct the measured ellipticity for the observational distortions by using the shapes of stellar objects as tracers. Stellar objects should ideally be point-like but get distorted in the same way as extended objects. Therefore, the PSF of stellar objects traces the observational distortions as a function of position on the image. Combining the PSF information from stars across the whole field allows one to derive the PSF pattern, that is the size and orientations of ellipticities induced by the PSF into images of stellar objects. Stellar objects are selected from a radius-magnitude-diagram and used to trace the point-spread function across the field, see Fig. 6.2. In such a diagram, stellar objects are easily identified because, due to their point-like nature, all stellar objects have the same radius which is given by the PSF. Stellar objects lie on a sequence of constant radius. At its bright end, the radius of the objects increases which is due to the saturation. The stellar sequence is determined by an automatic procedure which selects objects in a given range of signal-to-noise. We choose $70 < S/N < 10000$ which yields stellar objects with $1.55 < \theta_h < 2.15 \equiv \theta_{h,\min}$ and $22.79 < mag < 28.35$ for the CDFS sum image. Here, θ_h denotes the half-light radius in pixel determined by *imcat* and *mag* is an uncalibrated magnitude from the *imcat* software. $\theta_{h,\min}$ is the maximum half-light radius of objects on the stellar sequence. We will later take $\theta_{h,\min}$ as minimum radius of objects from which we will use the shape measurements in our lensing studies, see Sect. 7.1. In the following, we will refer to all objects with $\theta_h > \theta_{h,\min}$ as *resolved* and to those with $\theta_h \leq \theta_{h,\min}$ as *unresolved*. We will use the notation θ for projected angular distances and thus distinguish them from projected proper distances r .

The left panel of Fig. 6.3 shows the PSF pattern that results from the selected stellar objects. Note that no transitions in the PSF pattern at the edges of the CCD chips are seen. A second-order polynomial is fitted to the ellipticities of the stellar objects across the whole field (middle panel) and used to correct for the anisotropies of the point-spread function [see Eq. (6.2)]. The right panel of the Figure demonstrates that overall structures in the PSF pattern are eliminated or at least substantially reduced. The anisotropy-corrected ellipticities χ^{aniso} are related to the measured ellipticities χ by

$$\chi^{\text{aniso}} = \chi + P^{\text{sm}} q^* , \quad (6.2)$$

where P^{sm} is the *smear polarizability* tensor and q^* the stellar anisotropy derived from the stellar objects. The smear polarizability can be measured for each object from the third and fourth moments of its light distribution, see Bartelmann and Schneider (2001) for details. Figure 6.4 shows the ellipticities of stellar objects before and after the correction. The mean ellipticity becomes zero after the correction and the scatter in the ellipticities is reduced.

Similar to the smear polarizability, the shear polarizability P^{sh} is calculated. P^{sh} quantifies how much the ellipticity of an object is changed by gravitational shear in the absence of PSF effects. Because of the weighting in Eq. (6.1), P^{sh} and P^{sm} are non-trivial and depend

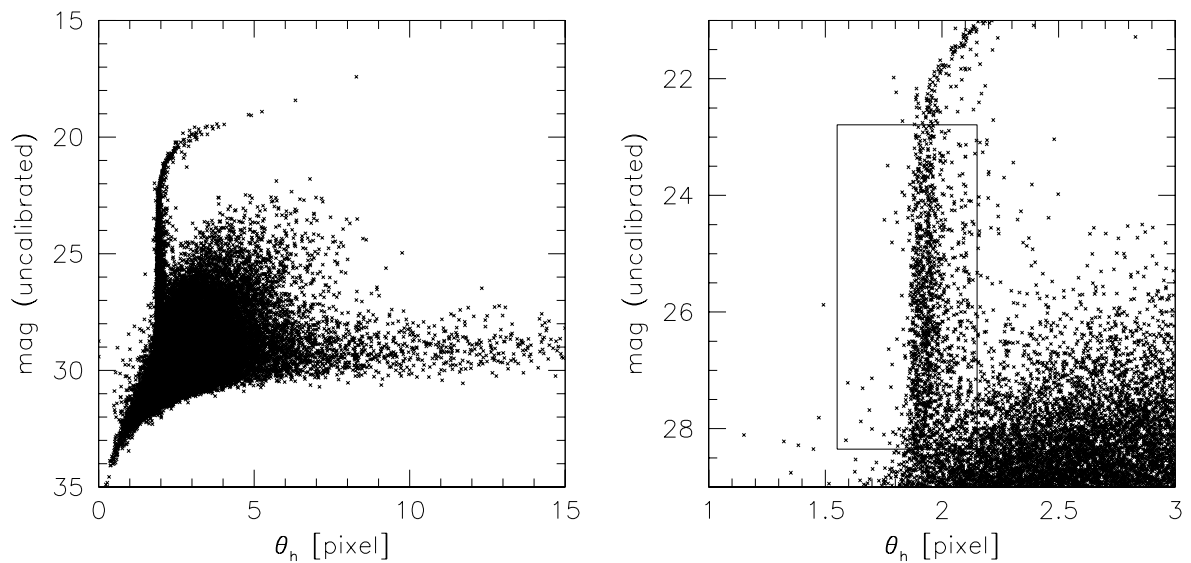


Figure 6.2: Radius-magnitude diagram for the CDFS sum image. The magnitude is not calibrated. The right panel shows a zoom-in of the left panel. The stellar objects selected are marked by the box.

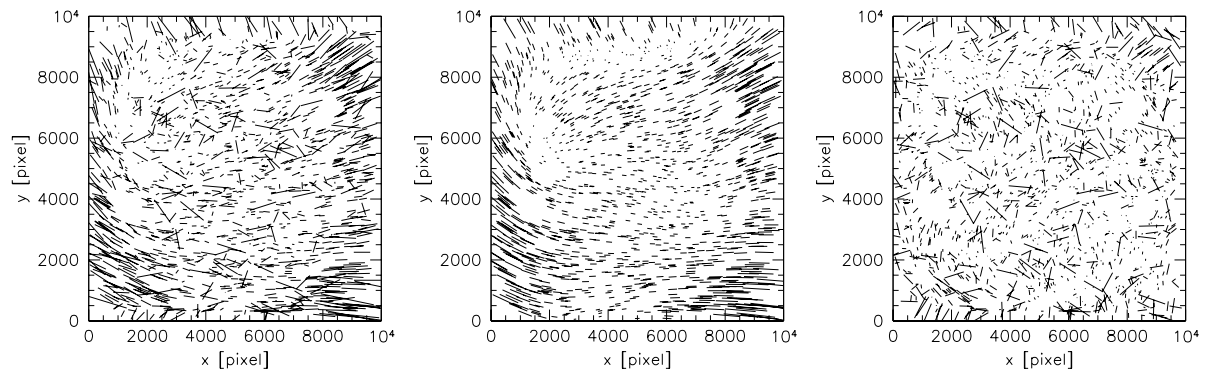


Figure 6.3: PSF pattern for the CDFS sum image. At the position of each stellar object a bar is plotted which is oriented along the major axis of the object and has a size of 20000 times its ellipticity. The left panel shows the PSF pattern before any correction is applied. The middle panel shows a second order polynomial fit to the pattern and the right panel shows the residuals that are left over after subtracting the model from the data.

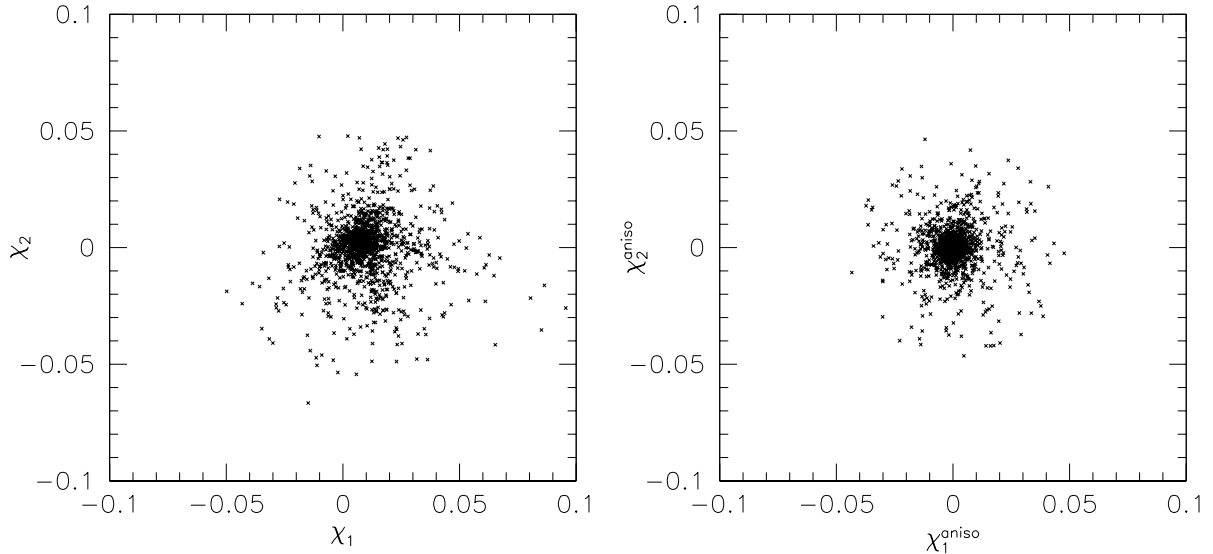


Figure 6.4: Ellipticities of stellar objects before and after the anisotropy correction. Before the correction, the mean ellipticity is $\chi_1 = 0.009 \pm 0.014$ and $\chi_2 = 0.000 \pm 0.014$ while after the correction it is $\chi_{\text{aniso},1} = 0.000 \pm 0.009$ and $\chi_{\text{aniso},2} = 0.000 \pm 0.010$.

on the weight function W . To get an estimate of the reduced shear g one also has to correct for the isotropic part of the PSF which makes images rounder. However, the effect is dependent on the size of the galaxies; large galaxies are less affected than smaller ones. The reduced shear is related to χ^{aniso} by

$$\langle g \rangle = \langle (P^g)^{-1} \chi_{\text{aniso}} \rangle \quad (6.3)$$

with

$$P^g = P^{\text{sh}} - P^{\text{sm}}(P^{*\text{sm}})^{-1}P^{*\text{sh}} \quad (6.4)$$

where the quantities with asterisks are determined from the stellar objects only. Remember that in the case of galaxy-galaxy lensing $g \approx \gamma$. Equation (6.3) holds only when averaging over several objects because in its derivation it has been used that the expectation value for the intrinsic ellipticities of galaxies (meaning without observational or gravitational distortions) is zero. Equation (6.3) applied to a single object gives an estimate of the ellipticity ϵ that would have been measured without observational distortions (but including the gravitational distortions):

$$\epsilon = (P^g)^{-1} \chi_{\text{aniso}} . \quad (6.5)$$

Note that we switched the notation of the ellipticity from χ to ϵ because $(P^g)^{-1} \chi_{\text{aniso}}$ is more similar to the ellipticity ϵ defined in Sect. 3.2 and $g \approx \gamma$ is related to the ellipticities χ and ϵ defined without weighting in Section 3.2 by Eq. (3.30); $g \approx \langle \epsilon \rangle$, but $g \approx \langle \chi \rangle / 2$. It

is this ϵ from Eq. (6.5) that we will refer to in the following when talking about ellipticities or shapes of objects.

Finally, each object is assigned a weight referring to its shape measurement. This is necessary because for some objects the applied corrections can become fairly large which renders their final ellipticity measurement quite uncertain. Such objects have to be down-weighted against objects with more reliable shape measurements in a lensing analysis in order to improve the signal-to-noise. Erben (2000) and Erben et al. (2001) have analysed shape measurements from simulated data to develop a weighting scheme that we will apply here. We select for each object its 20 closest neighbours in $\theta_h - S/N$ space. We measure the standard deviation σ_ϵ^w of the ellipticities from these neighbours and assign the weight $w = 1/(\sigma_\epsilon^w)^2$ to the corresponding object. For small or noisy objects where shapes cannot be measured accurately, the shear estimates will be more noisy and thus unrealistically high in more cases. For these objects the scatter will be highest and correspondingly the weight will be smallest. Also for well-resolved objects with reliable shape measurements, a nonvanishing standard deviation will be measured. But for these objects it will be dominated by the intrinsic ellipticity distribution of the galaxies and therefore yield the same weight for all of these objects. However, using real data, we found that there are always some objects having very high ellipticities ($\epsilon_i \gg 1$) such that the standard deviations measured for neighbouring objects in $\theta_h - S/N$ space are overestimated and thus the weights underestimated. We found that the weighting scheme is much improved by excluding all objects having $\epsilon_{1,2} > 1.5$. In the next Section we will test in more detail the performance of this weighting scheme.

6.3 The reliability of shape measurements

Accurate shape measurements lie at the heart of all weak lensing studies which have become an important tool in studying the dark matter distribution in galaxies, clusters or the large-scale structure. However, the distortions from gravitational shear are small in all these cases while the observational distortions due to pixelization, noise and seeing are of comparable size. Therefore, it is crucial to know how well algorithms like the KSB algorithm, that are used for correcting the shape measurements for observational distortions can recover the ‘real’ shapes of galaxy images. Erben (2000) and Erben et al. (2001) used simulated data to test the KSB algorithm and derived an optimized weighting scheme that we introduced in Sect. 6.2. However, simulated data always have to rely on simplifying assumptions about the distorting effects. Therefore, it is important to also test the algorithm on real data. We use observations of the CDFS field from three different surveys to create seven independent sumframes with very different exposure times and seeing conditions and compare the shape measurements from these images on an object-by-object basis. This allows us to investigate the importance of observing time and seeing conditions (Sect. 6.3.2) and to test the weighting scheme proposed by Erben et al. (2001). In Sect. 6.3.3 we show how the scatter in the shape measurements from independent sumframes depends on the observational properties of the objects, e.g. on magnitude or half-light radius.

In Sect. 6.3.4 we check if shape measurements are still reliable when performed on a sumframe that is coadded from images with very different seeing conditions and PSF patterns. The galaxy-galaxy lensing signal obtained from the different sumframes is compared in Sect. 6.3.5. Finally, in Sect. 6.3.6 we summarize our results.

6.3.1 The data

The observations are taken from COMBO-17³, the ESO Imaging Survey (EIS)⁴ and the GOODS project⁵. Each survey imaged the CDFS field in R using the WFI. We stacked the data into seven independent sumframes and additionally all data into one deep frame. The deep frame amounts to more than 15 hours exposure time. We will refer to the independent sumframes as B1 to B7 and to the deep sumframe as ‘deep’. Table 6.1 gives an overview of the observing periods, exposure times and seeing conditions for the different sumframes that were created from the data using the pipeline described in Sect. 6.1. The exposure times and the seeing vary substantially for these images.

Table 6.1: Observational characteristics of the sumframes used.

Survey	Name	Epoch	Exposure (s)	PSF ($''$)
COMBO-17	B1	10/99	14230	0.81
EIS	B2	12/99	6600	0.89
COMBO-17	B3	02/00	3000	0.81
COMBO-17	B4	02/00	5000	0.73
COMBO-17	B5	09/00	8500	0.96
COMBO-17	B6	01/01	3000	1.11
GOODS	B7	11/01	17000	1.04
	deep		57140	0.89

For each sumframe, we perform the shape measurements and the corrections as described in Sect. 6.2. Figure 6.5 shows the PSF patterns for each sumframe. Note that the unresolved objects selected for tracing the PSF pattern are not necessarily the same for the individual sumframes. The resulting PSF patterns are quite different so that it is not clear at all if the correction procedure works well on the deep sumframe which is a mixture of the different PSF patterns.

In Table 6.2 we give the size of the PSF anisotropy for the different sumframes and the residuals that are left after the anisotropy correction.

³<http://www.mpia-hd.mpg.de/COMBO/>

⁴<http://www.eso.org/science/eis/>

⁵<http://www.eso.org/science/goods/>

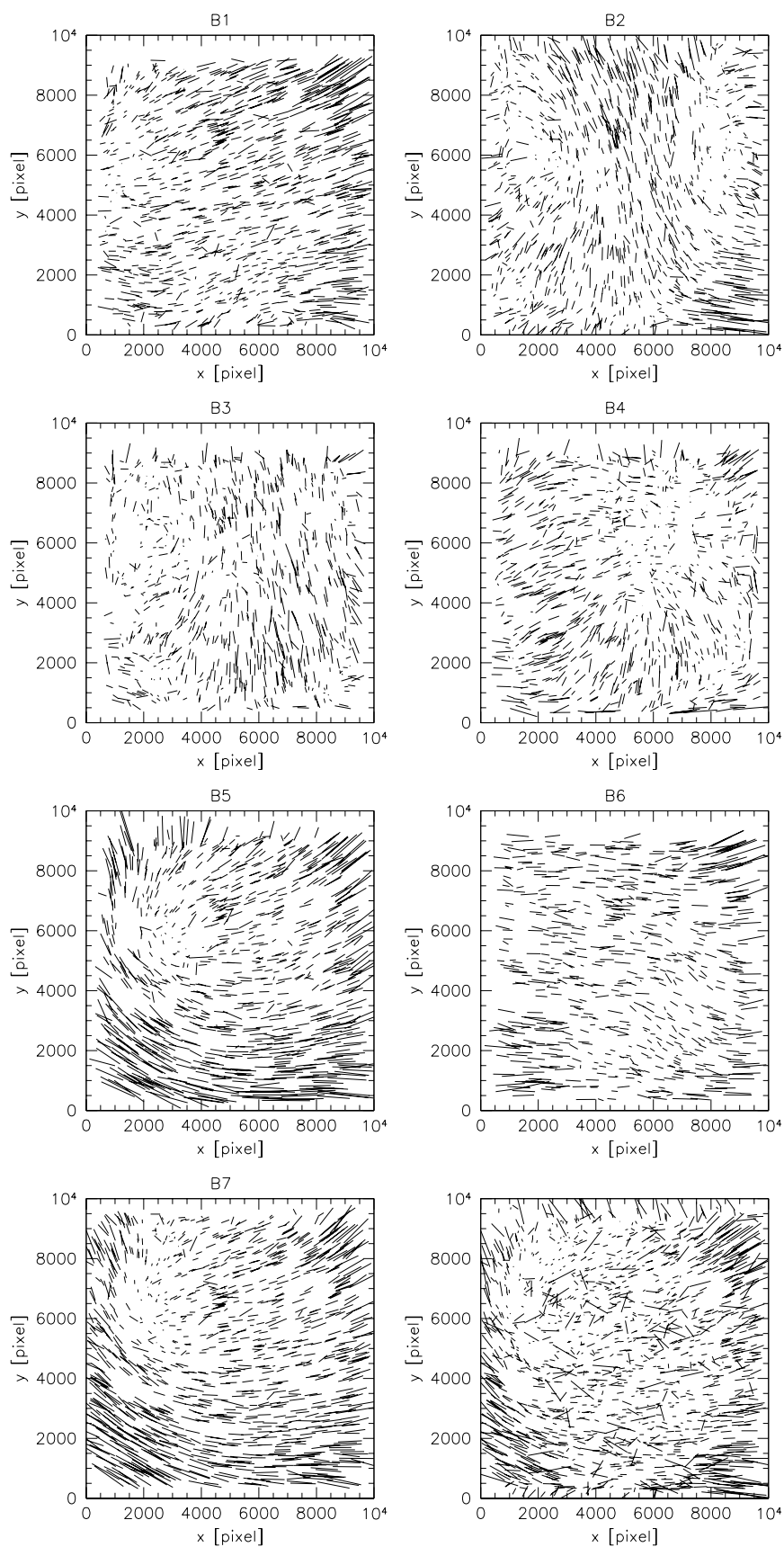


Figure 6.5: Same as the left panel of Fig. 6.3 but for the sumframes B1 to B7. The PSF pattern of the deep sumframe is also shown in the lower right panel.

Table 6.2: Stellar ellipticities before and after the anisotropy correction. After the correction, the mean ellipticities are zero.

	before correction				after correction	
	$\langle \epsilon_1 \rangle$	$\sigma(\epsilon_1)$	$\langle \epsilon_2 \rangle$	$\sigma(\epsilon_2)$	$\sigma(\epsilon_1)$	$\sigma(\epsilon_2)$
B1	0.013	0.010	0.009	0.010	0.006	0.006
B2	-0.003	0.015	-0.003	0.010	0.007	0.007
B3	-0.008	0.011	-0.002	0.008	0.008	0.008
B4	0.004	0.013	0.005	0.009	0.010	0.005
B5	0.014	0.021	0.001	0.019	0.009	0.007
B6	0.019	0.011	-0.002	0.009	0.007	0.005
B7	0.015	0.014	-0.001	0.018	0.006	0.005
deep	0.009	0.014	0.000	0.014	0.009	0.010

6.3.2 Influence of exposure time and seeing

First, we compare the shape measurements of sets of only two sumframes. We choose the sumframes such that the effect of different exposure time and seeing can be investigated independently. Sumframes B1 and B3 have similar seeing but very different exposure times while B3 and B6 have the same exposure time but very different seeing. For the objects common to both object lists we compare the corrected ellipticity components as measured on the two corresponding sumframes. We find 15801 objects common to B1 and B3 and 10401 objects common to B3 and B6. Fig. 6.6 shows that the shape measurements from the two sumframes with comparable seeing but different exposure time agree very well and just show some scatter due to the measurement errors. However, in the case of similar exposure time but different seeing conditions, the ellipticities are systematically larger when measured on the sumframe with the larger seeing, see Fig. 6.7.

We quantify the relation between the ellipticities measured on the two sumframes by fitting straight lines to the distributions shown in Figs. 6.6 and 6.7. We use the routine *fitxy* from the *Numerical Recipes* (Press et al., 1992) that takes errors in both coordinates into account. As error estimate on the ellipticities we use $\sigma_\epsilon^w = 1/\sqrt{w}$ where w is the weight for each object from the shape measurement on the corresponding sumframe, see Sect. 6.2. For different exposure times but comparable seeing we find

$$\epsilon_1(\text{B3}) = (1.0759 \pm 0.0237)\epsilon_1(\text{B1}) - 0.0092 \pm 0.0034 \quad (6.6)$$

$$\epsilon_2(\text{B3}) = (1.0550 \pm 0.0232)\epsilon_2(\text{B1}) - 0.0252 \pm 0.0033 \quad (6.7)$$

while at constant exposure time but different seeing the best fit is

$$\epsilon_1(\text{B6}) = (1.3458 \pm 0.0478)\epsilon_1(\text{B3}) + 0.0256 \pm 0.0052 \quad (6.8)$$

$$\epsilon_2(\text{B6}) = (1.3025 \pm 0.0457)\epsilon_2(\text{B3}) - 0.0018 \pm 0.0051 \quad (6.9)$$

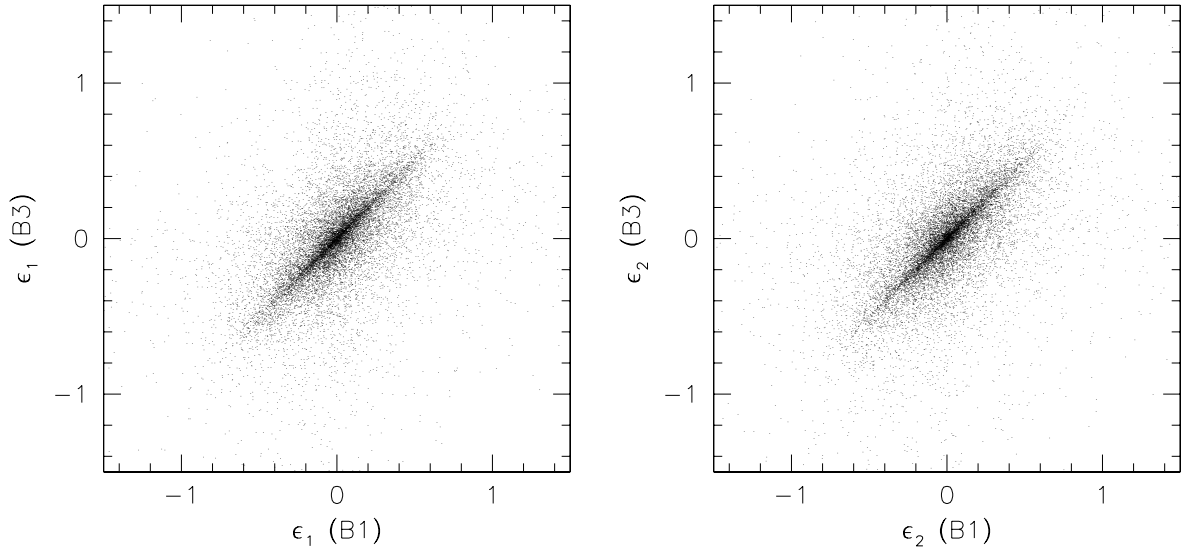


Figure 6.6: Comparison of the recovered ellipticities for objects detected on B1 and B3. The left panel shows the ϵ_1 -component and the right panel the ϵ_2 -component.

In both comparisons, the measured ellipticities are larger on average for the more noisy frame, see also Fig. 6.8. However, the huge difference in exposure time only increases the recovered ellipticities by about 7% for those objects that are detected on both sumframes while in the sumframe with bad seeing the recovered ellipticities are about 30% larger. Figure 6.7 shows that, although on average the ellipticities of the objects are larger when measured on B6 than on B3, for a substantial fraction of objects the two measurements still agree quite well. Therefore, the question arises how one can select those objects for which the shape measurements are reliable. We will investigate this question in more detail below when analyzing the scatter in the shape measurements from the sumframes B1 to B7. Here we only illustrate the influence of some quantities by splitting the sample into approximately two halves according to the half-light radii θ_h , signal-to-noise S/N , correction factor P^g or weight w of the objects and showing the relation between the ellipticity measurements for these subsamples. Figure 6.9 shows that all these quantities have an effect on the shape measurement and can in principle be used to select objects with reliable shape measurements. In Table 6.3 we quantify again the relation between the two ellipticity measurements by fitting a straight line to the distributions.

6.3.3 Scatter in the shape measurements between all independent sumframes

Now we take objects common to the independent sumframes B1-B5, B7 and investigate how the measurement errors depend on e.g. magnitude, half-light radius or signal-to-noise.

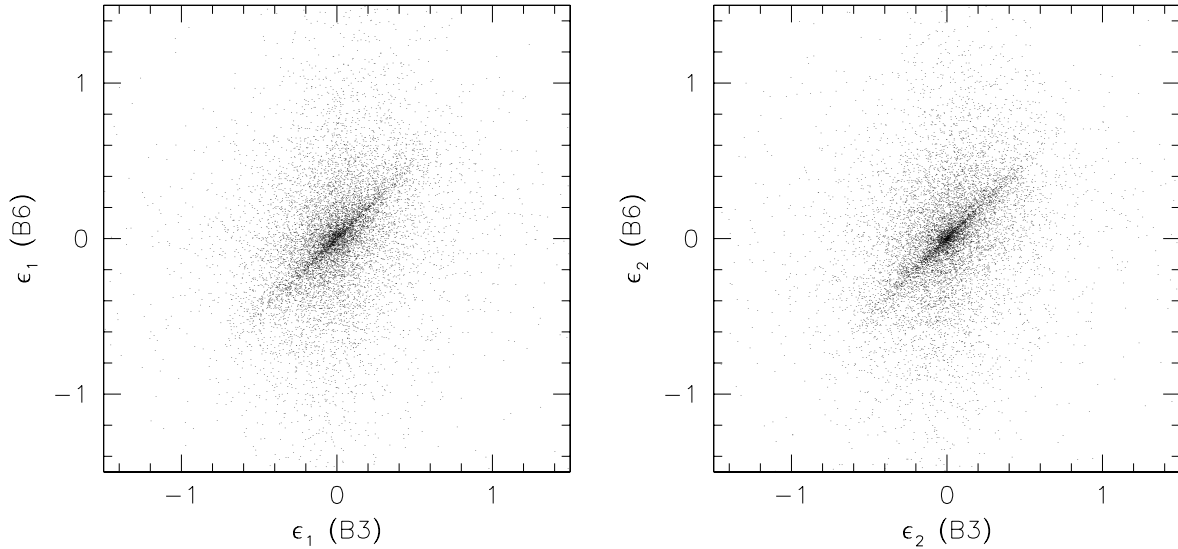


Figure 6.7: Same as Fig. 6.6 but for the sumframes B3 and B6.

We find 11403 objects common to these six frames. We leave out B6 because we do not want to be limited by its bad seeing and short exposure time. For each object we calculate the standard deviations σ_{ϵ_1} and σ_{ϵ_2} in ϵ_1 and ϵ_2 from the six independent measurements. From these we calculate the standard deviation $\sigma_\epsilon = (\sigma_{\epsilon_1}^2 + \sigma_{\epsilon_2}^2)^{1/2}$. Figure 6.10 shows a histogram over σ_ϵ for all objects and for subsamples of resolved and unresolved ones separately. The median of σ_ϵ for all objects is just $\sigma_\epsilon = 0.16$.

Figure 6.11 shows how σ_ϵ for resolved and unresolved objects depends on magnitude, signal-to-noise, half-light radius, correction factor P^g , ellipticity ϵ and the estimated uncertainty σ_ϵ^w in the ellipticity of the objects. For resolved objects, σ_ϵ is a strong function of magnitude, signal-to-noise, correction factor, ellipticity and the weights. As function of ellipticity, σ_ϵ is first only slowly rising, but at $\epsilon \approx 0.7$ the rise becomes steeper. A possible explanation is that ellipticities below 0.7 are still physical while those above 0.7 are not. Therefore, objects with $\epsilon > 0.7$ are mostly those objects for which the correction is not reliable and thus these objects have larger scatter in the ellipticity measurements. For objects with $\epsilon < 0.7$, most of them should have a reliable correction and therefore the measurements scatter less.

The lower right panel of Fig. 6.11 shows a good correlation between the estimated uncertainty σ_ϵ^w and the real scatter σ_ϵ . However, at about $\sigma_\epsilon^w < 0.25$, σ_ϵ increases again so that these objects get a larger weight than appropriate. In general, the observed scatter in ϵ is smaller than the estimated one. This is expected because the estimated scatter also takes the intrinsic ellipticity distribution of galaxies into account, $(\sigma_\epsilon^w)^2 = (\sigma_\epsilon^{\text{intrinsic}})^2 + (\sigma_\epsilon^{\text{noise}})^2$, which is not the case for the observed scatter.

Unresolved objects have in general, as expected, a larger σ_ϵ than resolved objects which is

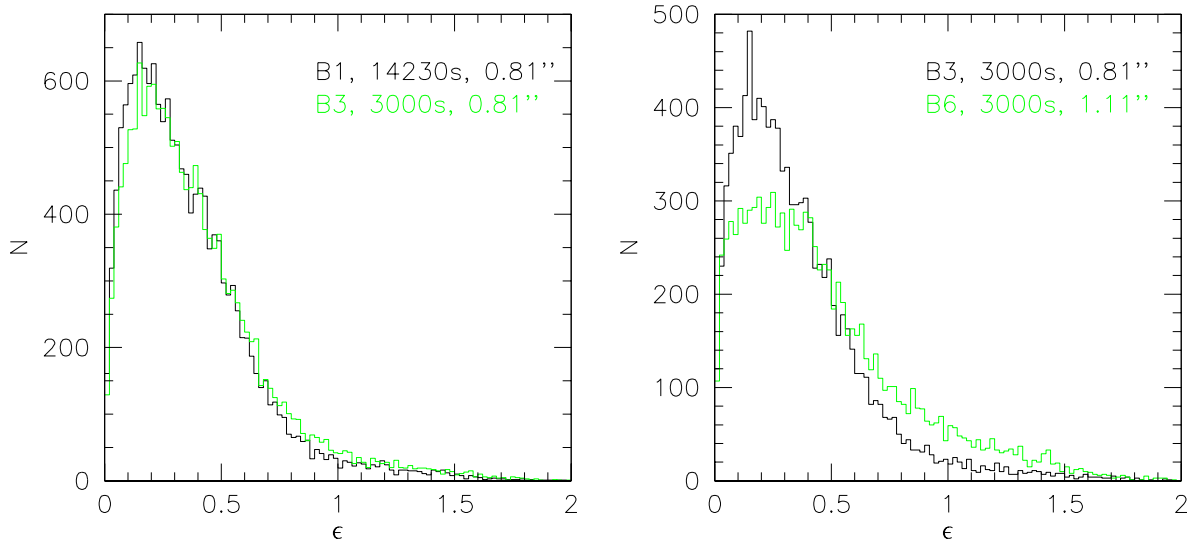


Figure 6.8: Histogram over absolute ellipticities ϵ . The left panel shows histograms for objects identified on B1 and B3. The black line corresponds to the shape measurement on B1 while the green line corresponds to B3. The right panel shows the same for the sumframes B3 (black) and B6 (green).

almost independent of the magnitude and signal-to-noise.

6.3.4 Shape measurements from the deep sumframe

In this Section, we use the objects common to the sumframes B1-B5, B7 from the Section before and compare their shapes to those measured on the deep sumframe. 10971 objects are uniquely identified on the deep sumframe. First, we compare the ellipticities $\langle \epsilon_i \rangle$ averaged from the measurements on the six sumframes to the measurements from the deep sumframe. Figure 6.12 shows that the correlation between these two ellipticity measurements are much tighter than those from the sumframes B1 and B3 or B3 and B6, see Figs. 6.6 and 6.7. However, this is not unexpected because the measurements from the deep sumframe are not independent from those from the sumframes B1-B5, B7. Further, due to the merging of a larger number of catalogs, fewer objects are left for the comparison of the individual sumframes with the deep sumframe than for the comparison of B1 and B3. The objects for which no counterpart was identified are those with the least accurate positions which probably also have the least accurate shape measurements.

Figure 6.12 also shows that a small fraction of objects has systematically larger ellipticities when measured on the deep sumframe instead of the sumframes B1-B5, B7. We cannot fit straight lines to the distributions as we did for the comparison of shape measurements from two sumframes, because we do not have a useful error estimate for the average of

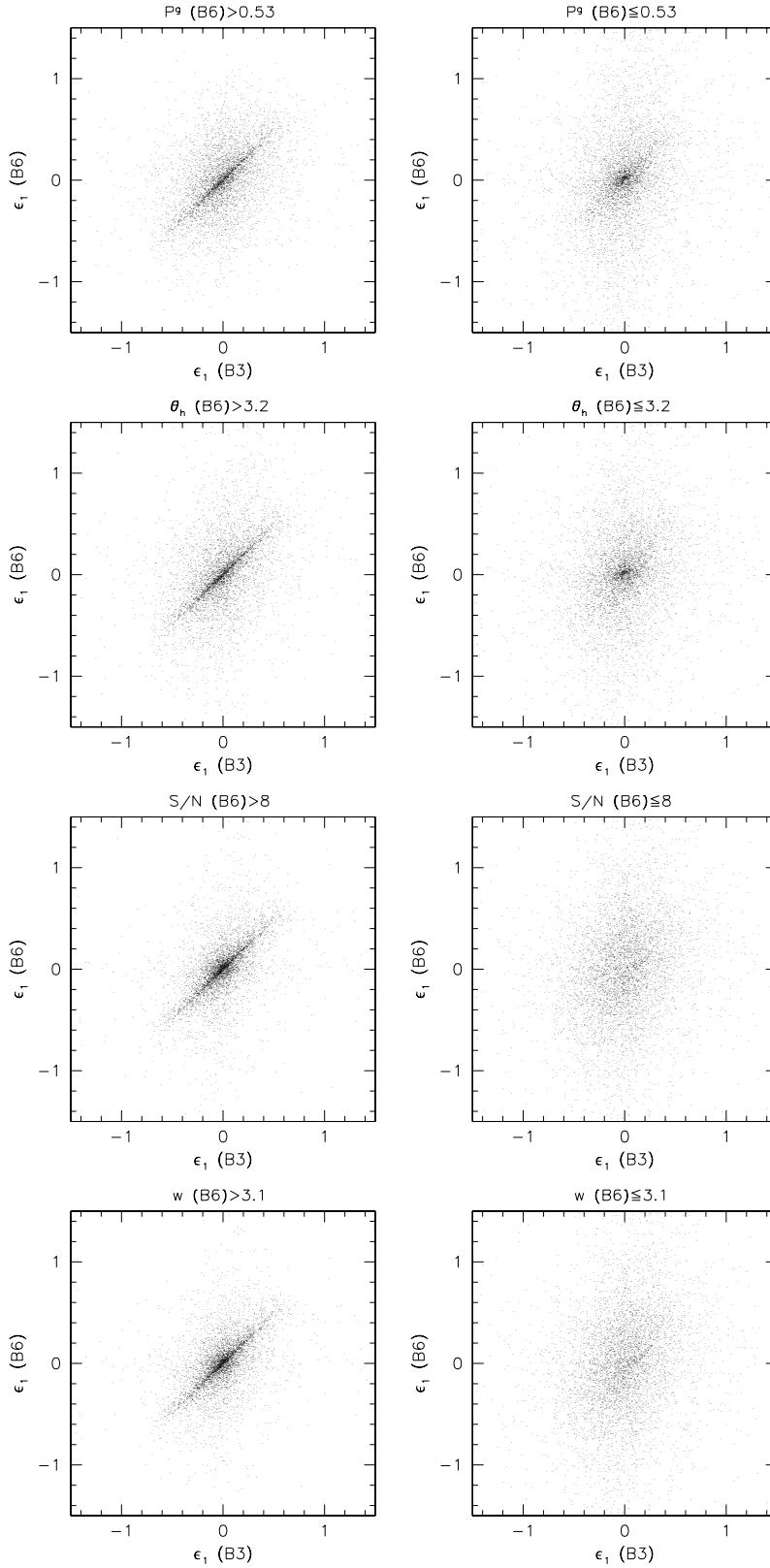


Figure 6.9: Same as Fig. 6.7 but splitting the sample into two subsamples in different ways. Shown is only the relation between $\epsilon_1(B3)$ and $\epsilon_1(B6)$; the plots for the ϵ_2 -component look very similar. The plots in the first row are for a cut in the correction factor P^g , the second row for a cut in half-light radius θ_h , the third row for a cut in signal-to-noise and the last row for a cut in the weights. The left column always shows that subsample for which a more reliable shape measurement is expected.

Table 6.3: Fits to $\epsilon_i(B6) = a\epsilon_i(B3) + b$ for different sets of objects detected on sumframes B3 and B6.

Selection	N	fit to ϵ_1		fit to ϵ_2	
		a	b	a	b
$P^g(B6) > 0.53$	5196	0.972 ± 0.044	0.016 ± 0.008	0.997 ± 0.044	0.005 ± 0.008
$P^g(B6) \leq 0.53$	5205	2.217 ± 0.132	0.037 ± 0.008	1.972 ± 0.113	-0.006 ± 0.008
$\theta_h(B6) > 3.2$	5189	1.222 ± 0.052	0.005 ± 0.009	1.228 ± 0.051	0.005 ± 0.009
$\theta_h(B6) \leq 3.2$	5212	1.663 ± 0.106	0.033 ± 0.007	1.479 ± 0.092	-0.005 ± 0.007
$S/N(B6) > 8$	5186	1.167 ± 0.048	0.029 ± 0.005	1.180 ± 0.048	-0.002 ± 0.005
$S/N(B6) \leq 8$	5215	1.924 ± 0.131	-0.005 ± 0.016	1.677 ± 0.112	-0.003 ± 0.015
$w(B6) > 3.1$	5260	1.164 ± 0.048	0.028 ± 0.005	1.171 ± 0.048	-0.001 ± 0.005
$w(B6) \leq 3.1$	5141	1.850 ± 0.117	-0.002 ± 0.016	1.646 ± 0.101	-0.007 ± 0.015

the shape measurements from the six sumframes available. We tried to use the average of the error estimates from the six sumframes but obtained very different fits when swapping the coordinates, that is when fitting the ellipticities from the deep sumframe as function of the mean ellipticities from the frames B1-B5, B7 instead of doing it the other way around. Therefore, we compare the measurements from the deep sumframe to those from B1, instead. We find that the ellipticities are about 10% larger when measured on the deep sumframe. Because the deep sumframe has larger seeing than sumframe B1, we expected larger ellipticities. However, the difference in seeing is not very large, so that the increase in the ellipticities might appear too large. To test this, we also compared the ellipticities from the deep sumframe to those from B7. B7 has larger seeing than the deep sumframe, so that the ellipticities from B7 should be larger now. We find a slope of almost exactly one for the straight-line-fit (within less than 1%). From that we conclude that the ellipticities measured on the deep sumframe are systematically larger than when measured on a sumframe with shorter exposure time in a way that cannot be accounted for just by the seeing conditions. The reason for this increase has to be investigated in more detail. A hint to a possible answer might already be given in Figure 6.5. There, the PSF patterns appear quite smooth for most of the sumframes B1-B5, B7 while for the deep sumframe a larger number of stars seems to have ellipticities that do not fit to the overall pattern. A few such stars can also be found in e.g. B1 or B5 but hardly in e.g. B2 or B6. Therefore, it is well possible that the anisotropy correction works less well for the deep sumframe than for the other sumframes.

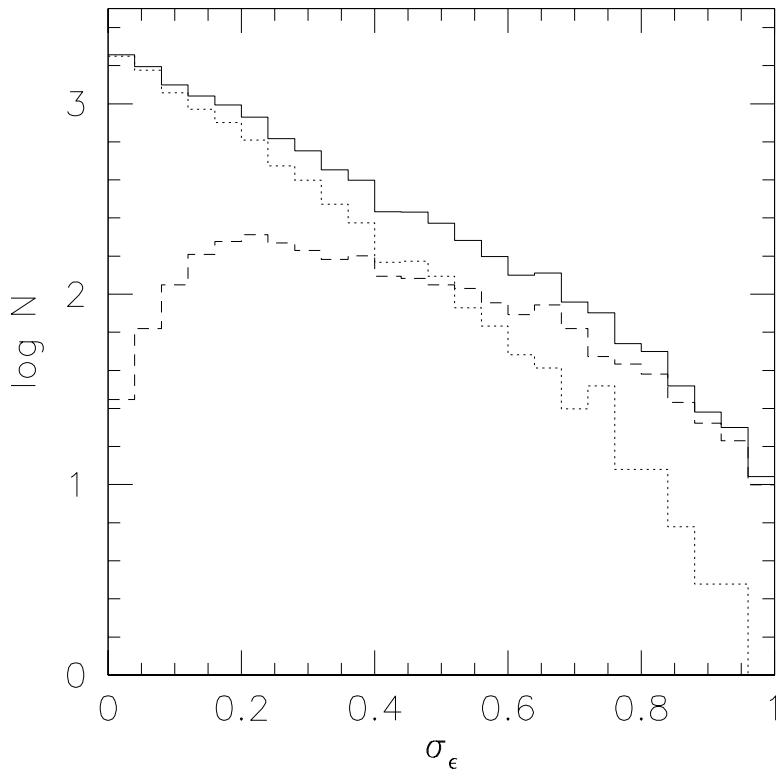


Figure 6.10: Histogram over the standard deviation σ_ϵ between the ellipticities ϵ measured on the sumframes B1-B5 and B7. The solid lines refers to all objects. The dotted and dashed lines show the histogram for objects that are resolved (dotted) and unresolved (dashed) on B7. B7 is the sumframe with the largest seeing in this comparison.

6.3.5 Galaxy-galaxy lensing measured from the different sumframes

For different choices of the weights we measure and compare the galaxy-galaxy lensing measurements from the different sumframes. We only use objects common to the sumframes B1-B5, B7 and the deep sumframe. The galaxy-galaxy lensing measurement is done as described in Sect. 7.1. Here, we take all resolved objects with $18 < R \leq 21.2$ as lenses and those with $21.5 < R \leq 24$ as sources. We always take the positions and magnitudes from the deep sumframe and only use the measurements of the ellipticities and weights from the different sumframes. This assures that always the shear from the same lens-source pairs is measured. Table 6.4 gives our different choices of the weights. W1 corresponds to no weighting at all, W2 uses just the standard deviation σ_ϵ between the ellipticities measured

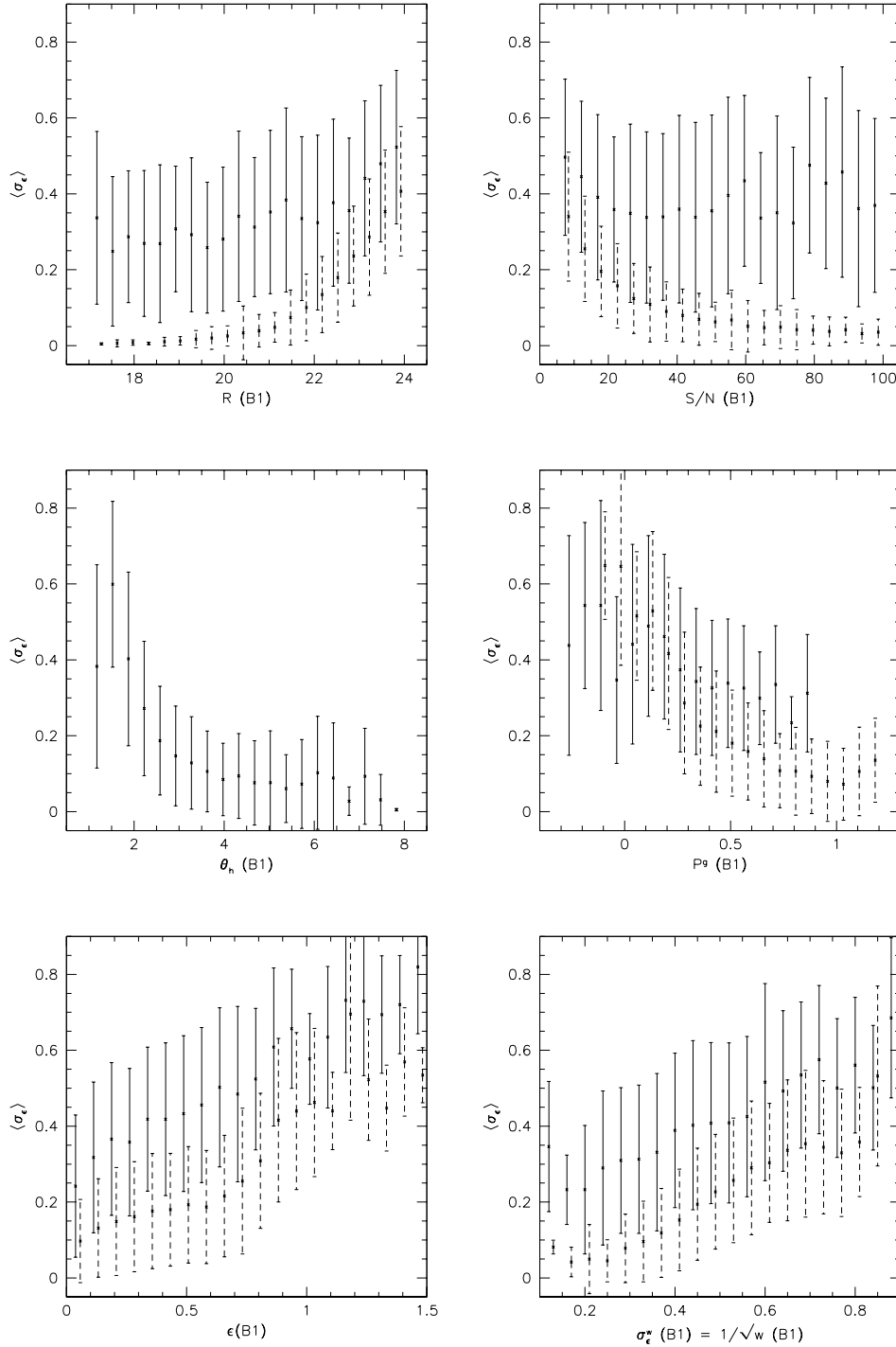


Figure 6.11: Measured standard deviations between shape measurements from the sum-frames B1-B5 and B7. The data are binned as function of magnitude (upper left panel), signal-to-noise (upper right panel), half-light radius (middle left panel), correction factor P^g (middle right panel), absolute ellipticity (lower left panel) and estimated uncertainty in the ellipticities (lower right panel). Shown is for each bin the averaged standard deviation $\langle \sigma_\epsilon \rangle$ of the total ellipticity over all objects in that bin with the standard deviation of σ_ϵ as errorbar. The data points with solid errorbars refer to objects that are unresolved on B7, those with dashed errorbars refer to objects that are resolved on B7. Only for the middle left panel, all objects have been used together. For clarity, the data points of the resolved objects have been shifted slightly to the right.

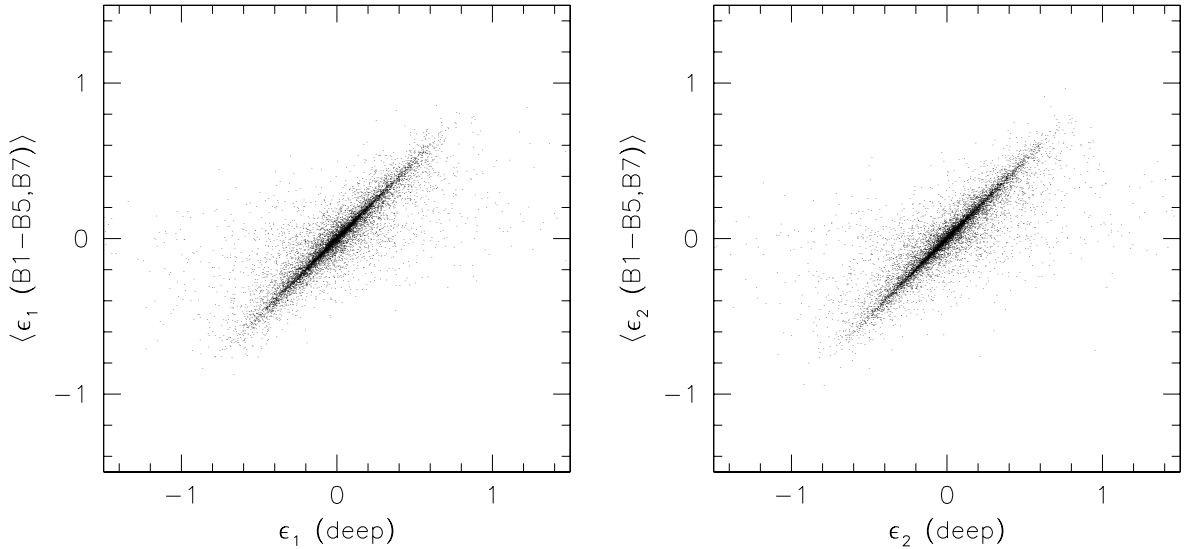


Figure 6.12: Comparison of the recovered ellipticities from the deep sumframe and the mean of the ellipticity measurements from the sumframes B1-B5, B7. The left panel shows the results for the ϵ_1 -component, the right panel for the ϵ_2 -component.

on the six sumframes B1-B5, B7 while W3 uses σ_ϵ as estimate of the measurement error $\sigma_\epsilon^{\text{noise}}$ and adds a constant as estimate of the width of the intrinsic ellipticity distribution. The constant 0.15 corresponds to a width of $\sigma_\epsilon^{\text{intrinsic}} \approx 0.39$. W3 should come closest to an optimal weighting scheme. W4 is just the weight σ_ϵ^w described in Sect. 6.2. Because we found that for objects with about $\sigma_\epsilon^w < 0.25$ the uncertainty in the ellipticities is underestimated, we take for W5 the minimum of σ_ϵ^w and 0.25. Finally, we calculate a new weight W6 in the same way as described in Sect. 6.2 but now choosing neighbouring objects in $P^g - S/N$ space instead of $\theta_h - S/N$ space.

Table 6.4: Different choices of weights of individual objects used for the galaxy-galaxy lensing measurements. Further explanations are given in the text.

W1	$w = 1$
W2	$w = 1/\sigma_\epsilon^2$
W3	$w = 1/(\sigma_\epsilon^2 + 0.15)$
W4	$w = 1/(\sigma_\epsilon^{\theta_h, S/N})^2 = 1/(\sigma_\epsilon^w)^2$
W5	$w = 1/[\min(\sigma_\epsilon^{\theta_h, S/N}, 0.25)]^2$
W6	$w = 1/(\sigma_\epsilon^{P^g, S/N})^2$

Figure 6.13 shows the galaxy-galaxy lensing measurements from the different sumframes

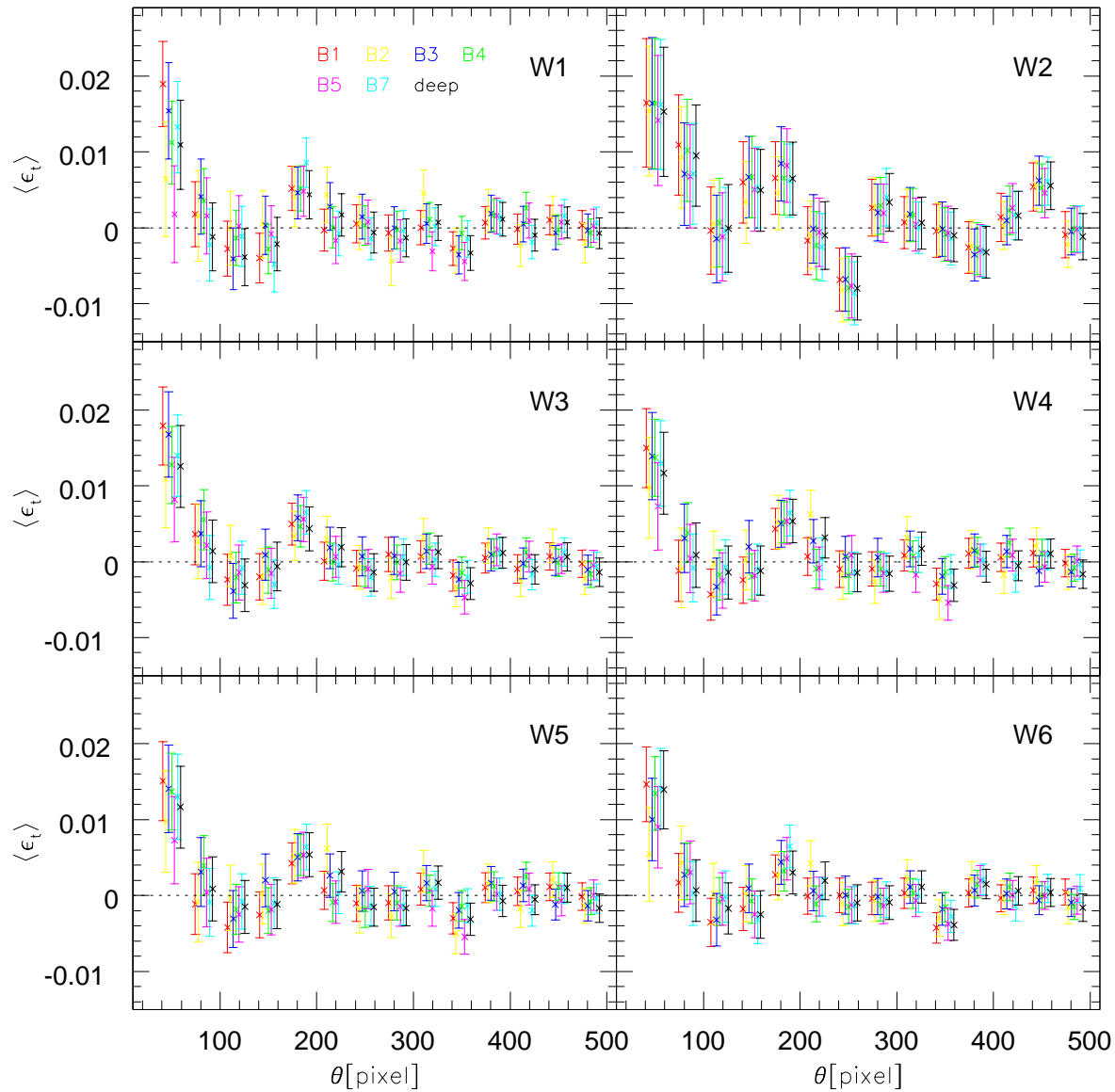


Figure 6.13: Measurement of $\langle \epsilon_t(\theta) \rangle$ for different choices of the weights. Each colour corresponds to a shape measurement from a different sumframe. Further explanations are given in the text. For clarity, the data points corresponding to the sumframes B1-B3 have been shifted slightly to the left and those corresponding to the sumframes B5, B7 and deep to the right.

and for the different choices of weights. The measurement of $\langle \epsilon_t(\theta) \rangle$ shows best agreement but also the largest errorbars for W2. The errorbars are that large because almost circular objects that contain hardly any useful information are treated in the same way as objects with larger ellipticities. For almost circular objects, the scatter in the shape measurement is typically smaller than for elongated ones (see Fig. 6.11) so that these objects get very high weights. The weights W3 are more appropriate because they include the intrinsic ellipticity distribution of the galaxies. For W3, the data points from all sumframes agree with those from the deep sumframe within $1\text{-}\sigma$. However, for normal observations, the knowledge of σ_ϵ is not available and therefore other definitions of the weights like W4 to W6 have to be used. In those cases, the number of data points outside the $1\text{-}\sigma$ limits from the deep sumframe increases.

Because it is hard to judge from Fig. 6.13 the quality of the different weighting schemes and sumframes, we compare in Fig. 6.14 the sizes of the errorbars $\sigma(\langle \epsilon_t \rangle)$ for different weighting schemes (left panel) and different sumframes (right panel). Because the lens-source pairs are the same for all measurements, the sizes of the errorbars directly reflect the quality of the shape measurements and the weighting schemes. The weights W3-W6 all yield smaller errorbars than W1 which corresponds to no weighting. W4 and W5 are very similar and slightly larger than W3. The smallest errorbars are obtained for W6 which gives errorbars that are even smaller than for W3 which we consider as the best-suited weighting scheme. From this Figure we conclude that the weighting scheme W4 that was already introduced in Sect. 6.2 as our standard weighting scheme is able to reduce the errorbars in the lensing measurement in a way which comes close to the optimal weighting scheme. Slight improvements are still possible by changing the parameter space in which neighbouring objects are searched from which the scatter in the ellipticities is measured.

The right panel of Fig. 6.14 shows that the sizes of the errorbars are quite similar for the different sumframes. However, B1 and B4 always give the smallest errorbars while B2 gives systematically larger errorbars than the other frames. The result for B1 and B4 is quite easily understood because B4 is the sumframe with the best seeing while B1 has still good seeing but also a substantially larger exposure time than B4. The large errorbars for B2 cannot be understood from just the seeing or exposure time of this sumframe. A closer look at the PSF correction of B2 revealed that for this sumframe there is not just one stellar sequence in the radius-magnitude diagram (see Fig. 6.2) but two sequences at slightly different half-light radii. The objects forming these two sequences lie in distinct halves of the sumframes meaning that the size of the PSF is not uniform across the field-of-view. However, to a smaller degree this is also true for the other sumframes. Therefore, it is not clear if this effect can really explain the larger errors for the sumframe B2.

Not only the sizes of the errorbars determine if a weighting scheme is appropriate. Agreement between the measurements from the different sumframes is also necessary. We quantify this agreement by calculating for each weighting scheme and for each bin k shown in Fig. 6.13 the weighted mean

$$\overline{\langle \epsilon_t(\theta_k) \rangle} = \frac{\sum_i (\langle \epsilon_{t,i}(\theta_k) \rangle / \sigma_i^2)}{\sum_i (1/\sigma_i^2)} \quad (6.10)$$

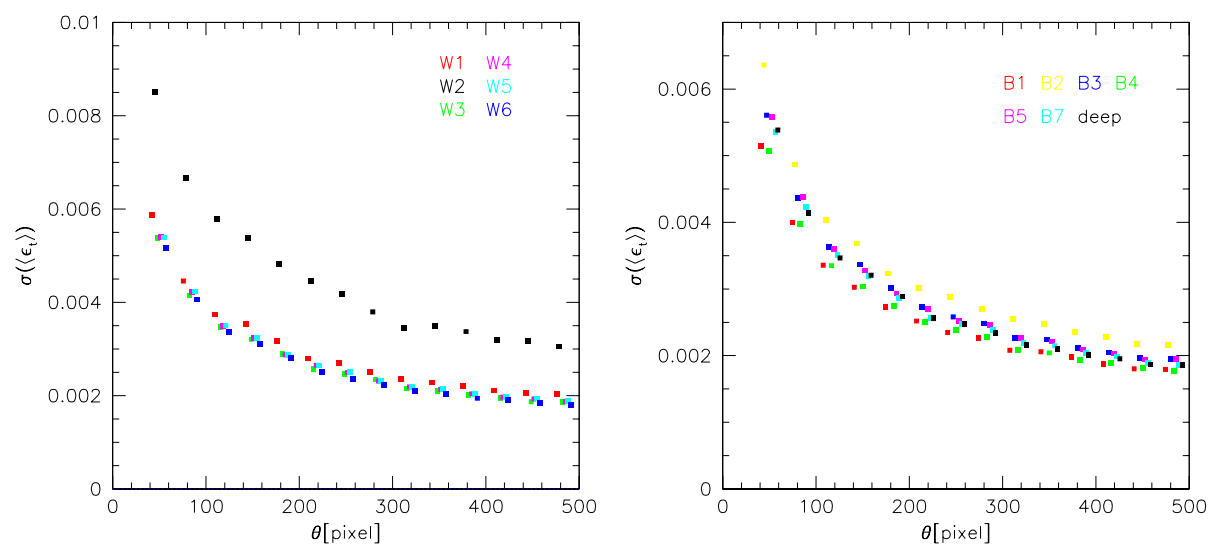


Figure 6.14: Sizes of the errorbars of the measurement of $\langle \epsilon_t(\theta) \rangle$ in Fig. 6.13. Shown in the left panel are just the errorbars for the measurements from the deep sumframe for the different choices of weights. The right panel gives the errorbars for the weighting scheme W3 for the different sumframes. For clarity, the data points have been shifted slightly towards the left or right.

and the χ^2

$$\chi_k^2 = \sum_i \left(\frac{\langle \epsilon_{t,i}(\theta_k) \rangle - \overline{\langle \epsilon_t(\theta_k) \rangle}}{\sigma_i^2} \right)^2 \quad (6.11)$$

of the measurements from the seven sumframes. The sums in Eqs. (6.10) and (6.11) extend over the sumframes B1-B5, B7, deep. σ_i is here the size of the errorbar of the corresponding data point. We first tried to compare χ_k^2 from the different weighting schemes for each bin k individually. However, apart from W2 that always gives very small χ_k^2 , there is no systematic trend visible such that a certain weighting scheme always gives the smallest or largest χ_k^2 . Therefore, we consider for each weighting scheme the sum of the χ_k^2 's from the 14 bins, $\chi^2 = \sum_k \chi_k^2$. We find $\chi^2 = 26.56$ for W1, $\chi^2 = 3.22$ for W2, $\chi^2 = 16.81$ for W3, $\chi^2 = 24.16$ for W4, $\chi^2 = 24.15$ for W5, and $\chi^2 = 17.35$ for W6. In this comparison, our standard weighting scheme W4 is only slightly better than no weighting (W1) while W6 is almost as good as W3.

Finally, we compare fits of $\langle \epsilon_t(\theta) \rangle = a/\theta$ to the galaxy-galaxy lensing measurements, see Table 6.5, where the fits extend over $\theta = (35 - 500)$ pixel. For more details on how the fits are made see Section 7.1. The uncertainties in the fits directly reflect the sizes of the errorbars for different weighting schemes or different sumframes, for example they are smallest for the sumframes B1 and B4 which already yielded the smallest errorbars on the measurement of $\langle \epsilon_t(\theta) \rangle$. For the weighting schemes that we consider as appropriate, W3-W6, the measurements using different weights agree quite well, typically within $1-\sigma$. The measurements using different sumframes agree best for the weighting scheme W6. For W4 and W5 the amplitudes of the fits deviate stronger. However, one has to keep in mind that some of the sumframes should normally not be used for lensing studies due to either the short exposure time or the seeing conditions.

6.3.6 Summary

We compared shape measurements and galaxy-galaxy lensing measurements from independent sumframes. We find that the shape measurement is most sensitive to the seeing conditions and that larger seeing systematically increases the measured ellipticities for some fraction of detected objects. The exposure time of a sumframe, on the other hand, has only little influence on the shape measurement. Of course, deep exposures are still preferable because they give more objects for which shapes can be measured and that can be used for lensing studies. The uncertainty in the shapes that we estimated from the scatter between the measurements from the independent sumframes is a function of e.g. the half-light radius, signal-to-noise or ellipticity of the objects. We find the strongest dependence on signal-to-noise, magnitude and P^g , the correction factor from the KSB algorithm. However, the exact dependence on the magnitude will depend on the depth of the exposure. Because it is closely related to the signal-to-noise, the signal-to-noise of an object appears more appropriate and more generally usable for deriving weights. Comparing the galaxy-galaxy lensing measurements with different weighting schemes we find that a weighting scheme using the signal-to-noise and the correction factor P^g of an object

Table 6.5: Fits of $\langle \epsilon_t(\theta) \rangle = a/\theta$ over (35 – 500) pixel for the different sumframes and weighting schemes used, see also Fig. 6.13.

Frame	W1	W2	W3	W4	W5	W6
B1	0.163 ± 0.141	0.493 ± 0.210	0.221 ± 0.129	0.088 ± 0.132	0.091 ± 0.133	0.102 ± 0.123
B2	0.168 ± 0.189	0.358 ± 0.205	0.172 ± 0.158	0.174 ± 0.169	0.174 ± 0.169	0.204 ± 0.153
B3	0.310 ± 0.161	0.462 ± 0.212	0.321 ± 0.142	0.335 ± 0.147	0.340 ± 0.147	0.175 ± 0.137
B4	0.220 ± 0.143	0.477 ± 0.207	0.229 ± 0.130	0.223 ± 0.133	0.225 ± 0.133	0.176 ± 0.127
B5	-0.041 ± 0.162	0.401 ± 0.214	0.050 ± 0.144	-0.036 ± 0.148	-0.036 ± 0.148	0.072 ± 0.139
B7	0.105 ± 0.156	0.404 ± 0.208	0.124 ± 0.138	0.160 ± 0.146	0.159 ± 0.146	0.164 ± 0.138
deep	0.026 ± 0.151	0.430 ± 0.208	0.124 ± 0.139	0.139 ± 0.142	0.138 ± 0.142	0.124 ± 0.131

works best. The weighting scheme introduced by Erben et al. (2001) also improves the measurements as compared to no weighting. Finally, we find that not all of our sumframes are suitable for lensing measurements. For the sumframe B5 with comparably small exposure time and seeing around $1''$ we obtain a systematically small lensing signal. This raises the question of how one can judge if a sumframe is suitable for lensing studies or not.

Chapter 7

Galaxy-galaxy lensing measurements from COMBO-17

This Chapter contains the main results of this thesis which are the galaxy-galaxy lensing measurements for two of the COMBO-17 fields. First, in Sect. 7.1 we report on the detection of a galaxy-galaxy lensing signal without yet using the redshift information from COMBO-17. Then, in Sect. 7.2 we carry out the quantitative measurement using redshifts and spectral classification. We apply the lens models described in Sects. 2.5 and 3.3 to the data.

7.1 Detection of a galaxy-galaxy lensing signal

In this Section we try to detect a galaxy-galaxy lensing signal by measuring the average tangential alignment of background galaxies with respect to foreground galaxies as a function of projected separation, see Sect. 3.4.2. In this step we do not use redshifts yet, but apply simple magnitude cuts for the lens and source selection. Therefore, we can use the shape catalogs that were obtained directly from the sumframes described in Sect. 6.1 without being restricted to objects that are common to these catalogs and those from COMBO-17. The catalogs from COMBO-17 are used only for the determination of the photometric zeropoints. In addition to the four COMBO-17 fields we also use the fifth field here to which we refer as FDF field, see also Sect. 5.1. Table 7.1 gives an overview of the exposure times and seeing conditions of the five fields.

To determine the photometric zeropoints, we use bright but unsaturated stellar objects with $17.5 < R < 20$ which are common to the shape catalogs and the COMBO-17 catalogs. This is possible only for the three fields for which data reduction and calibration has already been finished by COMBO-17. For the A901 and the S11 fields we find the same zeropoints within 0.01 mag while for the CDFS field the zeropoint is shifted by 0.25 mag relative to the two former ones. For simplicity, we decided to use the zeropoint from the A901 and S11 fields for all five fields. Note that, as long as we use the magnitudes only for a rough distinction of lens and source galaxies but do not use it to interpret the resulting

Table 7.1: Observational characteristics of the five fields. $\theta_{h,\min}$ denotes the minimum half-light radius required for potential lens and source galaxies. It is the maximum half-light radius at which an object is still regarded as unresolved and used for the PSF correction, see also Fig. 6.2.

Field	Exposure (s)	PSF (")	$\theta_{h,\min}$ (")
A901	24900	0.74	0.88
S11	21600	0.88	1.02
CDFS	57140	0.88	1.02
SGP	27100	0.88	1.02
FDF	15340	0.88	1.02

lensing signal and try to relate it to the lens galaxy population, this somewhat uncertain photometric calibration is of no strong concern. However, when trying to compare the lensing signals from the different fields, the photometric calibration certainly plays a role because a wrong calibration would mean that we compare different lens galaxy populations for which a different lensing signal would be expected.

Apart from the magnitude cuts we select only objects with half-light radii above the PSF as lens and source galaxies. Further, we exclude objects with close projected neighbours as potential sources. This exclusion is necessary because close neighbours affect the shape measurements and could thus bias the galaxy-galaxy lensing measurement. For simplicity, we take only those objects as potential neighbours that are read in from the object catalogs used and that have magnitudes $R_{d,\min} < R \leq R_{s,\max}$ where $R_{d,\min}$ is the brightest magnitude for lenses and $R_{s,\max}$ is the faintest magnitude for sources. This makes it well possible to miss bright neighbours. However, $R_{d,\min}$ is chosen close to the saturation limit, and we will see below that not much bias is expected if a few bright neighbours are missed. It is not clear a priori what the minimum allowed separation $\theta_{\text{neighbour}}$ should be. If it is too small, we include too many sources with unreliable shape measurements while, if it is too large, we exclude too many sources and thus deteriorate our signal-to-noise. We experimented with different values of $\theta_{\text{neighbour}}$. Figure 7.1 shows plots for lenses with $R = 18 - 22$ and sources with $R = 22.5 - 24$. We will show further below how these plots were obtained. Here, we only use them to explain our choice of $\theta_{\text{neighbour}}$. These plots are remarkably similar. The only clear difference is seen for the innermost data point which has a negative $\langle \epsilon_t \rangle$ in all cases and lies outside the plotted range for all but the plot with $\theta_{\text{neighbour}} = 20$ pixel. This negative data point clearly indicates that the ellipticities of objects with close neighbours are biased such that these objects are preferentially radially aligned with their next neighbour. Therefore, it is important to exclude these close pairs from the further analysis. However, the similarity of the data points at larger θ indicates that no bias is introduced if these objects are kept and used in pairs with larger separations. We use fine bins of 1 pixel width to fit a $1/\theta$ profile to the data points in Fig. 7.1, see Table 7.2. These fits show that pairs with separations smaller than $\theta_{p,\min} = 35$ pixel should be

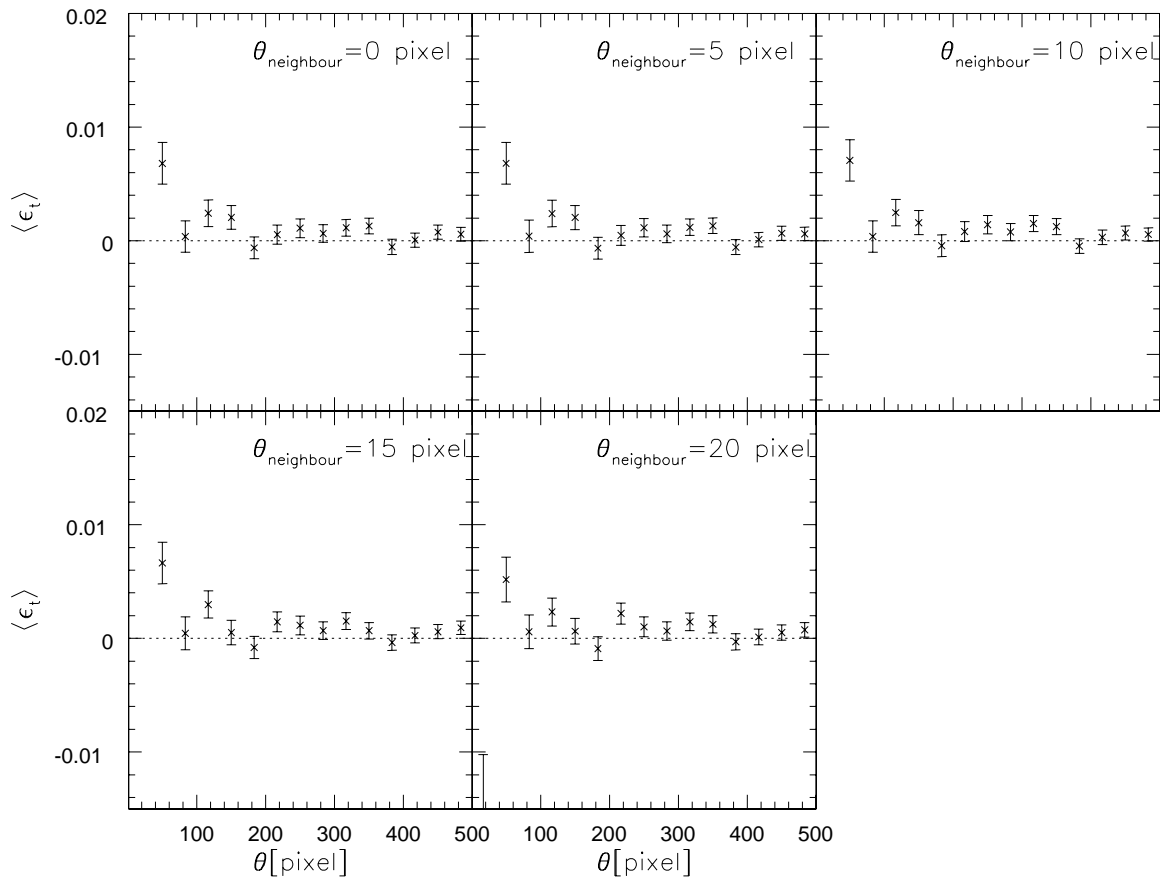


Figure 7.1: Averaged tangential ellipticities as function of projected distance for all five fields together. For each plot, galaxies with $18 < R < 22$ are taken as lenses and galaxies with $22.5 < R < 24$ as sources. Source galaxies with a projected neighbour within $\theta_{\text{neighbour}}$ are excluded. The corresponding values of $\theta_{\text{neighbour}}$ are given inside the plots.

excluded because, for all values of $\theta_{\text{neighbour}}$, the fits extending over (35 – 500) pixel give the smallest relative errors. Further, the amplitude of the signal is smaller if pairs with smaller $\theta_{\text{p,min}}$ are also used, but we find that it is stable if at least pairs with distances smaller than 35 pixel are excluded. Fits extending over (40 – 500) pixel or (45 – 500) pixel give the same amplitude as those extending over (35 – 500) pixel, but a larger relative error. Comparing the fits extending over (35 – 500) pixel for different choices of $\theta_{\text{neighbour}}$ shows that the best signal is obtained when potential sources with neighbours within 10 pixel are excluded. However, note that the results are not very sensitive to the actual choice of $\theta_{\text{neighbour}}$. The amplitude of the signal is consistent for all given choices of $\theta_{\text{neighbour}}$; it is more sensitive to $\theta_{\text{p,min}}$. From this we conclude that objects with neighbours within 10 pixel have too biased shape measurements. Objects for which the closest neighbour lies

within (10–35) pixel are also biased against the closest neighbour so that such pairs should be excluded. However, these sources still contain enough information when combined with lenses at larger separations than 35 pixel to improve the statistics and should thus be kept as potential sources.

As expected from the different seeing conditions, we find slightly different best choices of $\theta_{\text{neighbour}}$ and θ_{min} for the five fields individually. However, because the differences are not large, we will use $\theta_{\text{neighbour}} = 10$ pixel and $\theta_{\text{min}} = 35$ pixel for all fields.

Table 7.2: Fits of $\langle \epsilon_t(\theta) \rangle = a/\theta$ for all five fields together. The first column gives the minimum allowed projected distance to the next neighbour of a potential source galaxy. The second to fourth columns give the fitted values of a with its standard errors. The index to a indicates over which range in θ in pixel the fit extends. N_s gives the number of sources and the last column shows what fraction of sources is lost for the different choices of $\theta_{\text{neighbour}}$ relative to $\theta_{\text{neighbour}} = 0$ pixel.

$\theta_{\text{neighbour}}$ [pixel]	a_{35-500}	a_{20-500}	a_{10-500}	N_s	loss [%]
0	0.2074 ± 0.0452	0.1295 ± 0.0434	-0.0636 ± 0.0557	57697	-
5	0.1861 ± 0.0462	0.1088 ± 0.0445	-0.0813 ± 0.0557	57629	0.1
10	0.2234 ± 0.0459	0.1478 ± 0.0441	-0.0548 ± 0.0566	56436	2.2
15	0.2051 ± 0.0470	0.1231 ± 0.0453	0.0273 ± 0.0493	52286	9.4
20	0.1855 ± 0.0507	0.1166 ± 0.0485	0.1166 ± 0.0485	45893	20.5

7.1.1 Measurement of $\langle \epsilon_t(\theta) \rangle$

As input to our programs we use filtered object catalogs in which objects with half-light radii smaller than the size of the PSF, $\theta_h \leq \theta_{h,\text{min}}$, are excluded. Only those objects with $R_{d,\text{min}} < R \leq R_{s,\text{max}}$ are read in. First, objects with neighbours within a given $\theta_{\text{neighbour}}$ are determined and marked. Each object is then checked for being a potential source galaxy. If it is not marked as object with close neighbour and fulfills the magnitude cut $R_{s,\text{min}} < R \leq R_{s,\text{max}}$ for sources, it is taken as source galaxy j . The object list is then searched for potential lenses which are objects within a certain maximum distance θ_{max} relative to the source j and with $R_{d,\text{min}} < R \leq R_{d,\text{max}}$. For an identified lens i , the tangential ellipticity $\epsilon_{t,ij}$ for this special lens-source pair is calculated according to Eq. (3.50). From the projected separation θ between lens and source, the corresponding bin k in θ is determined. At this step we use bins of just 1 pixel width which can later be rearranged to arbitrary bin sizes. These fine bins allow us to fit the profile $\epsilon_t(\theta)$ much more accurately than fewer but larger bins would do. For each bin k , the weighted averaged tangential ellipticity $\langle \epsilon_{t,k} \rangle = (\sum w_j \epsilon_{t,ij}) / \sum w_j$ is calculated, where the sum extends over all N pairs belonging to that bin and w_j is the weight assigned to the source galaxy j from the shape measurement, see Sect. 6.2. We did not try the weighting scheme W6 from Sect.

6.3.5 yet. The errorbars to $\langle \epsilon_{t,k} \rangle$ are determined from randomizing the orientations of the source galaxies 100 times. For each randomization the corresponding $\langle \epsilon_{t,k,\text{rand}} \rangle$ is measured in exactly the same way as described above. The standard deviation of these simulated $\langle \epsilon_{t,k,\text{rand}} \rangle$ is assigned as errorbar to the measured $\langle \epsilon_{t,k} \rangle$.

Figure 7.2 shows $\langle \epsilon_t(\theta) \rangle$ for the different fields for lenses with $18 < R_d < 22$ and sources with $22.5 < R_s < 24$. $\theta_{\text{neighbour}} = 10$ pixel is used. Table 7.3 shows fits to $\langle \epsilon_t(\theta) \rangle = a/\theta$. A galaxy-galaxy lensing signal is detected in all fields but the CDFS field. However, the detection for the S11 field is only marginal. The remaining three fields (A901, SGP and FDF) have consistent amplitudes in the fits. These differences between the five fields show that even a field size of about $30' \times 30'$ might not yet be large enough to be unaffected by cosmic variance. The differences cannot be explained by different seeing conditions or depth of the fields. While it is true that the CDFS field is substantially deeper than the other fields, this cannot explain the differences in the galaxy-galaxy lensing measurement. The weighted averaged tangential alignment $\langle \epsilon_{t,k} \rangle$ measured from a sumframe of the same field with shorter exposure time yields results consistent with those from the deep sumframe. Also, no signal is detected if we change the magnitudes of the objects in the CDFS field by 0.25 mag which is the more appropriate calibration. It has to be investigated if the differences between the fields are due to differences in e.g. the redshift distributions of the galaxies, their clustering properties or the galaxy populations themselves.

Table 7.3: Fits of $\langle \epsilon_t(\theta) \rangle = a/\theta$ over (35 – 500) pixel for the five fields individually and combined. The second column gives the fitted values of a with its standard errors. N_d , N_s and N_p give the numbers of lenses, sources and pairs. Sources with a neighbour within 10 pixel have been excluded.

Field	a	N_d	N_s	N_p
A901	0.26 ± 0.09	4719	11748	546023
S11	0.17 ± 0.11	4465	10588	437785
CDFS	-0.02 ± 0.11	5571	12661	572150
SGP	0.37 ± 0.10	4343	11448	441677
FDF	0.30 ± 0.12	4007	9991	383922
all	0.22 ± 0.05	23105	56436	2381557

7.1.2 Tests of the galaxy-galaxy lensing signal

We perform a number of null tests to check if the detected signal can really be assigned to galaxy-galaxy lensing. All these tests are designed to give signals consistent with zero.

First, we rotate the sources by 45° before doing the measurement. The ellipticity component we measure this way is also referred to as *cross component* ϵ_\times . It is given by $\epsilon_\times = -[\epsilon_2 \cos(2\alpha) - \epsilon_1 \sin(2\alpha)]$ where α is defined as for the tangential ellipticity, see Eq. (3.50). Figure 7.3 shows $\langle \epsilon_\times(\theta) \rangle$ measured in exactly the same way as $\langle \epsilon_t(\theta) \rangle$ in Fig. 7.2.

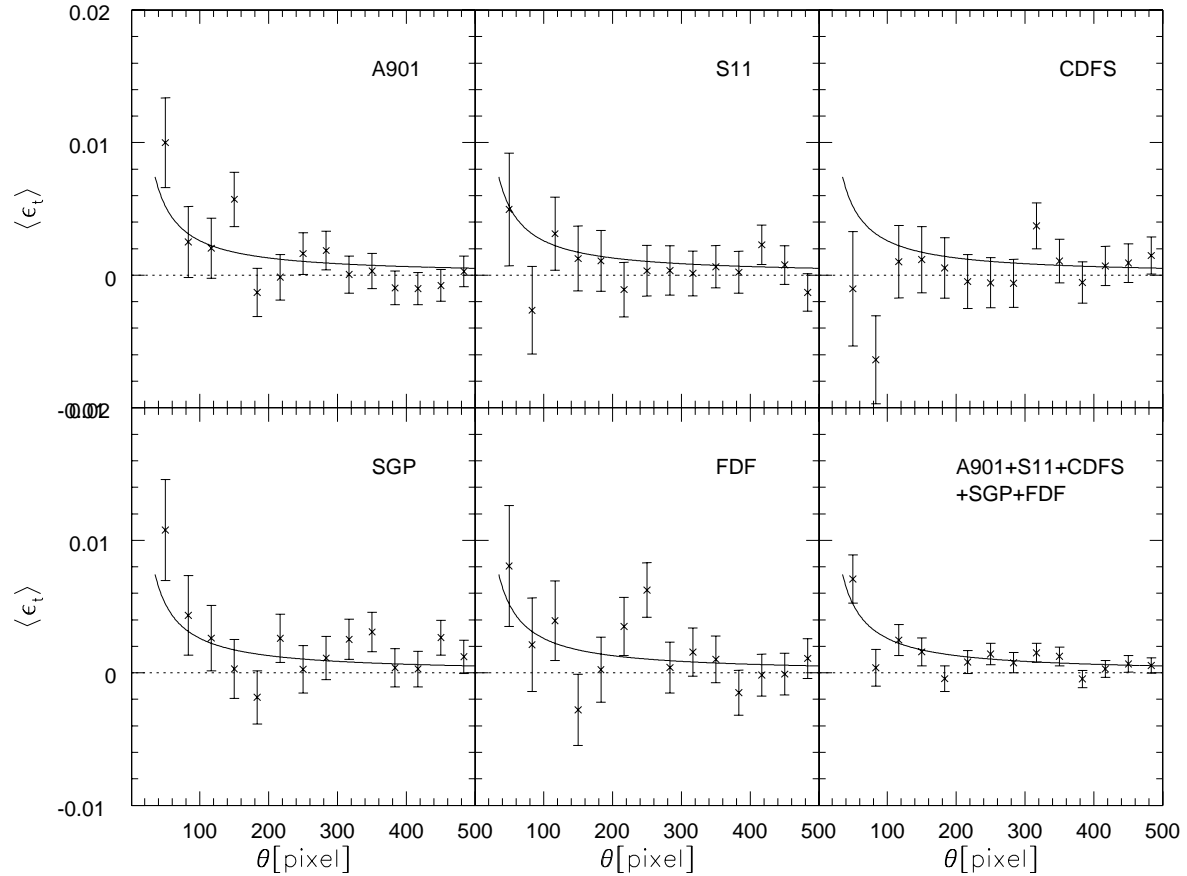


Figure 7.2: Averaged tangential ellipticities as function of projected distance for all five fields individually and combined. For each plot, resolved objects with $18 < R < 22$ are taken as lenses and those with $22.5 < R < 24$ as sources. Sources with a projected neighbour within $\theta_{\text{neighbour}} = 10$ pixel are excluded. The solid lines show fits to $\langle \epsilon_t(\theta) \rangle = a/\theta$ over (35 – 500) pixel, see Table 7.3.

Table 7.4 shows fits to $\langle \epsilon_{\times}(\theta) \rangle = a/\theta$. In the next test we use the randomizations of the orientations of the source galaxies that were already used to derive the errorbars on the galaxy-galaxy lensing signal. We measure ϵ_t from the randomly oriented sources and average $\langle \epsilon_{t,k} \rangle$ for each bin k over the 100 different realizations. The results are given in the third column of Table 7.4. The fourth column of the Table shows the results for randomizing the positions of the lens galaxies 100 times. In this test, ϵ_t is measured with respect to the random positions of the lens. $\langle \epsilon_{t,k} \rangle$ for each bin k is averaged over the different realizations and the standard deviation of these 100 measurements of $\langle \epsilon_{t,k} \rangle$ is taken as error bar. The last test is to swap lenses and sources and thus to measure the alignment of the lens galaxies with the sources, see the last column of Table 7.4. In practice, we select lens galaxies with $22.5 < R_d < 24$ and sources with $18 < R_s < 22.5$ that do not have a neighbour within 10 pixel. All these tests give signals consistent with zero. Only in one case, using random lens positions for the SGP field, a $2\text{-}\sigma$ signal is detected. Once the SGP field is used for a quantitative analysis, this should be investigated further.

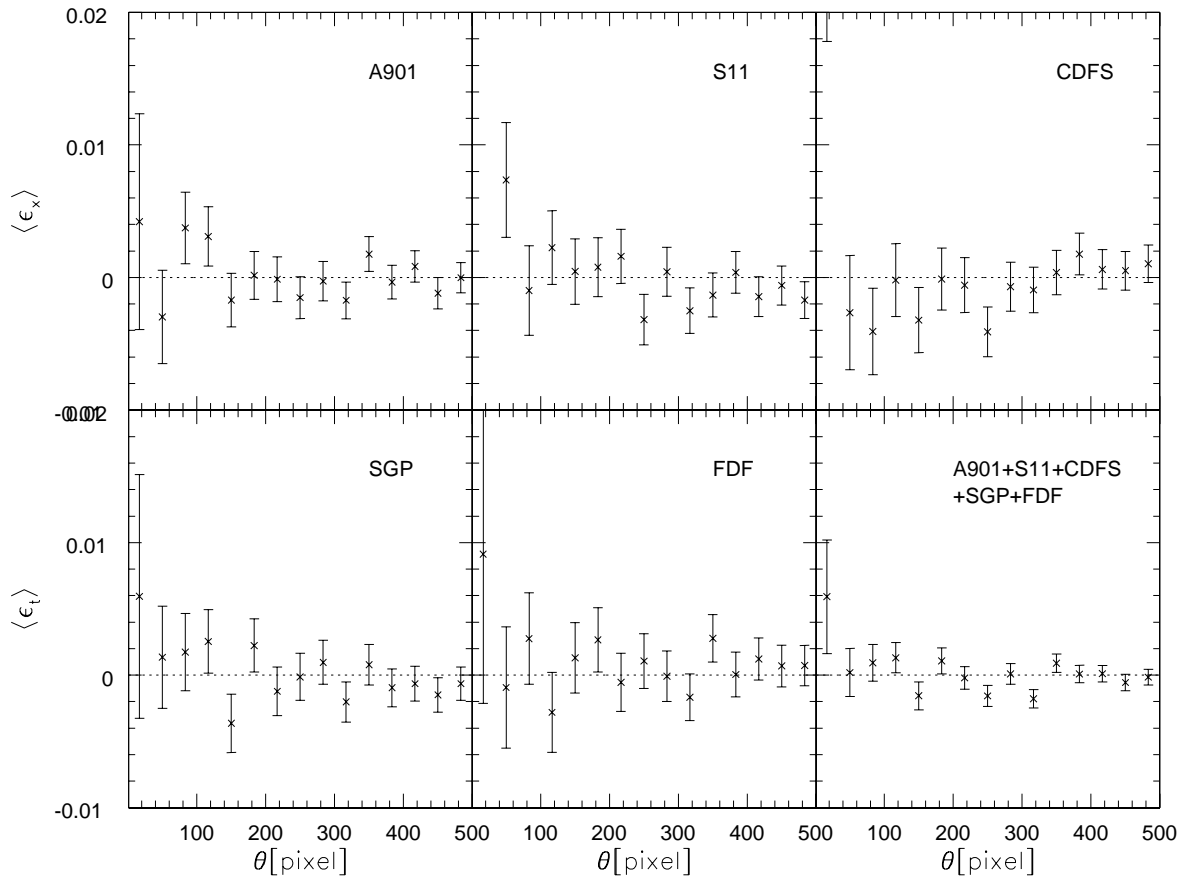


Figure 7.3: Same as Fig. 7.2 but showing $\langle \epsilon_{\times}(\theta) \rangle$ instead of $\langle \epsilon_t(\theta) \rangle$.

Table 7.4: Fits to an a/θ profile for different tests of the galaxy-galaxy lensing signal. Just as for the galaxy-galaxy lensing signal itself, the fits extend over (35 – 500) pixel. The second column shows the results for the cross component ϵ_{\times} . For the third column, the orientations of the source galaxies have been randomized while the positions of the lenses have been randomized for the fourth column. For the last column, source and lens galaxies have been swapped.

Field	$\langle\epsilon_{\times}(\theta)\rangle$	random orientations of sources	random positions of lenses	lenses \leftrightarrow sources
A901	0.02 ± 0.09	0.007 ± 0.009	0.003 ± 0.012	0.06 ± 0.07
S11	0.01 ± 0.11	-0.013 ± 0.011	0.001 ± 0.014	0.05 ± 0.08
CDFS	-0.13 ± 0.11	-0.001 ± 0.011	0.013 ± 0.016	0.01 ± 0.07
SGP	-0.02 ± 0.10	0.004 ± 0.010	-0.027 ± 0.013	0.02 ± 0.08
FDF	0.07 ± 0.12	0.015 ± 0.011	-0.003 ± 0.015	-0.06 ± 0.08
all	-0.02 ± 0.05	0.007 ± 0.005	-0.001 ± 0.006	0.01 ± 0.03

7.2 Quantitative measurements of galaxy-galaxy lensing

In this Section we will use the method by Schneider and Rix (1997) (see Sect. 3.4.2) to derive quantitative results on the dark matter halos of galaxies. We will restrict the analysis to the A901 and S11 fields for which we have redshifts and spectral classification available and for which a lensing signal has been detected (see Sect. 7.1).

7.2.1 Combined object catalogs from COMBO-17 and shape catalogs

The input catalogs for our quantitative measurement of galaxy-galaxy lensing are merged from the shape catalogs and the COMBO-17 catalogs. We use only objects that have a uniquely identified counterpart. Next, we remove all objects that are not classified as galaxies or likely galaxies by COMBO-17, that is we only take objects with classes 5 or 6 according to the definition of object classes in Sect. 5.3.2. We do not exclude unresolved objects at this step because having the classification available we can also include unresolved objects that are classified as galaxies as potential lenses. We will use positions, ellipticities and half-light radii from the shape catalogs and magnitudes, redshifts, SED-types and luminosities from the COMBO-17 catalogs. The luminosities are derived from restframe SDSS r' -magnitudes which were obtained from the best-fitting template adopting the standard cosmological parameters $(\Omega_m, \Omega_{\Lambda}) = (0.3, 0.7)$. All luminosities are expressed in solar units. For the conversion from absolute magnitudes to luminosities we use $M_{\odot, r'} = 4.47$. Further, we assume a characteristic luminosity $L_{\star, r'} = 10^{10} L_{\odot, r'}$. The corresponding absolute magnitude is $M_{\star, r} = -20.53$.

We will restrict the lens galaxy sample to galaxies with $18 < R_d \leq 24$ and $0.2 < z_d \leq 0.7$, and the source galaxies to $18 < R_s \leq 24$ and $0.3 < z_s \leq 1.55$ with $z_s > z_d + 0.1$. Figure 7.4 gives an overview of the redshift distribution of lens and source galaxies and of the SED distribution of the lenses. In Fig. 7.5 we show the redshift errors assigned by COMBO-17 as function of magnitude and redshift. Figure 7.6 shows the distribution of luminosities. The imposed minimum redshift separation of $\Delta z = 0.1$, which is larger than the assigned redshift error for most of the lens galaxies and the low-redshift sources, should largely exclude false lens-source pairs where the source candidate is actually in front of the lens candidate or is associated with it.

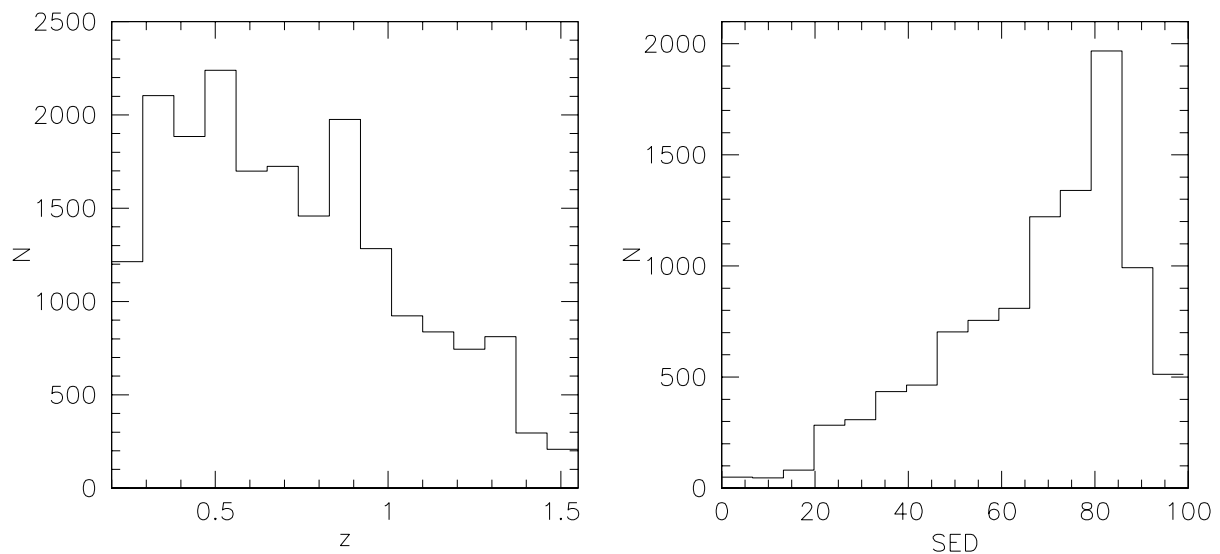


Figure 7.4: Left panel: Histogram over redshift for all galaxies with $18 < R \leq 24$; these are 10110 galaxies from the A901 field and 9291 galaxies from the S11 field. Right panel: Histogram over SED-type for all galaxies with $18 < R \leq 24$ and $0.2 < z \leq 0.7$; these are 4867 galaxies from the A901 field and 5117 galaxies from the S11 field.

For each galaxy i we assign a specific width $\sigma_{\epsilon,i}$ of the intrinsic ellipticity distribution, see Sect. 3.4.2. This $\sigma_{\epsilon,i}$ is given by $\sigma_{\epsilon,i} = 1/\sqrt{w_i}$ where the weights w_i are determined as explained in Sect. 6.2 from all galaxies but leaving out stars and quasars. $\sigma_{\epsilon,i}$ thus is the standard deviation of the ellipticity of 20 galaxies with half-light radii and signal-to-noise similar to that of galaxy i . This approach differs from the more common one of fitting an ellipticity distribution to all galaxies together. However, we find that the average ellipticity of galaxies varies systematically with e.g. half-light radius or signal-to-noise. This difference does probably not reflect any intrinsic difference in the galaxy population but merely reflects the measurement errors. Therefore, our approach allows us directly to take uncertainties in the shape measurements into account. Figure 7.7 shows σ_{ϵ} as function of half-light radius and signal-to-noise. Figure 7.8 shows a histogram over σ_{ϵ} . Note that the

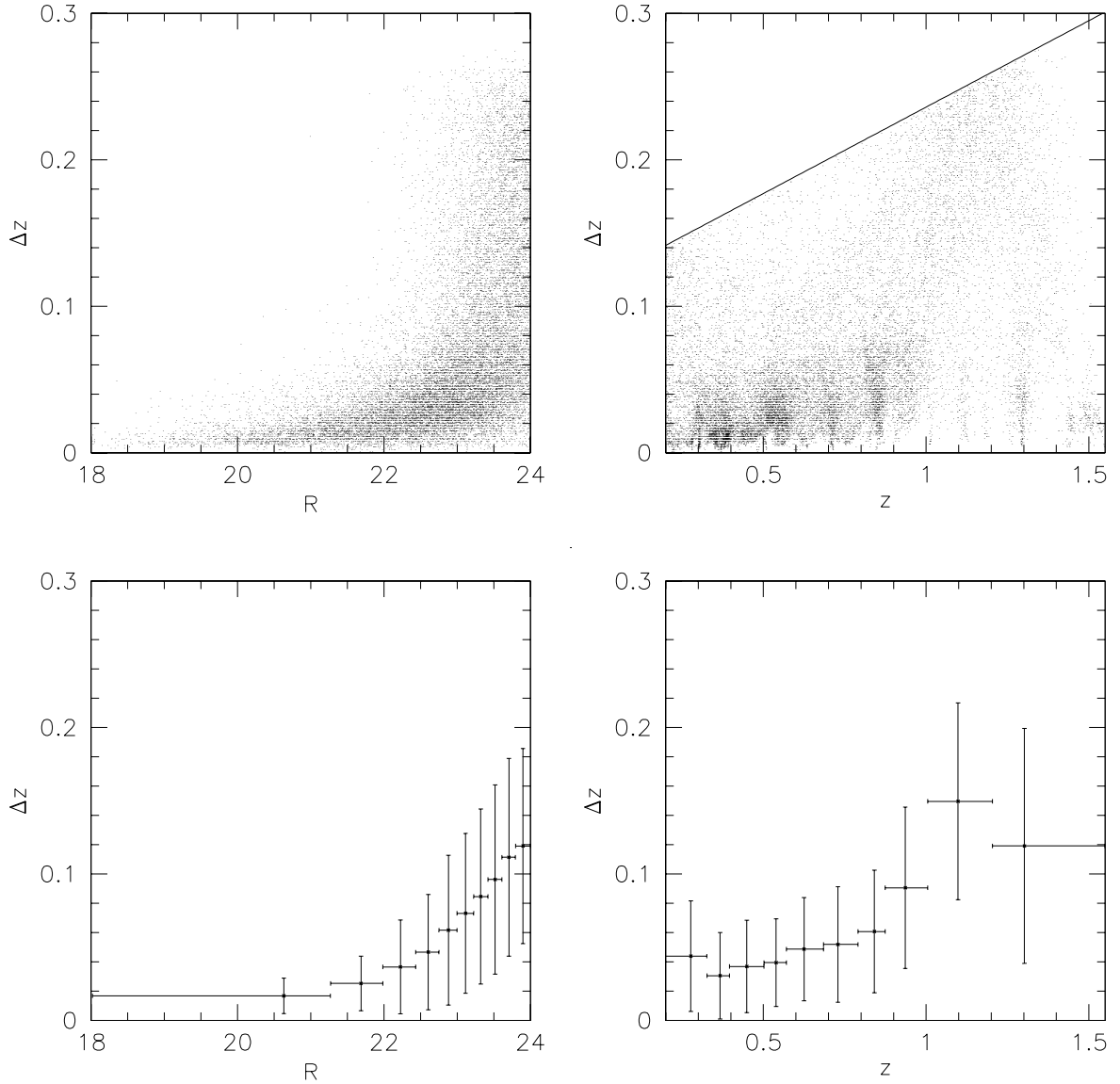


Figure 7.5: Redshift errors as function of apparent magnitude R (left panels) and redshift z (right panels) for all galaxies with $18 < R \leq 24$ and $0.2 < z \leq 1.55$. The solid line in the upper right panel is given by $(\Delta z)(z) = 0.118 \times 2.552^{\log(1+z)/\log 2.552}$ which approximates the maximum allowed redshift error as function of z , see also Sect. 5.3.2. Each bin in the lower panels contains 1940 galaxies (last bin 1941 galaxies). The data points correspond to the mean redshift error in the bin and to the median of the magnitude or redshift. Vertical errorbars give the standard deviation of the redshift error while horizontal errorbars mark the range of values of the magnitude or redshift used in that bin.

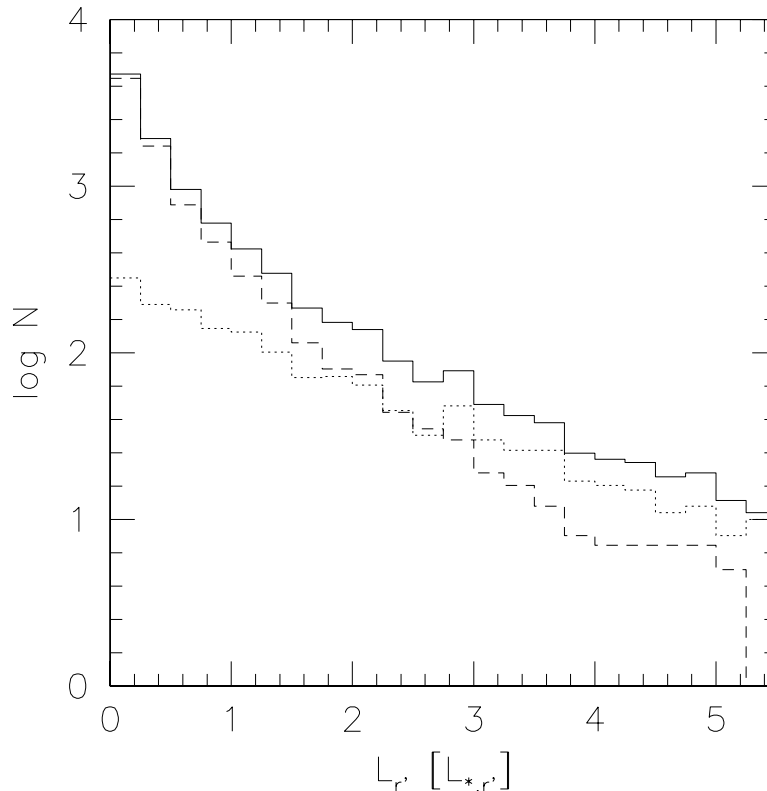


Figure 7.6: Histogram over $L_{r'}$ for galaxies with $18 < R \leq 24$ and $0.2 < z \leq 0.7$ for all SED-types (solid line), early-types (defined by $\text{SED} \leq 45$, dotted line) and late-types ($\text{SED} > 45$, dashed line). At about $L_{r'} > 2.5L_{*,r'}$ early-type galaxies become more abundant than late-type galaxies.

width of the ellipticity distribution fitted to all resolved galaxies with $18 < R \leq 24$ and $0.2 < z \leq 1.55$ is $\sigma_\epsilon = 0.362$ which is close to the peak in Fig. 7.8.

7.2.2 The measurement

For our quantitative measurement of galaxy-galaxy lensing we use the method by Schneider and Rix (1997) that has already been described briefly in Sect. 3.4.2. In this Section we will explain in detail how we use the input catalogs for the measurement.

From our object list described in Sect. 7.2.1 we use the following quantities in our program: position (x, y) in pixel; ellipticity (ϵ_1, ϵ_2) (see also Sect. 6.2); apparent magnitude in R ; redshift estimate z ; absolute magnitude M (usually $M_{r'}$, but other magnitudes can also be used); SED type; a scaled half-light radius $\theta_h^{\text{rel}} = \theta_h / \theta_{h,\text{min}}$ where $\theta_{h,\text{min}}$ is determined

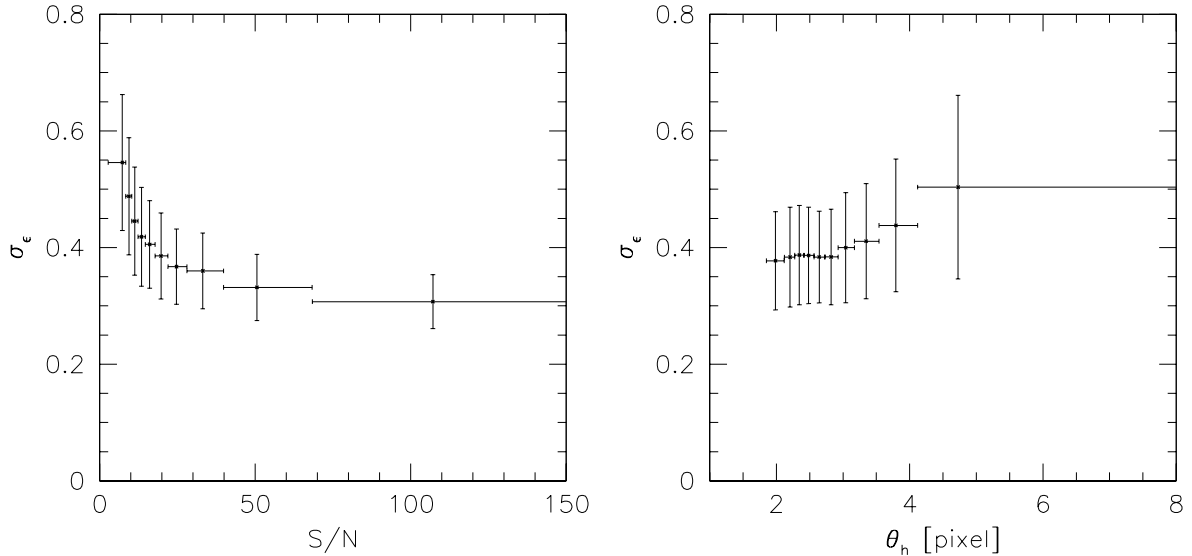


Figure 7.7: Assigned σ_ϵ as function of signal-to-noise and half-light radius for the resolved galaxies with $18 < R \leq 24$ and $0.3 < z \leq 1.55$. Each bin contains 1544 galaxies (last bin 1548 galaxies). The data points correspond to the mean σ_ϵ in the bin and to the median of the signal-to-noise or half-light radius. Vertical errorbars give the standard deviation of σ_ϵ while horizontal errorbars mark the range of values of signal-to-noise or half-light radius used in that bin.

from the PSF of the image (see also Table 7.1); assigned width of the intrinsic ellipticity distribution σ_ϵ . Table 7.5 gives an overview of the parameters that we can vary in the measurement. The actual choice of parameters will depend on the measurement performed and thus given later. Further, not all parameters given in the Table can always be given as parameter, depending on the fitted model.

First, the object list is read in and galaxies with close neighbours within $\theta_{\text{neighbour}}$ are marked. Then the object list is searched for potential sources which have to be in the required magnitude and redshift range, must be resolved ($\theta_h^{\text{rel}} > \theta_{h,\text{min}}^{\text{rel}}$) and not marked as object with close neighbour. Further, a potential source galaxy must have a minimum distance to the field boundary such that all potential lenses in the given redshift range and within $r_{p,\text{max}}$ lie within the field, see also Sect. 3.4.2. Once a potential source galaxy is identified, the object list is searched again for potential lenses for this particular source. A potential lens must fulfill the constraints given as parameter on apparent magnitude, redshift, SED type and luminosity. Further, only lens galaxies with $z_d < z_s - 0.1$ are considered. Finally, a potential lens-source pair is only taken if the projected separation θ_p and the projected physical separation r_p are within the required ranges.

When a lens-source pair is identified, the shear γ_{ij} (par1, par2) from that lens i acting on that particular source j is calculated according to the adopted lens model and for a range

Table 7.5: Parameters that can be varied in the measurement of galaxy-galaxy lensing.

Parameter	Meaning
$R_{d,\min}; R_{d,\max}$	allowed magnitude range for lenses, usually we take $R_{d,\min} = 18$ and $R_{d,\max} = 24$
$R_{s,\min}; R_{s,\max}$	allowed magnitude range for sources, usually we take $R_{s,\min} = 18$ and $R_{s,\max} = 24$
$z_{d,\min}; z_{d,\max}$	allowed redshift range for lenses, usually we take $z_{d,\min} = 0.2$ and $z_{d,\max} = 0.7$
$z_{s,\min}; z_{s,\max}$	allowed redshift range for sources, usually we take $z_{s,\min} = 0.3$ and $z_{s,\max} = 1.55$
$SED_{d,\min}; SED_{d,\max}$	allowed SED range for lenses
$L_{d,\min}; L_{d,\max}$	allowed luminosity range for lenses, measured in L_\star which is also given as parameter
$M_\odot; L_\star$	M_\odot is needed for transforming the given absolute magnitude M into luminosity L , L_\star is chosen according to the chosen absolute magnitude M . Both quantities depend on the restframe passband from which the absolute magnitude is measured.
$\eta; \eta_s$	η gives the scaling between velocity dispersion and luminosity for the SIS according to Eq. (3.35), η_s gives the scaling between outer scale and luminosity for the truncated SIS, see Eq. (3.41)
α_c	redshift dependence $c \propto (1+z)^{\alpha_c}$ of the concentration c for the NFW profile
$\theta_{h,\min}^{\text{rel}}$	minimum half-light radius relative to the PSF for source galaxies, usually $\theta_{h,\min}^{\text{rel}} = 1$ is taken
$\theta_{\text{neighbour}}$	minimum allowed projected separation in pixel to the closest neighbour for source candidates, usually $\theta_{\text{neighbour}} = 10$ is taken
$\theta_{p,\min}; \theta_{p,\max}$	range in projected separation (in pixel) that pairs are allowed to have; $\theta_{p,\min} = 35$ pixel is usually used, see also Sect. 7.1; $\theta_{p,\max}$ is used to exclude pairs with very large projected separations that are a substantial fraction of the field size, for typical combinations of $z_{d,\min}$ and $r_{p,\max}$ this parameter does not play a role
$r_{p,\min}; r_{p,\max}$	range in projected physical separation (in $h^{-1}\text{kpc}$) that pairs are allowed to have

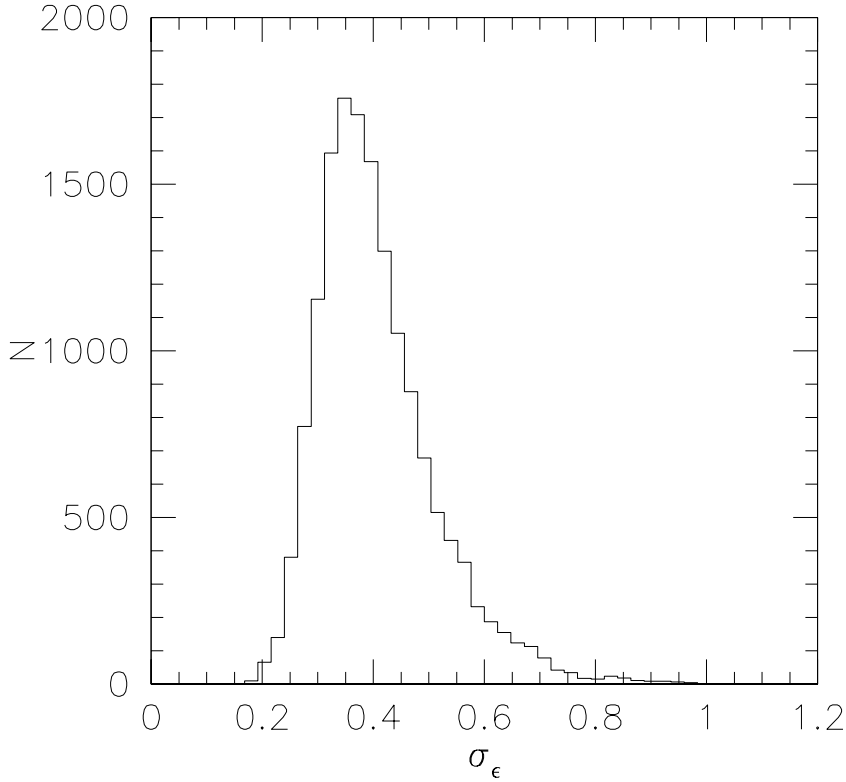


Figure 7.8: Histogram over the uncertainties in the ellipticities σ_ϵ for the resolved galaxies with $18 < R \leq 24$ and $0.3 < z \leq 1.55$.

of the fitting parameters par1 , par2 of that model. Depending on the model, one or two parameters are fitted simultaneously. From all lenses acting on a particular source j , the total shear $\gamma_j(\text{par1}, \text{par2}) = \sum_i \gamma_{ij}(\text{par1}, \text{par2})$ is added.

When all lenses acting on the source j have been identified and their shear has been taken into account, the computed shear is compared to the measured ellipticity of that source and the likelihoods of the different values of the fitting parameters are calculated. First, the intrinsic ellipticity is estimated according to [Eq. (3.51)]

$$\epsilon_{1,j}^{(s)}(\text{par1}, \text{par2}) = \epsilon_{1,j} - \gamma_{1,j}(\text{par1}, \text{par2}), \quad \epsilon_{2,j}^{(s)}(\text{par1}, \text{par2}) = \epsilon_{2,j} - \gamma_{2,j}(\text{par1}, \text{par2}). \quad (7.1)$$

The log-likelihood $\ell_j(\text{par1}, \text{par2})$ is given by [Eq. (3.54)]

$$\ell_j(\text{par1}, \text{par2}) = -\frac{[\epsilon_{1,j}^{(s)}(\text{par1}, \text{par2})]^2 + [\epsilon_{2,j}^{(s)}(\text{par1}, \text{par2})]^2}{\sigma_{\epsilon,j}^2} - \ln(\pi\sigma_{\epsilon,j}^2). \quad (7.2)$$

The total log-likelihood is given by the sum of the log-likelihoods for each source,

$$\ell(\text{par1}, \text{par2}) = \sum_j \ell_j(\text{par1}, \text{par2}). \quad (7.3)$$

7.2.3 Influence of foreground galaxy clusters in the fields

Both fields we use here contain foreground clusters of galaxies. The A901 field has been chosen specifically to study the supercluster composed of the clusters Abell 901a, 901b and 902 at a redshift of $z = 0.16$ (Gray et al., 2002). The S11 field is a random field containing the cluster Abell 1364 at a redshift of $z = 0.11$ by chance. Because we select only lens galaxies with redshifts $z_d > 0.2$, our lens sample should contain no galaxies that lie in these foreground clusters. Only a few cluster galaxies with a sufficiently large redshift error can be expected in the lens sample. It is generally assumed that in that case the foreground clusters do not affect the galaxy-galaxy lensing measurement. Although the foreground clusters will clearly distort the images of the background galaxies, this distortion should cancel out because in galaxy-galaxy lensing no preferred orientation of the lens-source pairs relative to the clusters is involved. For some of the lens-source pairs, the additional shear due to the foreground structure will lead to an overestimate of the shear due to the lens galaxies while for other pairs the shear will be underestimated. However, because the foreground clusters are fairly large, we prefer to test this assumption. We do this by modeling each cluster as SIS. Then we can calculate the shear γ_c due to the cluster(s) for each source and take it into account by using $\epsilon_j^{(s)} = \epsilon_j - \gamma_j - \gamma_c$ instead of Eq. (7.1).

Cluster in the S11 field

The S11 field contains the cluster Abell 1364 at a redshift of $z = 0.11$ (Hoessel et al., 1980). We take the brightest galaxy as the center of the cluster. This is an elliptical galaxy with $R = 15.5$ and absolute magnitude $M_r = -21.9$ at $\alpha_{J2000} = 11^{\text{h}}43^{\text{m}}29.6^{\text{s}}$ and $\delta_{J2000} = -01^{\text{h}}44^{\text{m}}29.8^{\text{s}}$. We model the cluster as SIS where σ_{S11} is the only fitting parameter. All resolved galaxies with $R = 18 - 24$ and $z = 0.2 - 1.55$ within $(500 - 5000)$ pixel from the center and without projected neighbour within 10 pixel are taken as background galaxies. This separation corresponds to about $(167 - 1670)h^{-1}$ kpc at the redshift of the cluster. 5996 sources are found. We fit the model by a maximum-likelihood technique similar to that described in Sects. 3.4.2 and 7.2.2 but with just the cluster as lens. The resulting velocity dispersion of the cluster with $1-\sigma$ errorbars is $\sigma_{S11} = 615_{-140}^{+110} \text{ km s}^{-1}$.

Clusters in the A901 field

The supercluster in the A901 field consists of the three clusters Abell 901a, Abell 901b and Abell 902 at $z = 0.16$. It has already been studied by Gray et al. (2002). They give the following central positions and velocity dispersions:

$$\text{A901a: } \alpha_{J2000} = 09^{\text{h}}56^{\text{m}}26.4^{\text{s}}, \delta_{J2000} = -09^{\text{h}}57^{\text{m}}21.7^{\text{s}}, \sigma_{A901a} = 542_{-333}^{+195} \text{ km s}^{-1}.$$

$$\begin{aligned} \text{A901b: } \alpha_{\text{J2000}} &= 09^{\text{h}}55^{\text{m}}57.4^{\text{s}}, \delta_{\text{J2000}} = -09^{\text{h}}59^{\text{m}}02.7^{\text{s}}, \sigma_{\text{A901b}} = 659_{-161}^{+129} \text{ km s}^{-1}. \\ \text{A902: } \alpha_{\text{J2000}} &= 09^{\text{h}}56^{\text{m}}33.6^{\text{s}}, \delta_{\text{J2000}} = -10^{\text{h}}09^{\text{m}}13.1^{\text{s}}, \sigma_{\text{A902}} = 738_{-384}^{+244} \text{ km s}^{-1}. \end{aligned}$$

Because Gray et al. (2002) had not yet redshift estimates available, we decided to measure again the velocity dispersions of the clusters using now the available redshifts. First, we model each of the three clusters individually without considering the two other ones. We apply the same source selection as in the case of the S11 field but using only galaxies with $z = 0.26 - 1.55$ this time. The separation of (500 – 5000) pixel corresponds to about $(230 - 2300)h^{-1}$ kpc at $z = 0.16$. 7702, 7347 and 6491 sources are found for A901a, A901b and A902. In a second step, we try to improve this model by taking the shear from the two other clusters into account. To do so we fit iteratively the velocity dispersion of one cluster while keeping those of the other two clusters fixed at the most recently fitted value. However, we note that the changes as compared to treating all three clusters individually are well within the $1\text{-}\sigma$ errorbars. We finally find $\sigma_{\text{A901a}} = 760_{-110}^{+95} \text{ km s}^{-1}$, $\sigma_{\text{A901b}} = 595_{-140}^{+115} \text{ km s}^{-1}$, $\sigma_{\text{A902}} = 375_{-375}^{+170} \text{ km s}^{-1}$. We note that the derived velocity dispersions agree only for A901b with those found by Gray et al. (2002). That for A902 is just within the errorbars quoted by Gray et al. (2002) while that for A901a falls just outside their errorbar. We do not want to further investigate these differences here. When taking the clusters into account, we will use our result as well as those of Gray et al. (2002).

Influence of the clusters

As expected, taking the cluster shear into account has hardly any influence on the results. The best-fit values of the different fits change – if at all – by much less than the $1\text{-}\sigma$ errors. Also the errorbars remain the same or become even slightly smaller. Further, the log-likelihoods are increased when considering also the cluster shear. This increase is larger when using our model of the A901 supercluster than when using the model of Gray et al. (2002). We conclude that we can safely neglect the shear from the foreground clusters. All results shown in the following Sections just consider the shear from the lens galaxies.

7.2.4 Fitting the SIS model with σ_* and η

First, we use the simple SIS model (see Sect. 2.5.1 and 3.3.1) for which we fit σ_* and η simultaneously to detect a galaxy-galaxy lensing signal and investigate the dependence on luminosity of the lenses. We obtain the best signal for pairs with separations $0 \leq r_p < 150h^{-1}$ kpc. The lower limit on r_p is only a formal one and depends on the actual measurement of the redshift of the lenses and the imposed minimum projected separation of $\theta_{\text{p,min}} = 35$ pixel. Figure 7.9 shows the result for lenses of all SED types and all luminosities. Figure 7.10 shows the same but for subsets of lenses splitted into SED type and luminosity. Table 7.6 gives the best-fit parameters for the different lens samples.

The resulting σ_* and η averaged over all lens galaxies agree quite well with expectations from the luminous parts of galaxies. η is significantly larger than zero, showing that

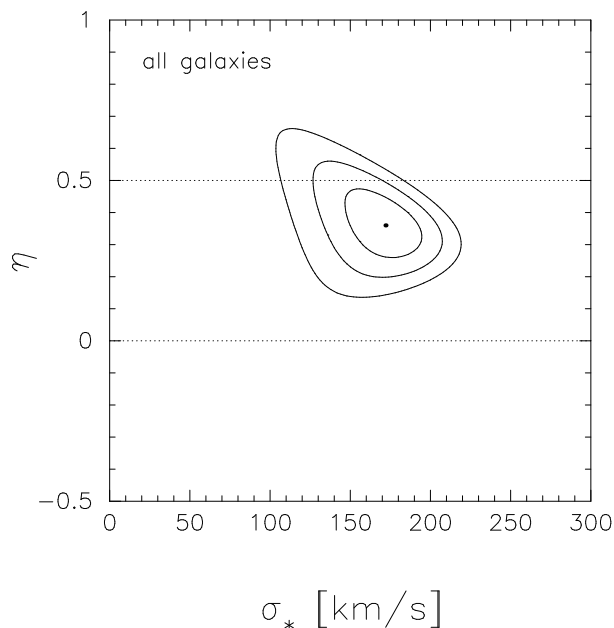


Figure 7.9: Constraints on σ_* and η from fitting an SIS model with a Tully-Fisher/ Faber-Jackson relation. Shown in this Figure are the 1-, 2- and 3- σ limits for lens galaxies of all SED types and all luminosities $L_{r'}$.

Table 7.6: Numbers of lenses N_d , sources N_s and pairs N_p used in the different fits of the SIS model. The first two columns give the selection of SED types and lens luminosity. $SED \leq 45$ corresponds to early-type galaxies while $SED > 45$ selects late-type lenses. The number of sources and thus pairs is quite different although the selection criteria only refer to the lens galaxies. The reason is that in the Table not the potential number of sources is given but the number of sources for which actually a lens within the required radius of $150h^{-1}$ kpc is found. The last two columns give the best fit values of σ_* and η with 1- σ errorbars.

SED	$L_{r'} [L_{r',*}]$	N_d	N_s	N_p	σ_* [km/s]	η
all	all	8975	12228	72573	172^{+14}_{-14}	$0.36^{+0.07}_{-0.07}$
0-45	all	1411	6748	11279	212^{+22}_{-26}	$0.24^{+0.11}_{-0.10}$
46-100	all	7564	12032	61294	156^{+20}_{-24}	$0.37^{+0.11}_{-0.11}$
all	> 1.5	921	3971	5326	250^{+58}_{-54}	$0.07^{+0.20}_{-0.22}$
all	< 1.5	8054	12204	67247	178^{+24}_{-24}	$0.49^{+0.24}_{-0.18}$

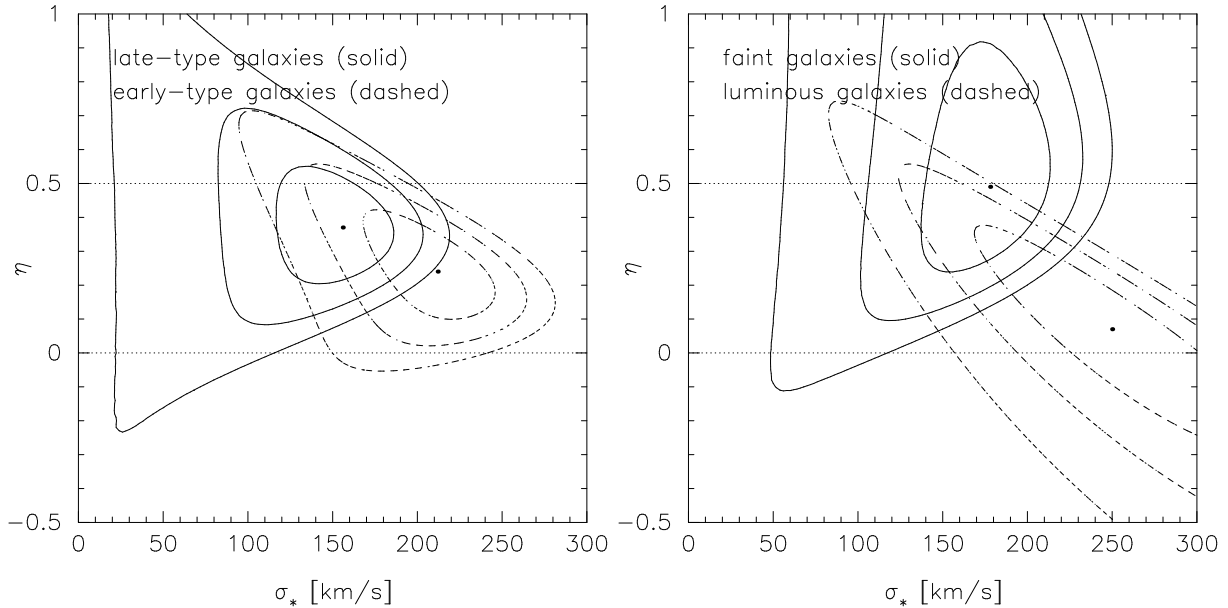


Figure 7.10: Same as Figure 7.9 but for two subsets of lens galaxies at a time. In the left panel, solid contours are for late-type lenses ($\text{SED} > 45$) and dashed contours for early-type lenses ($\text{SED} \leq 45$). In the right panel, solid contours refer to low-luminosity lenses ($L_{r'} < 1.5L_{\star,r'}$) and dashed contours to high-luminosity lenses ($L_{r'} > 1.5L_{\star,r'}$).

more luminous galaxies have larger velocity dispersions and thus larger (aperture) masses. However, splitting the lens sample into a luminous and a faint one indicates that η is larger for the faint galaxy sample. For the faint galaxy sample we find $\eta \approx 0.5$ implying constant (aperture) mass-to-light ratios independent of luminosity, while the luminous sample yields $\eta \approx 0$ in which case the velocity dispersions and thus aperture masses are independent of luminosity. The difference in η is significant at the $2\text{-}\sigma$ level. The quite different behaviour of the two subsamples raises the question whether the overall $\eta \approx 0.35$ fitted to all lenses is really related to the Tully-Fisher and Faber-Jackson relations or whether it is just the best-fit compromise from two quite different subsamples. On the other hand, the overall best-fit values lie within the $1\text{-}\sigma$ contours of both subsamples and η is not at all well constrained from these subsamples.

Splitting the lens sample into two subsamples according to the spectral types we find a $2\text{-}\sigma$ difference in the velocity dispersion which is larger for early-type galaxies. The differences in η are only given at the $1\text{-}\sigma$ level. Figure 7.6 shows that the luminous subsample is dominated by early-type galaxies while in the faint subsample late-type galaxies are more abundant. Indeed, the luminous and early-type subsamples as well as the faint and late-type subsamples are consistent with each other and show similar trends.

Our best-fit velocity dispersion $\sigma_{\star} = (172 \pm 14) \text{ km s}^{-1}$ for all lens galaxies implies a rotation velocity of $v_{\text{rot}} = \sqrt{2}\sigma_{\star} = (243 \pm 20) \text{ km s}^{-1}$. This is in the upper range of the constraints from other groups who used galaxy-galaxy lensing or satellite dynamics. However, in

most cases, the results are not directly comparable because other groups probed different radial ranges or assumed a different scaling of the velocity dispersion with luminosity. From satellite dynamics, Prada et al. (2003) find a velocity dispersion of 120 km s^{-1} inside $120h^{-1} \text{ kpc}$. Averaged over larger separations, Hoekstra et al. (2002) and McKay et al. (2001) find velocity dispersions of 130 km s^{-1} and 113 km s^{-1} , respectively. Hoekstra et al. (2002) probe projected separations out to $120''$ corresponding to about $450h^{-1} \text{ kpc}$ at the typical lens redshift in their sample ($z_d \approx 0.4$). McKay et al. (2001) use separations out to about $1h^{-1} \text{ Mpc}$ but also include the shear from neighbouring galaxies in their analysis. Velocity dispersions comparable to the one we find are also found by Hudson et al. (1998); Fischer et al. (2000); Brainerd et al. (1996) and Wilson et al. (2001). Hudson et al. (1998) find 148 km s^{-1} inside $30''$ which corresponds to a separation of $140h^{-1} \text{ kpc}$ at their typical lens redshift of $z_d \approx 0.6$. Fischer et al. (2000) obtain a velocity dispersion of $(150 - 190) \text{ km s}^{-1}$ inside about $1h^{-1} \text{ Mpc}$ while Brainerd et al. (1996) get 155 km s^{-1} inside $34''$. Wilson et al. (2001) only probe early-type galaxies for which they obtain a velocity dispersion of 168 km s^{-1} inside $200h^{-1} \text{ kpc}$.

The index η in the Tully-Fisher/Faber-Jackson relation is not fitted by most groups but fixed to some value (typically $\eta \equiv 0.25$ or $\eta \equiv 0$ is used). Those groups that constrain η obtain best-fit values very similar to ours. Hudson et al. (1998) and Smith et al. (2001) find $\eta > 0.3$. Smith et al. (2001) also find an upper limit of $\eta < 1.2$. Prada et al. (2003) also find $\eta = 0.3$ from satellite dynamics.

7.2.5 Using the SIS model to constrain the radial profile

When trying to find the optimal range in r for detecting and measuring a galaxy-galaxy lensing signal in Sect. 7.2.4 we observed that the best-fit velocity dispersion decreases when the fit is extended towards larger radii. While this contradicts the SIS model where a constant velocity dispersion is assumed, this is exactly what is expected because it is generally believed that at some point the halos of galaxies must depart from being isothermal. We realized that one can even use the simple SIS model to constrain the radial profile of lens galaxies although this model actually assumes a certain profile. We fix $\eta = 0.35$ and fit only σ_* over increasingly larger ranges in r . We use the same constraints on r_{\min} and θ_{\min} as before and vary just r_{\max} . Figure 7.11 shows the best-fit velocity dispersion fitted to all lens galaxies simultaneously as function of r_{\max} . The Figure clearly shows that the best-fit velocity dispersion is decreasing with radius. At radii above $r \approx 500h^{-1} \text{ kpc}$ it becomes flat. There is some weak indication that in the central part, until about $r = 100h^{-1} \text{ kpc}$, the velocity dispersion is even rising. We also checked from independent bins that the velocity dispersion is indeed declining outside of $100h^{-1} \text{ kpc}$: for lens-source pairs with separations below $50h^{-1} \text{ kpc}$ we obtain $\sigma_* = 164_{-34}^{+26} \text{ km s}^{-1}$, for pairs with $50h^{-1} \text{ kpc} \leq r < 100h^{-1} \text{ kpc}$ we get $\sigma_* = 186_{-24}^{+18} \text{ km s}^{-1}$, and for pairs with $100h^{-1} \text{ kpc} \leq r < 300h^{-1} \text{ kpc}$ the best-fit velocity dispersion is $\sigma_* = 122_{-32}^{+22} \text{ km s}^{-1}$. The quoted errorbars are $1\text{-}\sigma$ limits.

Figure 7.12 shows the same profile for the four different subsamples of lens galaxies that were already used in Sect. 7.2.4. At radii above $r \approx 100h^{-1} \text{ kpc}$, the shape of the profiles

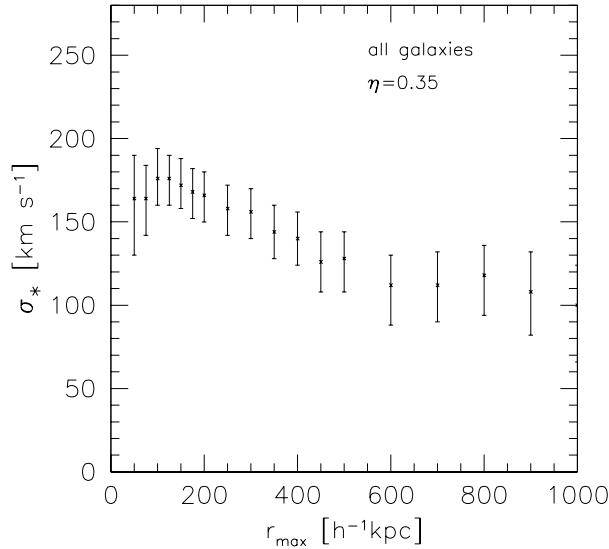


Figure 7.11: Best-fit velocity dispersion for the SIS model as function of r_{\max} where all pairs with $r < r_{\max}$ have been used in the fit. All lenses are used here and $\eta = 0.35$ is taken. The errorbars are $1\text{-}\sigma$ limits.

is the same as in Fig. 7.11. In all subsamples, the velocity dispersion is decreasing with radius and becomes flat at radii above $r \approx 500h^{-1}$ kpc. Most probably, this change in the profile does not reflect any intrinsic change in the profiles of galaxies but can be accounted for by surrounding group and cluster halos in which the lens galaxies reside. However, we find $\sigma_* \approx 120\text{km s}^{-1}$ in the flat part for all subsamples which is somewhat surprising given the expectation that the environment should be very different for the subsamples. Therefore, the radius at which the group and cluster contribution becomes important as well as its amplitude should be different for the subsamples. We checked that the flat profile at large radii is not some artefact of our measurement by measuring the radial profile around random points which results in velocity dispersions consistent with zero at all radii. Further, the flat profile cannot be explained by the foreground clusters; if we consider this additional shear as described in Sect. 7.2.3 we do not find any significant changes in the profile. One solution might be that the environment is indeed not different for our subsamples. Clearly, this has to be investigated. This hypothesis is supported by the results of McKay et al. (2001) who use galaxy-galaxy lensing to investigate lens galaxies in different environments. They find that, on average, lens galaxies in under- or overdense environment have very similar luminosities and morphological types. However, Guzik and Seljak (2002) find on the contrary that the group and cluster contribution is significantly smaller for late-type galaxies than for early-types, see also Sect. 4.2.

In the inner parts, the radial profiles for our subsamples are significantly different. For the

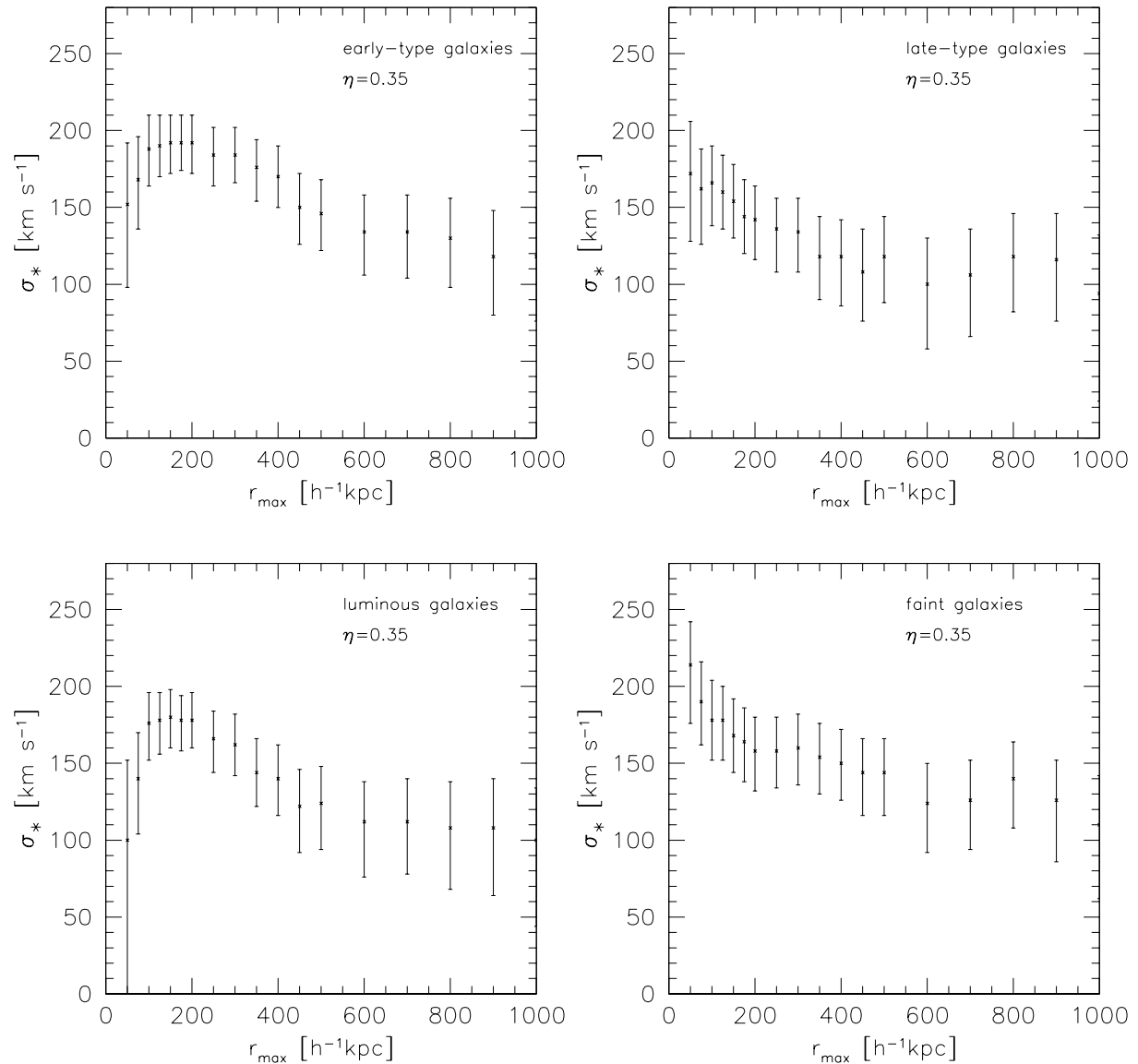


Figure 7.12: Same as Fig. 7.11 but for different lens selections. For the upper left panel early-type galaxies ($\text{SED} \leq 45$) are selected while the upper right panel is for late-type galaxies ($\text{SED} > 45$). The lower left panel refers to intrinsically luminous lenses ($L > 1.5L_{\star,r'}$) and the lower right panel to intrinsically faint lenses ($L < 1.5L_{\star,r'}$). All fits are done using $\eta = 0.35$.

early-type sample and the luminous one we find velocity dispersions that are rising with radius until about $r = 100h^{-1}$ kpc while for the late-type and faint samples the velocity dispersions are declining at all radii. This behaviour remains if we do not take $\eta = 0.35$ for all samples but use the values determined in Sect. 7.2.4, see Fig. 7.13. This is not unexpected because a change in η should affect pairs at all separations in the same way.

It might be surprising to see in Fig. 7.12 that the velocity dispersion in the inner parts is very similar for the subsamples although large differences in the best-fit σ_* were found in Sect. 7.2.4. This similarity is due to the choice of η which was allowed to vary in Sect. 7.2.4 but is fixed here. Using the best-fit values of η , the velocity dispersions in the inner parts agree more with the expectations from Sect. 7.2.4, see Fig. 7.13.

A rising velocity curve is expected if galaxies can be described by NFW profiles, see Sect. 2.5.3. However, if the early-type and luminous samples can be described by NFW profiles, then the same should be true for the late-type and faint samples. The absence of a peak in the observed velocity profile then means that this peak must occur at smaller radius where our measurement is not sensitive enough to detect it. Indeed, because $r_s = r_{\text{vir}}/c$ [see Eq. (2.19)] and luminous or early-type galaxies are thought to be more massive than faint or late-type galaxies and have thus larger virial radii and smaller concentrations, this agrees with the expectations.

However, there could also be different explanations for the rise in the velocity profile. In Sect. 7.1 we saw that lens-source pairs with small projected angular separations θ_p can bias the galaxy-galaxy lensing measurement towards systematically too low signal, see Table 7.2. To avoid this bias we determined the best $\theta_{\text{neighbour}}$ and $\theta_{p,\text{min}}$ for the whole sample. But it might well be that we have to choose larger minimum separations for the early-type and luminous samples because these galaxies could be larger than the average and therefore introduce a larger bias. To check this, we calculate the average half-light radius θ_h for our different samples. For the early-type sample we find $\theta_{h,\text{early}} = 2.78 \pm 1.02$ pixel and $\theta_{h,\text{late}} = 2.77 \pm 1.00$ pixel for the late-type sample. Therefore, it is very improbable that the different radial profiles of the early- and late-type samples can be accounted for by an uncorrected bias due to close pairs. For the luminous and faint samples we find $\theta_{h,\text{lum}} = 3.56 \pm 1.12$ pixel and $\theta_{h,\text{faint}} = 2.69 \pm 0.96$ pixel, respectively. Therefore, we check for the luminous sample how the velocity profile changes if we increase $\theta_{\text{neighbour}}$ and $\theta_{p,\text{min}}$. As already found in Sect. 7.1, varying $\theta_{\text{neighbour}}$ does not have a significant effect. So we keep $\theta_{\text{neighbour}} = 10$ pixel fixed and just vary $\theta_{p,\text{min}}$. In Fig. 7.14 we show the inner profile for different choices of $\theta_{p,\text{min}}$. From the mean half-light radius of the luminous sample compared to that of all lens candidates [$\theta_{h,\text{all}} = 2.77 \pm 1.00$ pixel] one would expect $\theta_{p,\text{min}} = \frac{3.56}{2.77} \times 35$ pixel ≈ 45 pixel to be a good choice. No difference in the corresponding profile is seen compared to that with $\theta_{p,\text{min}} = 35$ pixel. If $\theta_{p,\text{min}}$ is further increased to 60 pixel, the innermost data point is changed while the others remain very similar. However, the problem is that if a large $\theta_{p,\text{min}}$ is chosen, many pairs that contribute to the innermost bin are excluded. For $\theta_{p,\text{min}} = 35$ pixel 247 lenses contribute to the innermost bin while 121 lenses contribute to it for $\theta_{p,\text{min}} = 45$ pixel and only 25 lenses are left for $\theta_{p,\text{min}} = 60$ pixel. The number of lenses for the second bin is changed by less than a factor of 2. Therefore, the innermost data point becomes more affected by small-number statistics.

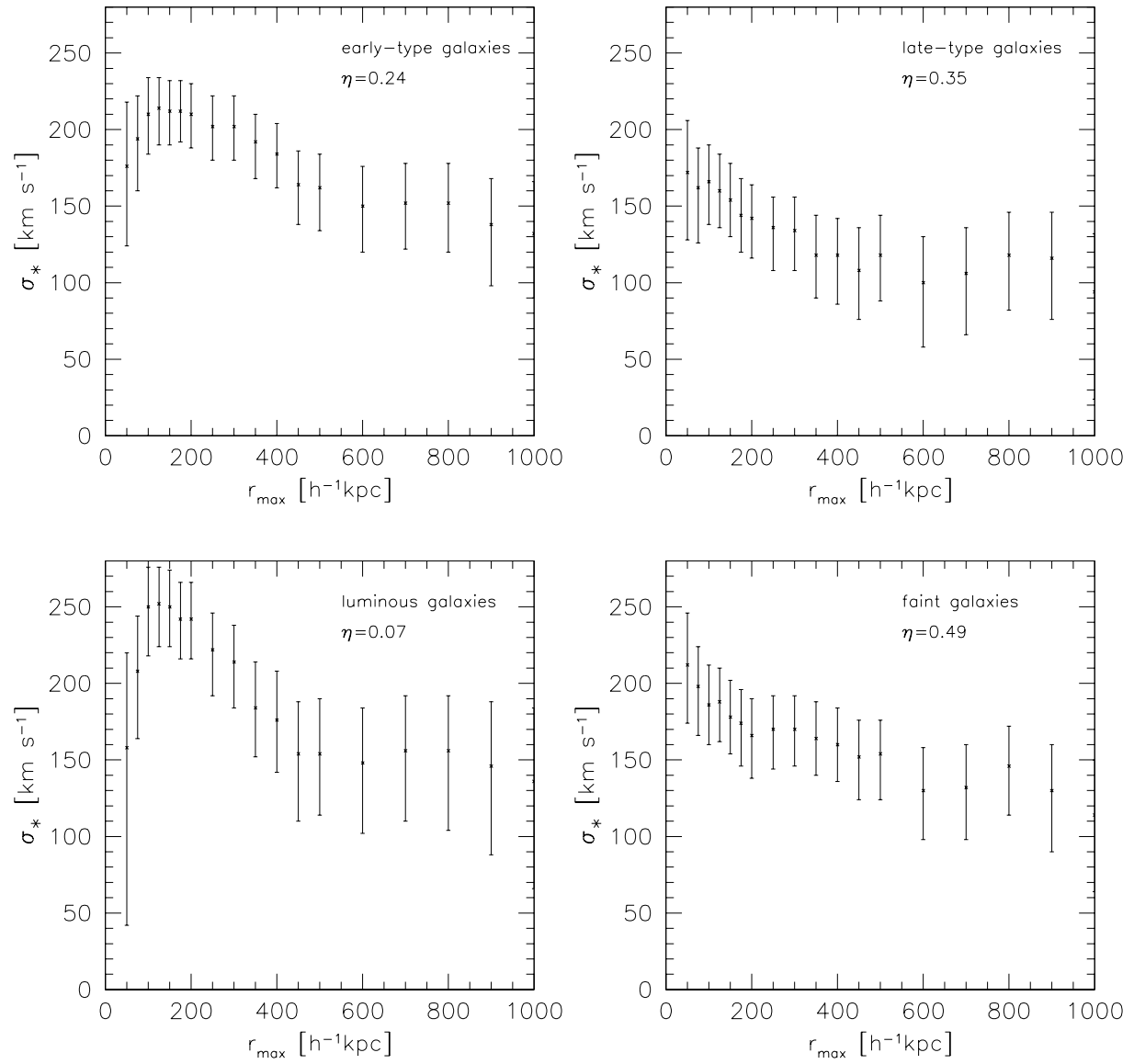


Figure 7.13: Same as Fig. 7.12 but using the values of η given in Table 7.6 for the different samples.

We summarize that no clear evidence for a biased inner radial profile is seen. But even if such bias exists and is taken into account, the radial profile of the luminous sample is clearly not decreasing in the inner parts but at most flat. Therefore, we conclude that we found evidence for different shapes of the inner radial profiles of the faint and luminous samples as well as of the early- and late-type samples.

To get significant results on the inner velocity profile, one should investigate in more detail at which minimum separation $\theta_{p,\min}$ the shape measurements can still be trusted. This could for example be done by investigating the alignment of galaxies with stars or with other galaxies or quasars at higher redshift. In these cases, no lensing occurs and thus no alignment should be detected on average. Therefore, any detection of such alignment directly indicates biased shape measurements. With sufficiently large data sets one could even try to determine $\theta_{p,\min}$ as function of half-light radius of the lenses.

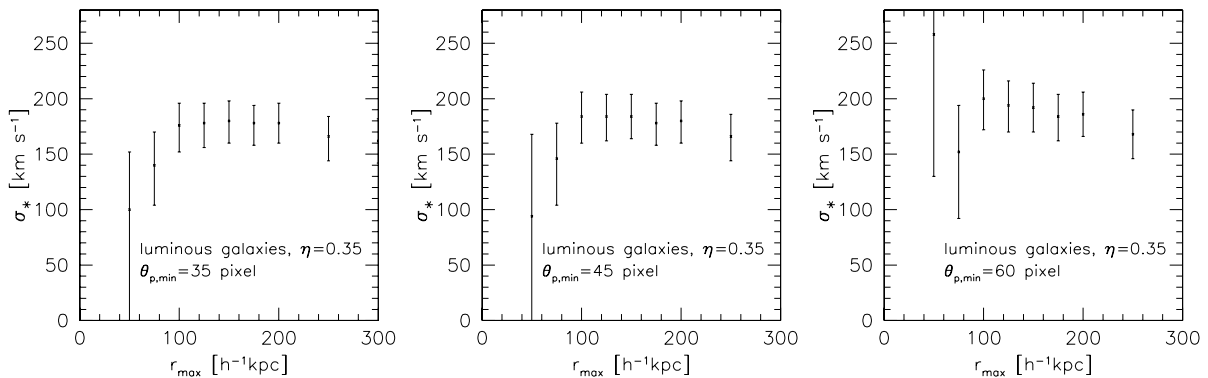


Figure 7.14: Same as Fig. 7.12 for just the luminous sample and only for $r_{\max} \leq 300h^{-1}$ kpc. The three panels differ in the choice of $\theta_{p,\min}$; $\theta_{p,\min} = 35$ pixel for the left panel, $\theta_{p,\min} = 45$ pixel for the middle panel and $\theta_{p,\min} = 60$ pixel for the right panel.

7.2.6 Fitting the truncated SIS model

In this Section we fit the truncated SIS model, see Sects. 2.5.2 and 3.3.2. We first use $\eta_s = 0.5$ and $\eta = 0.35$ and figure out the optimal range in r_p over which lens-source pairs are considered. If $r_{p,\max}$ is too small, we cannot expect to be able to constrain the radial profile while, if $r_{p,\max}$ is too large, we are affected by the size of the field and lose too many lenses close to the field boundary. We finally end up with $r_{p,\max} = 400h^{-1}$ kpc. Figure 7.15 shows the resulting contour plot when all lenses are used in the fit and $\eta = 0.35$ and $\eta_s = 0.5$ are chosen. Marginalization over σ_* yields a 2- σ upper limit of $s_* \leq 92h^{-1}$ kpc and a 3- σ upper limit of $s_* \leq 460h^{-1}$ kpc. The 3- σ contours stay almost parallel for increasing s_* and do not close until $s_* = 1000h^{-1}$ kpc. The best-fit values of σ_* and s_* with their 1- σ limits are $\sigma_* = 202_{-24}^{+32}$ and $s_* = 32_{-16}^{+20}$ kpc. 385121 pairs from 8315 lenses and 9740 sources

have contributed to the fit. We also used other values of η_s . For $\eta_s = 0.0$ and $\eta_s = 1.0$ the contours become larger yielding $2\text{-}\sigma$ upper limits of about $s_\star \leq 120h^{-1}$ kpc in both cases. The $3\text{-}\sigma$ upper limits are larger than $1000h^{-1}$ kpc. In both cases, the log-likelihood is smaller than for $\eta_s = 0.5$.

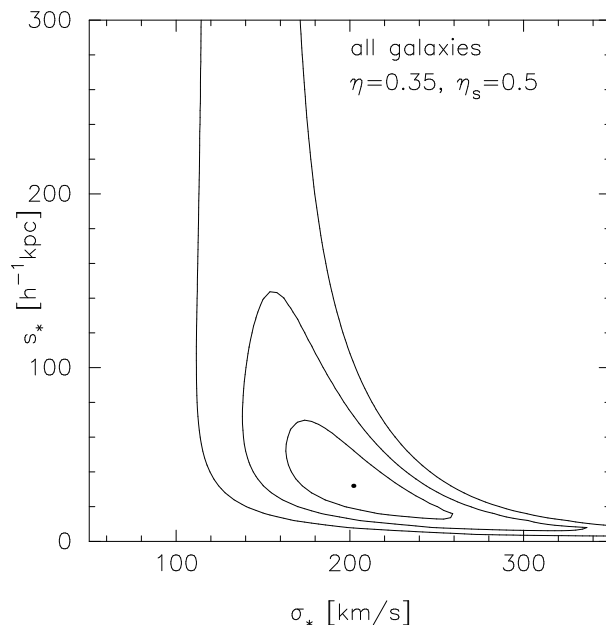


Figure 7.15: Fit of the truncated SIS model to all lenses. All pairs with $r < 400h^{-1}$ kpc are used. $\eta = 0.35$ and $\eta_s = 0.5$ is taken. Shown are the 1-, 2- and 3- σ contours.

We next split the lens sample into subsamples as in the previous Sections, see Fig. 7.16. A $2\text{-}\sigma$ upper limit on s_\star is only detected for the early-type [$s_\star \leq 156h^{-1}$ kpc] and luminous [$s_\star \leq 112h^{-1}$ kpc] samples. The contours for the different samples are very similar and we lack the signal-to-noise to detect any dependence of s_\star on the lens selection. However, it is interesting to note that our constraints on s_\star seem to come mostly from the luminous sample. These conclusions remain unchanged when using the best-fit values of η from Sect. 7.2.4 for the subsamples instead of $\eta = 0.35$. Then even the $1\text{-}\sigma$ contour of the faint sample does not stay closed while the $2\text{-}\sigma$ contour becomes smaller for the luminous sample. Figure 7.16 shows that the best-fit velocity dispersion is very similar for the luminous and the faint samples. Again, this is due to our choice of $\eta = 0.35$. For the best-fit values of η from Sect. 7.2.4, we obtain a larger velocity dispersion for the luminous sample than for the faint one.

Our limit on s_\star is significantly smaller than that obtained by Hoekstra et al. (2002) who find $s_\star = 313_{-81}^{+136}$ kpc [$1\text{-}\sigma$ errors] for $\eta_s = 0.5$ but using $\eta = 0.25$. Their best-fit s_\star is excluded by our measurement at the $2\text{-}\sigma$ level. If we use $\eta = 0.25$ we still find $s_\star = 24$ kpc, but the $3\text{-}\sigma$ upper limit is even reduced to $s_\star \leq 160h^{-1}$ kpc. From the galaxy-galaxy lensing analyses of SDSS data, a $2\text{-}\sigma$ lower limit of about $s_\star \geq 200h^{-1}$ kpc is obtained

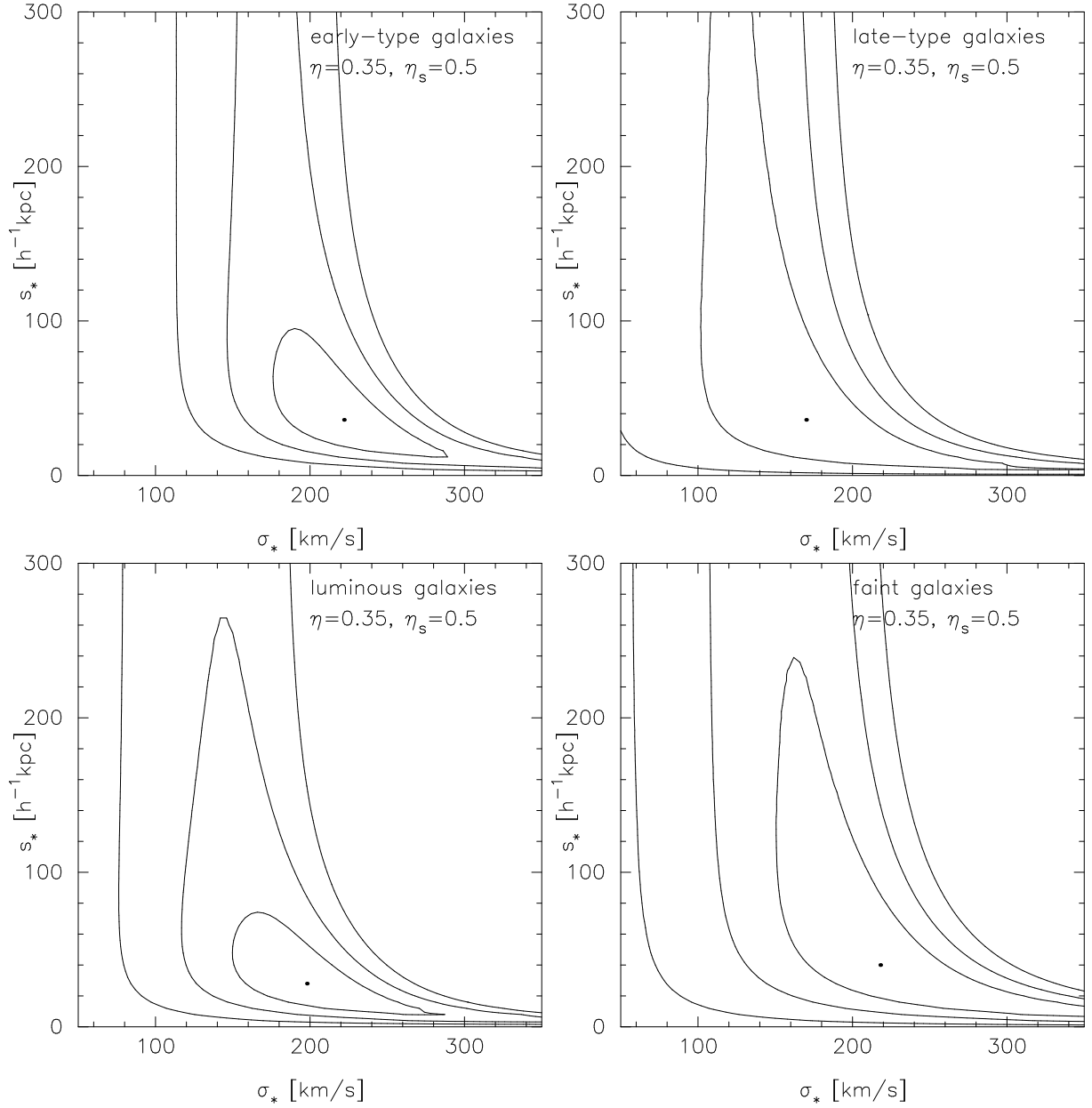


Figure 7.16: Same as Fig. 7.15, but for the different subsamples of lens galaxies. For the upper left panel early-type galaxies ($\text{SED} \leq 45$) are selected while the upper right panel is for late-type galaxies ($\text{SED} > 45$). The lower left panel refers to intrinsically luminous lenses ($L > 1.5L_{*,r'}$) and the lower right panel to intrinsically faint lenses ($L < 1.5L_{*,r'}$). All fits are done using $\eta = 0.35$ and $\eta_s = 0.5$.

(Fischer et al., 2000; McKay et al., 2001). Only Hudson et al. (1998) find s_* comparable to ours. They also find lower limits on s_* that are close to zero [below $10h^{-1}$ kpc], just as we do. Both, Hoekstra et al. (2002) and Hudson et al. (1998), probe lens galaxies in a redshift range comparable to ours and use the method of Schneider and Rix (1997) to account for shear contributions from several lenses. Therefore, we do not see any obvious reason why our results on s_* should be so different. $30h^{-1}$ kpc at a typical lens redshift of $z_d \approx 0.4$ correspond to 33 pixel. Therefore, boundary effects from the size of the field should be completely negligible. However, the required minimum projected separation $\theta_{p,\min} = 35$ pixel between lenses and sources implies that we basically probe halos outside of s_* . Therefore, the questions arises if the best-fit s_* is changed for different selections of $\theta_{p,\min}$ and $r_{p,\min}$. However, increasing these two parameters up to $\theta_{p,\min} = 50$ pixel or $r_{p,\min} = 100h^{-1}$ kpc only makes the contours wider but does not shift s_* towards larger values.

7.2.7 Fitting the NFW profile

Finally, we parametrize the lens galaxies by the NFW profile. We use the concentration c and the virial radius r_{vir} as parameters. We choose again $r_{p,\max} = 400h^{-1}$ kpc. Taken both quantities to be the same for all lenses, we arrive at the contour plot shown in Fig. 7.17. The virial radius is quite well constrained, while on the concentration only a lower limit can be obtained. In Fig. 7.18 we show the corresponding plots for the four subsamples. Table 7.7 gives the best-fit values of the virial radius together with the resulting virial masses and velocities and the lower limits on the concentration for the different lens selections.

Table 7.7: Best-fit virial radii r_{vir} , virial masses M_{vir} and rotation velocities v_{vir} at the virial radius with $1\text{-}\sigma$ errorbars for different lens selections. Also given is the $1\text{-}\sigma$ lower limit on the concentration c . For all fits it was assumed that the concentration and virial radius are the same for all lenses. In the last column we give the theoretical estimate of the concentration from Eq. (2.24).

SED	$L_{r'}$ [$L_{r',*}$]	N_d	N_s	N_p	r_{vir} [h^{-1} kpc]	M_{vir} [$10^{11}h^{-1}M_{\odot}$]	v_{vir} [km/s]	c_{\min}	c_{th}
all	all	8315	9740	385121	150^{+20}_{-20}	$2.4^{+1.0}_{-0.9}$	83^{+11}_{-11}	6	18
0-45	all	1320	9378	59688	290^{+30}_{-40}	$17.0^{+5.9}_{-6.1}$	161^{+17}_{-22}	8	12
46-100	all	6995	9729	325433	120^{+20}_{-40}	$1.2^{+0.7}_{-0.85}$	67^{+11}_{-23}	0	17
	> 1.5	863	7744	27898	280^{+30}_{-20}	$15.3^{+5.5}_{-3.0}$	155^{+17}_{-11}	20	12
	< 1.5	7452	9737	357223	130^{+30}_{-20}	$1.5^{+1.4}_{-0.6}$	72^{+17}_{-11}	0	16

We also used a parametrization of the concentration with redshift, $c \propto (1+z)^{-1}$ [see Eq. (2.25)], but obtained almost identical results. Only the lower limit on c becomes larger by (30-70)% for the lens samples for which a lower limit is detected. This increase in c is just

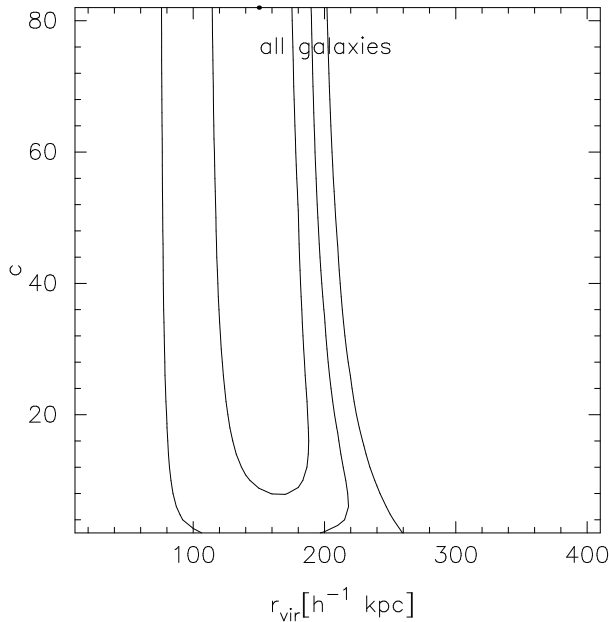


Figure 7.17: Fit of the NFW profile to all lens galaxies. The parameters c and r_{vir} are taken to be the same for all galaxies.

as much as is needed to obtain the same concentration for lenses at redshifts $z = 0.3 - 0.7$ as in the case before where c was assumed to be independent of redshift.

Table 7.7 shows that early-type or luminous galaxies have 2 to 2.5 times larger virial radii than late-type or faint galaxies which is significant at more than $3-\sigma$. The difference in the virial mass is correspondingly about a factor of 10. The rotation velocity at the virial radius v_{vir} is proportional to the virial radius, $v_{\text{vir}}/(\text{km s}^{-1}) = 0.555 r_{\text{vir}}/\text{kpc}$ [see Sect. 2.5.3] and thus differs also by a factor of 2 to 2.5. Note that M_{vir} and v_{vir} are independent of the concentration. However, the maximum rotation velocity v_{max} and the corresponding radius $r_{v_{\text{max}}}$ at which the maximum occurs, are not independent of c but given by $r_{v_{\text{max}}}/r_{\text{vir}} = 2.16/c$ and $v_{\text{max}}/v_{\text{vir}} = 0.46 \left(\frac{c}{\ln(1+c) - c/(1+c)} \right)^{1/2}$ for $\Delta_{\text{vir}} = 200$. Table 7.8 gives these ratios for some values of c . For small concentrations, the maximum rotation velocity is almost identical to v_{vir} . If one assumes $c = 25$ for the late-type or faint lens sample, then $v_{\text{max}} \approx 105 \text{ km s}^{-1}$ for these galaxies. This can however not be compared directly to the much larger rotation velocities found for the SIS and truncated SIS [$v_{\text{rot}} = \sqrt{2}\sigma_v$] because for these models only the velocity dispersion and thus rotation velocity of L_* -galaxies was fitted. A parametrization of the relation between v_{vir} or v_{max} of the NFW profile and the luminosity of the lens galaxies is needed to carry out this comparison.

Guzik and Seljak (2002) use galaxy-lensing to determine virial masses of L_* -galaxies. From measurements in the r' -band they obtain $M_{\text{vir}} = (7 - 9) \times 10^{11} h^{-1} M_{\odot}$, depending on how the group/cluster contribution is modeled. This is larger than our estimate for all galaxies

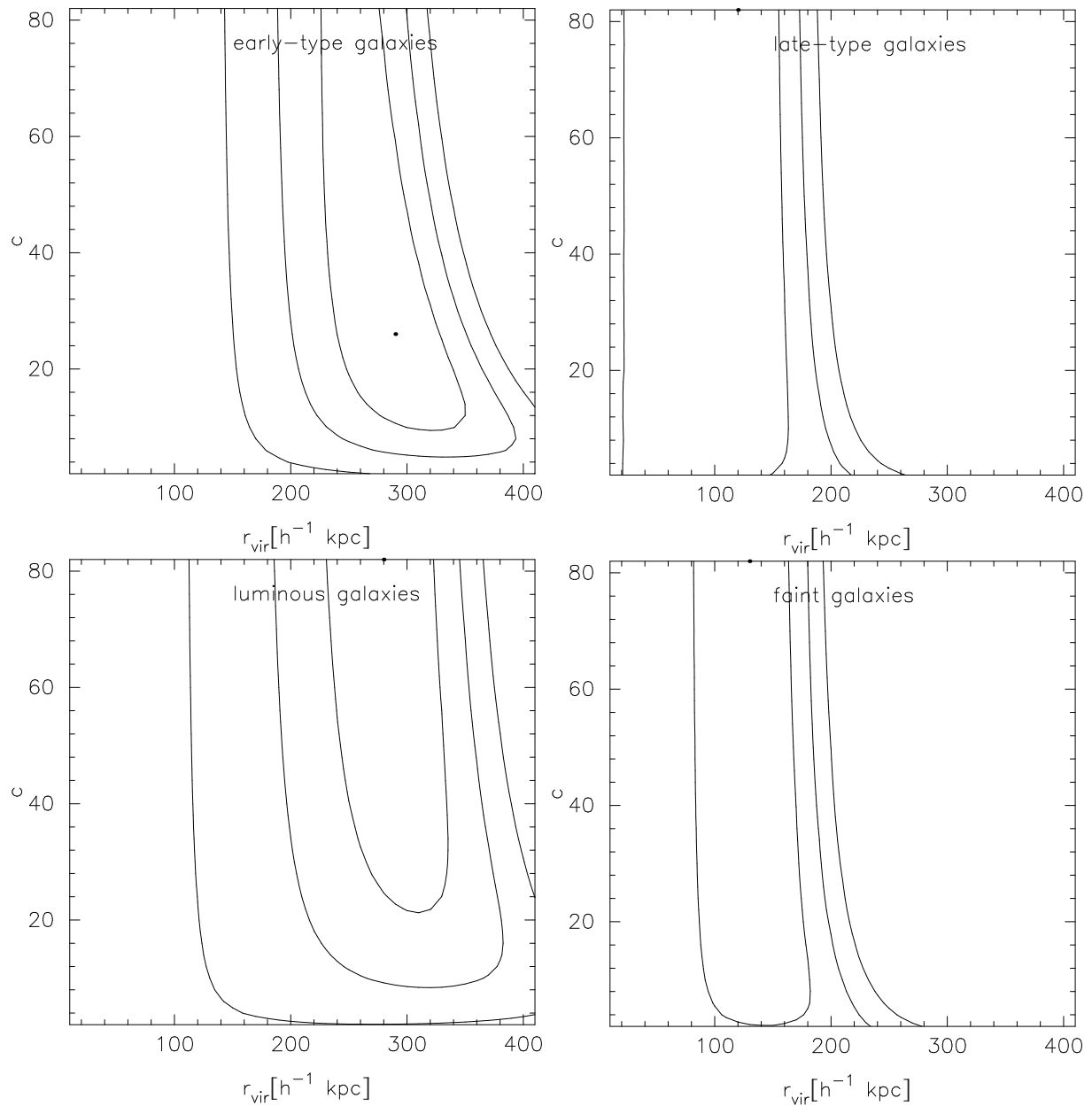


Figure 7.18: Same as Fig. 7.17, but for the different lens selections. For the upper left panel early-type galaxies ($\text{SED} \leq 45$) are selected while the upper right panel is for late-type galaxies ($\text{SED} > 45$). The lower left panel refers to intrinsically luminous lenses ($L > 1.5L_{*,r'}$) and the lower right panel to intrinsically faint lenses ($L < 1.5L_{*,r'}$).

together. However, Table 7.7 shows that the best-fit virial mass of all galaxies is dominated by the late-type or faint samples. Therefore, it is hard to estimate what the virial mass of an L_* -galaxy would be. Guzik and Seljak (2002) also split their lens sample into an early-type and late-type subsample for which they obtain $M_{\text{vir}} = (11.7 \pm 2.5) \times 10^{11} h^{-1} M_{\odot}$ and $M_{\text{vir}} = (3.3 \pm 2.1) \times 10^{11} h^{-1} M_{\odot}$, respectively. Again, this is not directly comparable to our findings due to different definitions of early- and late-type lenses and due to the different ranges in lens luminosity involved in the fits. However, our results and those from Guzik and Seljak (2002) are on the same order of magnitude which gives some confidence that they are actually consistent.

Table 7.8: Maximum rotation velocities v_{max} and radii $r_{v_{\text{max}}}$ at which they occur relative to the rotation velocity at the virial radius v_{vir} and virial radius r_{vir} for different concentrations c .

c	$r_{v_{\text{max}}}/r_{\text{vir}}$	$v_{\text{max}}/v_{\text{vir}}$
5	0.43	1.05
10	0.22	1.19
15	0.14	1.32
20	0.11	1.42
25	0.09	1.52

7.2.8 Mass estimates and comparison of the models

We use the best-fit parameters for the three different lens models (SIS, truncated SIS and NFW) to plot the integrated mass as function of radius. For the SIS the values of the parameters are given in Table 7.6. For the truncated SIS we use the best-fit velocity dispersion and outer scale for the best-fit η from Sect. 7.2.4. For all lens galaxies these parameters are given in Sect. 7.2.6. For the early-type sample we use $(\sigma_*, s_*) = (240 \text{ km s}^{-1}, 40h^{-1} \text{ kpc})$, for the late-type sample $(\sigma_*, s_*) = (170 \text{ km s}^{-1}, 36h^{-1} \text{ kpc})$, for the luminous sample $(\sigma_*, s_*) = (296 \text{ km s}^{-1}, 20h^{-1} \text{ kpc})$, and for the faint sample $(\sigma_*, s_*) = (208 \text{ km s}^{-1}, 60h^{-1} \text{ kpc})$. The virial radii for the NFW model are given in Table 7.7. We assume $c = 10$ for all lens samples. However, Fig. 2.4 shows that the aperture mass does not depend strongly on the concentration for fixed virial radius. The aperture masses for the different lens samples are shown in Fig. 7.19.

Due to the smallness of the outer scale, the aperture mass for the truncated SIS starts to deviate from that for the SIS already at small radii, at $50h^{-1} \text{ kpc}$ or less. For the truncated SIS, a total mass of the galaxies is defined [see Eq. (2.14)]. For all lens galaxies together, the estimate of the averaged total mass is $M_{\text{SIStrunc}} = 2.4 \times h^{-1} 10^{11} M_{\odot}$ which is exactly the best-fit virial mass for the NFW model. However, for the subsamples, the agreement between the mass estimates from the truncated SIS and the NFW model is less good. Again, one has to keep in mind that for the SIS and truncated SIS a scaling

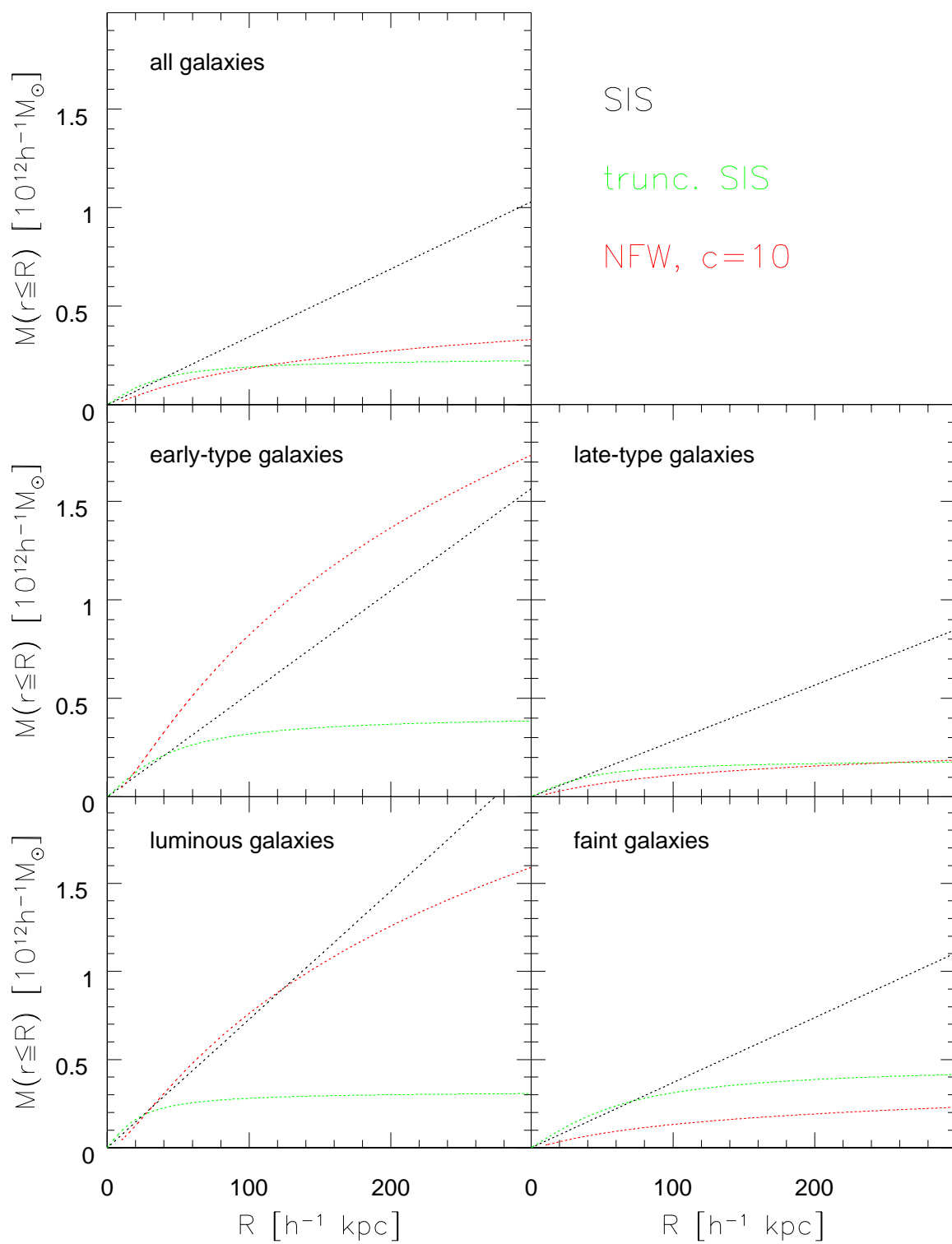


Figure 7.19: Aperture masses for the different lens models and lens selections.

relation between the velocity dispersion and the luminosity of the lens galaxies was taken into account which is not the case for the NFW model. Therefore, the mass estimates from the two different classes of models cannot be compared directly.

Finally, it is interesting to compare the quality of the fits for the truncated SIS and the NFW model. Both models have two parameters and the fits include exactly the same lens-source pairs. The log-likelihood of the best-fit parameters for the whole lens sample as well as for the subsamples is always larger for the truncated SIS than for the NFW model. The difference is smaller for the subsamples of luminous or late-type galaxies ($\ell_{\text{trSIS}} - \ell_{\text{NFW}} = 1.60$ for luminous and $\ell_{\text{trSIS}} - \ell_{\text{NFW}} = 2.47$ for late-type galaxies) than for the subsamples of faint or early-type galaxies ($\ell_{\text{trSIS}} - \ell_{\text{NFW}} = 5.20$ for faint and $\ell_{\text{trSIS}} - \ell_{\text{NFW}} = 3.20$ for early-type galaxies). However, two things have to be kept in mind: first, the derived best-fit parameters of the NFW model are probably not the real minima of the log-likelihood function because they lie at the maximum concentration c considered in the parameter space for all sample but the one of early-type galaxies, see Figs. 7.17 and 7.18. Second, it can well be expected that the log-likelihood increases if not the concentration c is fitted but if a second parameter describing the relation between virial radius or virial mass and luminosity of the galaxies is chosen instead. Therefore, it seems to early to conclude that the truncated SIS provides a better fit to the data.

7.2.9 Summary

We used the maximum-likelihood method of Schneider and Rix (1997) to investigate the dark matter halos of lens galaxies at $z = 0.2 - 0.7$ in two of the COMBO-17 fields. Using the SIS model together with a Tully-Fisher/Faber-Jackson relation, a clear lensing signal is detected with a best-fit velocity dispersion for L_* -galaxies of $\sigma_* = (172 \pm 14) \text{ km s}^{-1}$ ($1\text{-}\sigma$ limits) and a relation between luminosity and velocity dispersion of the form $\sigma_v \propto L^\eta$ with $\eta = 0.36 \pm 0.07$. The derived velocity dispersion is in the upper range of constraints obtained by other groups while the best-fit η agrees well with results from other groups and the expectations from the central parts of galaxies. Splitting the lens sample into an early- and late-type sample or a luminous and faint sample we find larger σ_* and a weaker dependence of the velocity dispersion on luminosity (smaller η) for the early-type and luminous samples than for the late-type and faint samples. These differences are most striking for the lens selection based on luminosity: for the faint sample constant (aperture) mass-to-light ratios independent of the luminosity are favoured while the luminous sample favours masses being independent of the luminosity.

In Sect. 7.2.5 we presented evidence for a radial dependence of the best-fit velocity dispersion which is declining outside of at least $200h^{-1} \text{ kpc}$, depending on the lens selection. This contradicts the SIS model for which a constant velocity dispersion is assumed. For the luminous and early-type samples we even found a rising velocity dispersion in the inner approximately $100h^{-1} \text{ kpc}$. We tested whether the rise in the inner parts could be due to observational biases from shape measurements that are affected by close neighbours of the objects. We did not find evidence for such a bias but can, on the other hand, not rule out that the velocity dispersion is flat in the inner parts instead of being rising. However, the

velocity dispersion for the late-type and faint samples is clearly declining from the smallest separation measured. Therefore, we can conclude that the velocity dispersion as function of radius behaves differently at small radii in early-type and luminous galaxies on the one hand and late-type and faint galaxies on the other hand, implying that the central density profile of these classes of galaxies is different.

Fitting the truncated SIS model also yields evidence against the SIS model. We find a surprisingly small outer scale of only $30h^{-1}$ kpc implying that half the mass of the galaxies is contained within this small radius, if the model is correct.

Finally, we fitted the NFW profile. We found only lower limits on the concentration c but obtained quite tight constraints on the virial radius. For the whole lens sample, the virial radius is about $150h^{-1}$ kpc. It is larger for the early-type and luminous samples (around $280h^{-1}$ kpc) and smaller for the late-type and faint samples (around $130h^{-1}$ kpc). The resulting virial masses are about $1.5 \times 10^{11}h^{-1}M_{\odot}$ for the late-type and faint samples and about 10 times larger for the early-type and luminous samples.

Our modeling of the lens galaxies did not yet take into account a possible contribution from group or cluster halos surrounding the lens galaxies. Therefore, the next step will be to investigate the influence of the environment of the lens galaxies on the measurement. This can first be done by splitting the lens sample into two subsamples of galaxies in over- and underdense regions. Next, one can try to adopt some parametrized model of the group and cluster contribution as Guzik and Seljak (2002) have proposed. It is well possible that some of our conclusion might not reflect intrinsic properties of the lens galaxy sample but could be explained by different environments.

Chapter 8

Outlook

In this thesis, we used data from the COMBO-17 survey for weak lensing studies. Two main questions have been addressed: the reliability of shape measurements of small galaxies and the detection and quantitative analysis of galaxy-galaxy lensing which allows us to put constraints on the dark matter halos of galaxies. The results are already summarized in Sects. 6.3.6 and 7.2.9.

The main finding from the comparison of shape measurements in Sect. 6.3 is that shape measurements are mostly limited by the seeing conditions. However, the seeing does not deteriorate shape measurements from all objects in the same way – its influence is stronger on objects with e.g. smaller signal-to-noise or smaller half-light radii. Further, objects that have a larger uncertainty in the measured ellipticities typically also have been corrected by a larger correction factor and have larger ellipticities after the correction. This knowledge can be used to assign weights to the shape measurements of objects. With these weights it is possible to use all detected objects in a weak lensing measurement and to extract the information that is available even from the objects that are most affected by observational noise. Such a weighting scheme based on the signal-to-noise and half-light-radius of objects was developed by Erben et al. (2001). We tested it together with other weighting schemes by investigating how well a galaxy-galaxy lensing measurement can be reproduced from independent observations of the same field. We find that the weighting scheme by Erben et al. (2001) is able to improve the measurement as compared to no weighting. However, it can still be improved by e.g. assigning the weights based on the correction factor P^g and the signal-to-noise instead of half-light-radius and signal-to-noise. Then the errorbars are further reduced and the agreement between the galaxy-galaxy lensing measurements from the independent data sets is further improved.

Our quantitative galaxy-galaxy lensing measurements are based on just two out of four COMBO-17 fields that are in principle available for these studies. For one of the remaining fields, data reduction has not been finished yet while in the other field we were not able to detect a galaxy-galaxy lensing signal that is consistent with the two fields used here. We plan to further investigate this field and to try to find out if this field is intrinsically different from the other ones or if observational problems could be made responsible. This field is the prominent CDFS field for which a wealth of data is available. We already used

it to investigate the reliability of shape measurements so that it should be possible to find out if any biases in the data reduction exist. However, we note that this field also seems to be intrinsically a particular field. It was selected because of its emptiness – no bright structures like galaxy clusters are seen. Indeed, a derivation of the luminosity functions for this field and the two other fields from COMBO-17 used in our analysis shows that fewer bright galaxies exist in the CDFS field (Wolf et al., 2003a). Further, a X-ray study revealed signs from the large-scale structure showing up as at least two spikes in the redshift distribution at $z = 0.67$ and $z = 0.73$ (Gilli et al., 2003).

The two fields that were used for the galaxy-galaxy lensing analysis contain large foreground clusters of galaxies. We checked how these foreground structures change the measurement and whether they introduce any bias. The expectation that foreground clusters should have no impact on the results was found to be fully justified.

The main results from the galaxy-galaxy lensing measurements are:

- A clear signal is detected. Averaged over all lens galaxies, the best-fit velocity dispersion of L_* -galaxies is $\sigma_* = (172 \pm 14) \text{ km s}^{-1}$ and the index η in the Tully-Fisher/Faber-Jackson relation $\sigma_* \propto L_*^\eta$ is best fit by $\eta = 0.36 \pm 0.07$. The errorbars are 1- σ limits in both cases. Both parameters show some evidence for a type-dependence such that early-type or luminous galaxies have larger σ_* and smaller η than late-type or faint galaxies.
- The best-fit velocity dispersion σ_* is a function of physical separation over which lens-source pairs are considered. Assuming that this velocity dispersion can directly be interpreted as averaged velocity dispersion of the lens galaxies without any contribution from e.g. surrounding group or cluster halos, this would imply that galaxies are not isothermal. Instead, the density profile declines faster than isothermal outside of at least $200h^{-1} \text{ kpc}$. In the inner $100h^{-1} \text{ kpc}$ the velocity dispersion of early-type or luminous galaxies might even be rising. Such a rise is predicted if galaxies can be described by NFW profiles. However, it still has to be tested if the peak of the velocity dispersion occurs at a radius that is consistent with the expectations from the NFW model and if it really can be assigned to the density profiles of the galaxies or could as well be explained by the environment.
- An upper limit on the outer scale s_* in the truncated SIS model is detected. However, the outer scale appears to be surprisingly small, below $100h^{-1} \text{ kpc}$ at 2- σ confidence.
- Using the NFW model, the virial radius of the lens galaxies can be constrained, but not the concentration c . The best-fit virial radius is about $130h^{-1} \text{ kpc}$ for late-type or faint galaxies and about $280h^{-1} \text{ kpc}$ for early-type or luminous galaxies. The corresponding virial masses are $1.5 \times 10^{11} h^{-1} M_\odot$ and $1.5 \times 10^{12} h^{-1} M_\odot$, respectively. Again, the effect of the environment on these results has to be investigated.

With the results presented in this thesis, the data set from COMBO-17 is still far from being fully exploited. We already mentioned that we want to investigate the full data set in the

future. The increase in data volume will then also allow us to apply more detailed modeling. The next items to be addressed will be the question which role the environment plays and how the modeling by the NFW profile can be improved. The role of the environment can be investigated most simply by splitting the lens sample into two subsamples of galaxies in underdense and overdense regions. If the statistics are good enough we also plan to apply a parametrized model like that proposed by Guzik and Seljak (2002) that quantifies the contribution from surrounding group or cluster halos to the detected shear. The modeling with the NFW profile can still be improved because so far all galaxies are treated in the same way. However, because a dependence of the virial radius on the type or luminosity of the galaxies seems to exist, a parametrization of this dependence should be incorporated in the model. Because no dependence on the concentration c was found, it is well possible that another combination of two parameters than virial radius and concentration is better suited for the fit.

COMBO-17 allows us to study halos of galaxies at larger redshift than other existing surveys like the SDSS that provide comparable statistics and also give redshifts and spectral information. Combining the results from the SDSS which probes lens galaxies at $z < 0.2$ with our results from COMBO-17 could give interesting information on the evolution of dark matter halos of galaxies.

Galaxy-galaxy lensing has only been detected for the first time in 1996. Since then, it has become an important tool in studying dark matter halos of galaxies. Improved modeling and larger surveys including redshift and spectral information start to allow one to apply detailed modeling and to investigate the dependence of halo profiles and masses on e.g. galaxy type, luminosity or environment. First quantitative results are already available, e.g. from this thesis or from the SDSS. Upcoming and even larger surveys like the VIRMOS-Descart survey or the CFHT Legacy Survey and planned surveys on e.g. the VISTA telescope or the VLT Survey Telescope will be well suited for galaxy-galaxy lensing studies in the future. Therefore, it can be expected that our knowledge on dark matter halos of galaxies will improve substantially within the next years.

Bibliography

- Aaronson, M. and Mould, J. (1983). A distance scale from the infrared magnitude/H I velocity-width relation. IV - The morphological type dependence and scatter in the relation; the distances to nearby groups. *Astrophysical Journal*, 265:1–17.
- Baade, D., Meisenheimer, K., Iwert, O., Alonso, J., Amico, P., Augusteijn, T., Beletic, J., Bellemann, H., Benesch, W., Böhm, H., Bönhardt, H., Deiries, S., Delabre, B., Donaldson, R., Dupuy, C., Franke, O., Gerdes, R., Gimozzi, R., Grimm, B., Haddad, N., Hess, G., Klein, H., Lenzen, R., Lizon, J.-L., Mancini, D., Münch, N., Rahmer, G., Reyes, J., Robledo, E., and Silber, A. (1998a). The Wide Field Imager for the 2.2-m MPG/ESO Telescope: a Preview. *ESO Messenger*, 93:13–15.
- Baade, D., Meisenheimer, K., Iwert, O., Alonso, J., Augusteijn, T., Beletic, J., Bellemann, H., Benesch, W., Böhm, H., Bönhardt, H., Brewer, J., Deiries, S., Delabre, B., Donaldson, R., Dupuy, C., Franke, O., Gerdes, R., Gilliotte, A., Grimm, B., Haddad, N., Hess, G., Ihle, G., Klein, H., Lenzen, R., Lizon, J.-L., Mancini, D., Münch, N., Pizarro, A., Prado, P., Rahmer, G., Reyes, J., Richardson, R., Robledo, E., Sanchez, F., Silber, A., Sinclair, P., Wackermann, R., and Zaggia, S. (1998b). The Wide Field Imager for the 2.2-m MPG/ESO Telescope: First Views with a 67-Million-Facetter Eye. *ESO Messenger*, 95:15–17.
- Bartelmann, M. (1996). Arcs from a universal dark-matter halo profile. *Astronomy and Astrophysics*, 313:697–702.
- Bartelmann, M. and Schneider, P. (2001). Weak Gravitational Lensing. *Physics Reports*, 340:291.
- Bertin, E. and Arnouts, S. (1996). SExtractor: Software for source extraction. *Astronomy and Astrophysics Supplement Series*, 117:393–404.
- Bertin, G. (2000). *Dynamics of galaxies*. Dynamics of galaxies / Giuseppe Bertin. New York : Cambridge University Press, ISBN 0-521-47262-8, 2000.
- Bevington, P. R. and Robinson, D. K. (1992). *Data reduction and error analysis for the physical sciences*. New York: McGraw-Hill, —c1992, 2nd ed.
- Brainerd, T. G., Blandford, R. D., and Smail, I. (1996). Weak Gravitational Lensing by Galaxies. *Astrophysical Journal*, 466:623.

- Brown, M. L., Taylor, A. N., Bacon, D. J., Gray, M. E., Dye, S., Meisenheimer, K., and Wolf, C. (2003). The shear power spectrum from the COMBO-17 survey. *Monthly Notices of the Royal Astronomical Society*, 341:100–118.
- Bryan, G. L. and Norman, M. L. (1998). Statistical Properties of X-Ray Clusters: Analytic and Numerical Comparisons. *Astrophysical Journal*, 495:80.
- Bullock, J. S., Kolatt, T. S., Sigad, Y., Somerville, R. S., Kravtsov, A. V., Klypin, A. A., Primack, J. R., and Dekel, A. (2001). Profiles of dark haloes: evolution, scatter and environment. *Monthly Notices of the Royal Astronomical Society*, 321:559–575.
- Carroll, B. W. and Ostlie, D. A. (1996). *An introduction to modern astrophysics*. Reading, Mass. : Addison-Wesley Pub., c1996.
- Clowe, D. and Schneider, P. (2002). Wide field weak lensing observations of A1835 and A2204. *Astronomy and Astrophysics*, 395:385–397.
- Danziger, I. J. (1997). Dark Matter in Early-Type Galaxies. In *ASP Conf. Ser. 117: Dark and Visible Matter in Galaxies and Cosmological Implications*, page 28.
- de Blok, W. J. G., Bosma, A., and McGaugh, S. (2003). Simulating observations of dark matter dominated galaxies: towards the optimal halo profile. *Monthly Notices of the Royal Astronomical Society*, 340:657–678.
- de Vaucouleurs, G., de Vaucouleurs, A., Corwin, H. G., Buta, R. J., Paturel, G., and Fouque, P. (1991). *Third Reference Catalogue of Bright Galaxies*. Volume 1-3, XII, 2069 pp. 7 figs.. Springer-Verlag Berlin Heidelberg New York.
- dell’Antonio, I. P. and Tyson, J. A. (1996). Galaxy Dark Matter: Galaxy-Galaxy Lensing in the Hubble Deep Field. *Astrophysical Journal Letters*, 473:L17.
- Eke, V. R., Cole, S., and Frenk, C. S. (1996). Cluster evolution as a diagnostic for Omega. *Monthly Notices of the Royal Astronomical Society*, 282:263–280.
- Erben, T. (2000). *Applications of the weak gravitational lens effect*. PhD thesis, Ludwig-Maximilians-Universität München.
- Erben, T., Van Waerbeke, L., Bertin, E., Mellier, Y., and Schneider, P. (2001). How accurately can we measure weak gravitational shear? *Astronomy and Astrophysics*, 366:717–735.
- Faber, S. M. and Jackson, R. E. (1976). Velocity dispersions and mass-to-light ratios for elliptical galaxies. *Astrophysical Journal*, 204:668–683.
- Fioc, M. and Rocca-Volmerange, B. (1997). PEGASE: a UV to NIR spectral evolution model of galaxies. Application to the calibration of bright galaxy counts. *Astronomy and Astrophysics*, 326:950–962.

- Fischer, P., McKay, T. A., Sheldon, E., Connolly, A., Stebbins, A., Frieman, J. A., Jain, B., Joffe, M., Johnston, D., Bernstein, G., Annis, J., Bahcall, N. A., Brinkmann, J., Carr, M. A., Csabai, I., Gunn, J. E., Hennessy, G. S., Hindsley, R. B., Hull, C., Ivezić, Ž., Knapp, G. R., Limmongkol, S., Lupton, R. H., Munn, J. A., Nash, T., Newberg, H. J., Owen, R., Pier, J. R., Rockosi, C. M., Schneider, D. P., Smith, J. A., Stoughton, C., Szalay, A. S., Szokoly, G. P., Thakar, A. R., Vogeley, M. S., Waddell, P., Weinberg, D. H., York, D. G., and The SDSS Collaboration (2000). Weak Lensing with Sloan Digital Sky Survey Commissioning Data: The Galaxy-Mass Correlation Function to $1 \text{ H}^{-1} \text{ Mpc}$. *Astronomical Journal*, 120:1198–1208.
- Gilli, R., Cimatti, A., Daddi, E., Hasinger, G., Rosati, P., Szokoly, G., Tozzi, P., Bergeron, J., Borgani, S., Giacconi, R., Kewley, L., Mainieri, V., Mignoli, M., Nonino, M., Norman, C., Wang, J., Zamorani, G., Zheng, W., and Zirm, A. (2003). Tracing the large scale structure in the Chandra Deep Field South. *astro-ph/0304177*.
- Gray, M. E., Taylor, A. N., Meisenheimer, K., Dye, S., Wolf, C., and Thommes, E. (2002). Probing the Distribution of Dark Matter in the A901/902 Supercluster with Weak Lensing. *Astrophysical Journal*, 568:141–162.
- Griffiths, R. E., Casertano, S., Im, M., and Ratnatunga, K. U. (1996). Weak gravitational lensing around field galaxies in Hubble Space Telescope survey images. *Monthly Notices of the Royal Astronomical Society*, 282:1159–1164.
- Guzik, J. and Seljak, U. (2002). Virial masses of galactic haloes from galaxy-galaxy lensing: theoretical modelling and application to Sloan Digital Sky Survey data. *Monthly Notices of the Royal Astronomical Society*, 335:311–324.
- Heavens, A., Refregier, A., and Heymans, C. (2000). Intrinsic correlation of galaxy shapes: implications for weak lensing measurements. *Monthly Notices of the Royal Astronomical Society*, 319:649–656.
- Heidt, J., Appenzeller, I., Gabasch, A., Jäger, K., Seitz, S., Bender, R., Böhm, A., Snigula, J., Fricke, K. J., Hopp, U., Kümmel, M., Möllenhoff, C., Szeifert, T., Ziegler, B., Drory, N., Mehlert, D., Moorwood, A., Nicklas, H., Noll, S., Saglia, R. P., Seifert, W., Stahl, O., Sutorius, E., and Wagner, S. J. (2003). The FORS Deep Field: Field selection, photometric observations and photometric catalog. *Astronomy and Astrophysics*, 398:49–61.
- Heymans, C. and Heavens, A. (2003). Weak gravitational lensing: reducing the contamination by intrinsic alignments. *Monthly Notices of the Royal Astronomical Society*, 339:711–720.
- Hoekstra, H., Franx, M., Kuijken, K., Carlberg, R. G., and Yee, H. K. C. (2002). Lensing by galaxies in CNOC2 fields. *astro-ph/0211633*.

- Hoekstra, H., Franx, M., Kuijken, K., and Squires, G. (1998). Weak Lensing Analysis of CL 1358+62 Using Hubble Space Telescope Observations. *Astrophysical Journal*, 504:636.
- Hoessel, J. G., Gunn, J. E., and Thuan, T. X. (1980). The photometric properties of brightest cluster galaxies. I - Absolute magnitudes in 116 nearby Abell clusters. *Astrophysical Journal*, 241:486–492.
- Hudson, M. J., Gwyn, S. D. J., Dahle, H., and Kaiser, N. (1998). Galaxy-Galaxy Lensing in the Hubble Deep Field: The Halo Tully-Fisher Relation at Intermediate Redshift. *Astrophysical Journal*, 503:531.
- Jing, Y. P. (2002). Intrinsic correlation of halo ellipticity and its implications for large-scale weak lensing surveys. *Monthly Notices of the Royal Astronomical Society*, 335:L89–L93.
- Kaiser, N., Squires, G., and Broadhurst, T. (1995). A Method for Weak Lensing Observations. *Astrophysical Journal*, 449:460.
- Kinney, A. L., Calzetti, D., Bohlin, R. C., McQuade, K., Storchi-Bergmann, T., and Schmitt, H. R. (1996). Template Ultraviolet to Near-Infrared Spectra of Star-forming Galaxies and Their Application to K-Corrections. *Astrophysical Journal*, 467:38.
- Kronawitter, A., Saglia, R. P., Gerhard, O., and Bender, R. (2000). Orbital structure and mass distribution in elliptical galaxies. *Astronomy and Astrophysics Supplement Series*, 144:53–84.
- Longair, M. S., editor (1998). *Galaxy formation*.
- Luppino, G. A. and Kaiser, N. (1997). Detection of Weak Lensing by a Cluster of Galaxies at $Z = 0.83$. *Astrophysical Journal*, 475:20.
- Mao, S. and Schneider, P. (1998). Evidence for substructure in lens galaxies? *Monthly Notices of the Royal Astronomical Society*, 295:587.
- Maoz, D. and Rix, H. (1993). Early-Type Galaxies, Dark Halos, and Gravitational Lensing Statistics. *Astrophysical Journal*, 416:425.
- McKay, T. A., Sheldon, E. S., Johnston, D., Grebel, E. K., Prada, F., Rix, H., Bahcall, N. A., Brinkmann, J., Csabai, I., Fukugita, M., Lamb, D. Q., and York, D. G. (2002). Dynamical Confirmation of Sloan Digital Sky Survey Weak-lensing Scaling Laws. *Astrophysical Journal Letters*, 571:L85–L88.
- McKay, T. A., Sheldon, E. S., Racusin, J., Fischer, P., Seljak, U., Stebbins, A., Johnston, D., Frieman, J. A., Bahcall, N., Brinkmann, J., Csabai, I., Fukugita, M., Hennessy, G. S., Ivezić, Z., Lamb, D. Q., Loveday, J., Lupton, R. H., Munn, J. A., Nichol, R. C., Pier, J. R., and York, D. G. (2001). Galaxy Mass and Luminosity Scaling Laws Determined by Weak Gravitational Lensing. *astro-ph/0108013*.

- Milgrom, M. (1983a). A modification of the Newtonian dynamics - Implications for galaxies. *Astrophysical Journal*, 270:371–389.
- Milgrom, M. (1983b). A Modification of the Newtonian Dynamics - Implications for Galaxy Systems. *Astrophysical Journal*, 270:384.
- Milgrom, M. (1983c). A modification of the Newtonian dynamics as a possible alternative to the hidden mass hypothesis. *Astrophysical Journal*, 270:365–370.
- Moore, B., Ghigna, S., Governato, F., Lake, G., Quinn, T., Stadel, J., and Tozzi, P. (1999). Dark Matter Substructure within Galactic Halos. *Astrophysical Journal Letters*, 524:L19–L22.
- Narayan, R. and Bartelmann, M. (1999). Gravitational lensing. In *Formation of Structure in the Universe*, page 360.
- Navarro, J. F., Frenk, C. S., and White, S. D. M. (1995). Simulations of X-ray clusters. *Monthly Notices of the Royal Astronomical Society*, 275:720–740.
- Navarro, J. F., Frenk, C. S., and White, S. D. M. (1996). The Structure of Cold Dark Matter Halos. *Astrophysical Journal*, 462:563.
- Navarro, J. F., Frenk, C. S., and White, S. D. M. (1997). A Universal Density Profile from Hierarchical Clustering. *Astrophysical Journal*, 490:493.
- Peacock, J. A., Cole, S., Norberg, P., Baugh, C. M., Bland-Hawthorn, J., Bridges, T., Cannon, R. D., Colless, M., Collins, C., Couch, W., Dalton, G., Deeley, K., De Propris, R., Driver, S. P., Efstathiou, G., Ellis, R. S., Frenk, C. S., Glazebrook, K., Jackson, C., Lahav, O., Lewis, I., Lumsden, S., Maddox, S., Percival, W. J., Peterson, B. A., Price, I., Sutherland, W., and Taylor, K. (2001). A measurement of the cosmological mass density from clustering in the 2dF Galaxy Redshift Survey. *Nature*, 410:169–173.
- Pickles, A. J. (1998). A Stellar Spectral Flux Library: 1150-25000 Å. *Publications of the Astronomical Society of the Pacific*, 110:863–878.
- Prada, F., Vitvitska, M., Klypin, A., Hotzman, J. A. Schlegel, D. J., Grebel, E. K., Rix, H.-W., Brinkmann, J., McKay, T. A., and Csabai, I. (2003). Observing the dark matter density profile of isolated galaxies. *astro-ph/0301360*.
- Press, W. H., Teukolsky, S. A., Vetterling, W. T., and Flannery, B. P. (1992). *Numerical recipes in C. The art of scientific computing*. Cambridge: University Press, —c1992, 2nd ed.
- Rix, H., de Zeeuw, P. T., Cretton, N., van der Marel, R. P., and Carollo, C. M. (1997). Dynamical Modeling of Velocity Profiles: The Dark Halo around the Elliptical Galaxy NGC 2434. *Astrophysical Journal*, 488:702–+.

- Sanders, R. H. and McGaugh, S. S. (2002). Modified Newtonian Dynamics as an Alternative to Dark Matter. *Annual Review of Astronomy and Astrophysics*, 40:263–317.
- Schirmer, M., Erben, T., Schneider, P., Pietrzynski, G., Gieren, W., Micol, A., and Pierfederici, F. (2003). GaBoDS: The Garching-Bonn Deep Survey – I. Anatomy of galaxy clusters in the background of NGC 300. *astro-ph/0305172*.
- Schlegel, D. J., Finkbeiner, D. P., and Davis, M. (1998). Maps of Dust Infrared Emission for Use in Estimation of Reddening and Cosmic Microwave Background Radiation Foregrounds. *Astrophysical Journal*, 500:525.
- Schneider, P. and Rix, H. (1997). Quantitative Analysis of Galaxy-Galaxy Lensing. *Astrophysical Journal*, 474:25.
- Seljak, U. (2002). Constraints on galaxy halo profiles from galaxy-galaxy lensing and Tully-Fisher/Fundamental Plane relations. *Monthly Notices of the Royal Astronomical Society*, 334:797–804.
- Smith, D. R., Bernstein, G. M., Fischer, P., and Jarvis, M. (2001). Weak-Lensing Determination of the Mass in Galaxy Halos. *Astrophysical Journal*, 551:643–650.
- Sofue, Y. and Rubin, V. (2001). Rotation Curves of Spiral Galaxies. *Annual Review of Astronomy and Astrophysics*, 39:137–174.
- Sofue, Y., Tutui, Y., Honma, M., Tomita, A., Takamiya, T., Koda, J., and Takeda, Y. (1999). Central Rotation Curves of Spiral Galaxies. *Astrophysical Journal*, 523:136–146.
- Swaters, R. A., Madore, B. F., van den Bosch, F. C., and Balcells, M. (2003). The Central Mass Distribution in Dwarf and Low Surface Brightness Galaxies. *Astrophysical Journal*, 583:732–751.
- Tully, R. B. and Fisher, J. R. (1977). A new method of determining distances to galaxies. *Astronomy and Astrophysics*, 54:661–673.
- Vanden Berk, D. E., Richards, G. T., Bauer, A., Strauss, M. A., Schneider, D. P., Heckman, T. M., York, D. G., Hall, P. B., Fan, X., Knapp, G. R., Anderson, S. F., Annis, J., Bahcall, N. A., Bernardi, M., Briggs, J. W., Brinkmann, J., Brunner, R., Burles, S., Carey, L., Castander, F. J., Connolly, A. J., Crocker, J. H., Csabai, I., Doi, M., Finkbeiner, D., Friedman, S., Frieman, J. A., Fukugita, M., Gunn, J. E., Hennessy, G. S., Ivezić, Ž., Kent, S., Kunszt, P. Z., Lamb, D. Q., Leger, R. F., Long, D. C., Loveday, J., Lupton, R. H., Meiksin, A., Merelli, A., Munn, J. A., Newberg, H. J., Newcomb, M., Nichol, R. C., Owen, R., Pier, J. R., Pope, A., Rockosi, C. M., Schlegel, D. J., Siegmund, W. A., Smee, S., Snir, Y., Stoughton, C., Stubbs, C., SubbaRao, M., Szalay, A. S., Szokoly, G. P., Tremonti, C., Uomoto, A., Waddell, P., Yanny, B., and Zheng, W. (2001). Composite Quasar Spectra from the Sloan Digital Sky Survey. *Astronomical Journal*, 122:549–564.

- Wilson, G., Kaiser, N., Luppino, G. A., and Cowie, L. L. (2001). Galaxy Halo Masses from Galaxy-Galaxy Lensing. *Astrophysical Journal*, 555:572–584.
- Wolf, C. (1999). *Vielfarben-Klassifikation in CADIS und die Suche nach Quasaren*. PhD thesis, Ruprecht-Karls-Universität Heidelberg.
- Wolf, C., Dye, S., Kleinheinrich, M., Meisenheimer, K., Rix, H.-W., and Wisotzki, L. (2001a). Deep BVR photometry of the Chandra Deep Field South from the COMBO-17 survey. *Astronomy and Astrophysics*, 377:442–449.
- Wolf, C., Meisenheimer, K., and Röser, H.-J. (2001b). Object classification in astronomical multi-color surveys. *Astronomy and Astrophysics*, 365:660–680.
- Wolf, C., Meisenheimer, K., Röser, H.-J., Beckwith, S. V. W., Chaffee, F. H., Fried, J., Hippelein, H., Huang, J.-S., Kümmel, M., von Kuhlmann, B., Maier, C., Phleps, S., Rix, H.-W., Thommes, E., and Thompson, D. (2001c). Multi-color classification in the calar alto deep imaging survey. *Astronomy and Astrophysics*, 365:681–698.
- Wolf, C., Meisenheimer, K., Rix, H.-W., Borch, A., Dye, S., and Kleinheinrich, M. (2003a). The COMBO-17 survey: Evolution of the galaxy luminosity function from 25 000 galaxies with $0.2 < z < 1.2$. *Astronomy and Astrophysics*, 401:73–98.
- Wolf, C., Wisotzki, L., Borch, A., Dye, S., Kleinheinrich, M., and Meisenheimer, K. (2003b). The evolution of faint AGN between $z \sim 1$ and $z \sim 5$ from the COMBO-17 survey. *astro-ph/0304072*.
- Wright, C. O. and Brainerd, T. G. (2000). Gravitational Lensing by NFW Halos. *Astrophysical Journal*, 534:34–40.
- Zaritsky, D., Smith, R., Frenk, C., and White, S. D. M. (1993). Satellites of spiral galaxies. *Astrophysical Journal*, 405:464–478.
- Zaritsky, D., Smith, R., Frenk, C., and White, S. D. M. (1997). More Satellites of Spiral Galaxies. *Astrophysical Journal*, 478:39.

Acknowledgements

Many people supported me during my work on this thesis. In particular, I thank Hans-Walter Rix and Peter Schneider who gave me the opportunity to work on this project. Further, Christian Wolf, Klaus Meisenheimer, Thomas Erben and Mischa Schirmer helped me with technical and scientific issues. Steffen Neumann supported and encouraged me when looking for a suitable PhD project and later helped me with lots of advice on all kinds of questions. With Bernd Lang I had interesting and fruitful discussions and he also reminded me of life outside the PhD work.

Of course I also have to thank the many people at the Max-Planck-Institute for Astronomy and at the University of Bonn for the good social environment and for helping me with all the little things.

Zusammenfassung

Inhalt dieser Arbeit ist die Untersuchung von dunklen Halos um Galaxien. Gegenwärtige Theorien der Galaxienentstehung sagen voraus, dass Galaxien in ausgedehnten Halos aus Dunkler Materie eingebettet sind, die deutlich grössere Ausmasse haben als die sichtbaren Teile der Galaxien. Diese Vorhersage durch Beobachtungen zu überprüfen ist schwierig, da die dunklen Halos – gemäss ihrer Definition – keinerlei Strahlung aussenden. Daher können sie nur durch ihre gravitative Wirkung untersucht werden. Zur Zeit sind zwei Methoden bekannt wie solche Untersuchungen auf Skalen von $100h^{-1}$ kpc oder grösser durchgeführt werden können. Diese nutzen entweder die Bewegungen von Satellitengalaxien um grössere Galaxien oder den schwachen Gravitationslinseneffekt. Diese grossen Skalen sind interessant, da die Simulationen zeigen, dass die dunklen Halos Ausdehnungen von mehreren hundert kpc haben. Ausserdem ist auf so grossen Skalen die leuchtende Materie vernachlässigbar, so dass es möglich ist, nur das Dichteprofil der Dunklen Materie zu untersuchen.

Wir wählen den schwachen Gravitationslinseneffekt als Methode in unseren Untersuchungen. Die Methode ist auch unter dem Namen *galaxy-galaxy lensing* bekannt. Der Linseneffekt hat den Vorteil gegenüber dem Studium der Satellitendynamik, dass keinerlei Annahmen über den dynamischen Zustand der Galaxien gemacht werden müssen, sondern dass die Verteilung der Dunklen Materie direkt untersucht werden kann. So wie die Untersuchung an Satellitengalaxien, können allerdings mit dem schwachen Linseneffekt dunkle Halos nur statistisch untersucht werden, d.h. für die Messung muss über mindestens Hunderte von Galaxien gemittelt werden. Dies macht die Interpretation der Ergebnisse entsprechend schwierig. Darüberhinaus stellt die Messung des schwachen Linseneffekts hohe Anforderungen an die Beobachtungsdaten, so dass das hier benutzte galaxy-galaxy lensing erst 1996 zum ersten Mal gemessen wurde. Wir benutzen Daten aus dem COMBO-17 Survey¹, der für diese Art von Untersuchung hervorragend geeignet ist. Der herausragendste Vorteil von COMBO-17 sind tiefe Beobachtungen in einem grossen Gesichtsfeld. Dadurch werden wir schliesslich Linsengalaxien bei Rotverschiebungen um $z = 0.5$ in vier Feldern mit einer Gesamtfläche von einem Quadratgrad Gesamtfläche untersuchen können. Allerdings benutzen wir in dieser Arbeit erst die Hälfte dieser Fläche. Zusätzlich liefert COMBO-17 photometrische Rotverschiebungen von insgesamt 17 optischen Filtern sowie eine spektrale Klassifikation der Galaxien. Besonders tiefe Rotaufnahmen bei den besten Beobachtungsbedingungen werden zur genauen Messung der Formen und Elliptizitäten der Hintergrundgalaxien genutzt.

Dieser herausragende Datensatz ist der erste Datensatz eines repräsentativen Himmelsausschnitts, der geeignet ist für Untersuchungen des schwachen Linseneffekts und der ausserdem Rotverschiebungen und Farbinformationen bietet. Bisher konnten nur Surveys mit geringer Tiefe solche Informationen bereitstellen. Daher werden wir mit COMBO-17

¹Classifying Objects by Medium-Band Observations in 17 filters

in der Lage sein, bereits durchgeführte Untersuchungen an lokalen Galaxien auf Galaxien bei höherer Rotverschiebung zu übertragen. Die interessantesten Fragen in diesen Untersuchungen betreffen nicht nur die Dichteprofile der dunklen Halos, sondern auch die Verbindung zwischen den leuchtkräftigen Teilen von Galaxien und ihren dunklen Halos. Wir werden den Zusammenhang zwischen dunklen Halos und der Leuchtkraft bzw. dem Spektraltyp von Galaxien untersuchen.

In Untersuchungen zum schwachen Gravitationslinseneffekt müssen Elliptizitäten von Hintergrundgalaxien sehr genau gemessen werden. Normalerweise sind diese Hintergrundgalaxien klein und umfassen nur wenige Pixel auf CCD-Bildern. Ausserdem werden sie durch z.B. ungenaues Fokussieren, Nachführfehler des Teleskops und insbesondere durch die Atmosphäre verzerrt. Spezielle Programme sind verfügbar zur Korrektur dieser Verzerrungen. Jedoch ist bisher noch nicht an beobachteten Daten – sondern nur an simulierten – die Qualität der Korrekturen und die Zuverlässigkeit der Elliptizitätsmessung überprüft worden. Wir werden mehrfache Beobachtungen eines der COMBO-17 Felder benutzen, um die Elliptizitätsmessungen von unabhängigen Summenbildern zu überprüfen und dadurch die Zuverlässigkeit der Elliptizitätsmessung überprüfen.

Ergebnisse

Zuverlässigkeit der Elliptizitätsmessung

Den grössten Einfluss auf die Zuverlässigkeit von Elliptizitätsmessungen hat das seeing, d.h. die Unruhe der Atmosphäre zum Zeitpunkt der Beobachtung. Allerdings werden durch schlechteres seeing die Elliptizitätsmessungen einzelner Objekte nicht in der gleichen Weise beeinflusst. Kleine oder schwache Objekte sind stärker betroffen, ebenso solche, für die eine grössere Elliptizität gemessen wurde (die dann meistens durch die ungenauere Messung bzw. Korrektur vergrössert ist). Ausserdem ist die Formmessung für die Objekte unzuverlässiger, die einen grösseren Korrekturfaktor haben. Diese Zusammenhänge können genutzt werden um die Formmessungen der verschiedenen Galaxien zu gewichten, wodurch sich die Signifikanz der Ergebnisse verbessern lässt. Wir haben verschiedene Schemata untersucht wie Gewichte zugewiesen werden können. Am erfolgreichsten ist eine Gewichtung aufgrund des Signal-zu-Rausch-Verhältnisses und des angewandten Korrekturfaktors eines Objekts. Dieses Schema verkleinert die Fehlerbalken in der Messung des galaxy-galaxy lensings im Vergleich zu keiner Gewichtung. Ausserdem sind die Messungen des galaxy-galaxy lensings von unabhängigen Datensätzen in guter Übereinstimmung zueinander, wenn diese Gewichtung benutzt wird.

Eigenschaften der dunklen Halos von Galaxien

Wir haben drei Modelle benutzt, mit denen die Dichteverteilung von Galaxien beschrieben werden kann: erstens die isotherme Sphäre die sich durch eine konstante Geschwindigkeitsdispersion unabhängig vom Radius auszeichnet, zweitens die isotherme Sphäre mit äusserem

Abschneideradius, bei der die Geschwindigkeitsdispersion nach aussen abfällt, und drittens das sogenannte Navarro-Frenk-White (NFW) Profil, bei dem die Geschwindigkeitsdispersion im innersten Bereich der Galaxien ansteigt, dann aber nach aussen weniger stark als für die isotherme Sphäre mit Abschneideradius abfällt. Die wichtigsten Ergebnisse sind im folgenden zusammengefasst:

- Im Fall der isothermen Sphäre ergibt sich eine Geschwindigkeitsdispersion von Galaxien typischer Leuchtkraft ($= 10^{10}$ Sonnenleuchtkräfte) von $\sigma_* = (172 \pm 14) \text{ km s}^{-1}$. Zwischen Geschwindigkeitsdispersion und Leuchtkraft wurde ein Zusammenhang gemäss $\sigma_v \propto L^\eta$ angenommen und $\eta = 0.36 \pm 0.07$ bestimmt. Die angegebenen Fehlerbalken sind jeweils $1\text{-}\sigma$ Intervalle. Beide Parameter zeigen Abhängigkeiten vom Spektraltyp und der Leuchtkraft der Galaxien – leuchtkräftigere Galaxien oder frühere Spektraltypen haben grössere Geschwindigkeitsdispersionen und ein kleineres η , d.h. eine geringere Abhängigkeit der Geschwindigkeitsdispersion von der Leuchtkraft als leuchtschwächere Galaxien oder späte Galaxientypen.
- Die gefundene Geschwindigkeitsdispersion ist nicht unabhängig vom Radius. Sollte dieses Ergebnis unmittelbar als Aussage über die Geschwindigkeitsdispersion von einzelnen Galaxien interpretierbar sein, dann wäre damit die isotherme Sphäre als geeignetes Modell zur Beschreibung der dunklen Halos ausgeschlossen. Die Geschwindigkeitsdispersion nimmt ab mindestens $200h^{-1} \text{ kpc}$ ab. In den inneren $100h^{-1} \text{ kpc}$ gibt es Hinweise, dass sie sogar ansteigt für leuchtkräftige Galaxien oder frühe Spektraltypen. Ein solcher Anstieg ist zwar für das NFW Profil vorhergesagt, allerdings muss noch überprüft werden, ob der Radius, bei dem die maximale Geschwindigkeitsdispersion erreicht wird, mit den theoretischen Erwartungen übereinstimmt. Ausserdem wäre es noch denkbar, dass der Anstieg nicht auf die Dichteprofile der Galaxien selbst zurückzuführen ist, sondern durch z.B. dunkle Halos von Galaxiengruppen oder -haufen, in denen sich diese Galaxien befinden könnten, erklärt werden kann.
- Eine obere Schranke für den Abschneideradius der isothermen Sphäre konnte gemessen werden. Dieser ist allerdings überraschend klein, kleiner als $100h^{-1} \text{ kpc}$ mit $2\text{-}\sigma$ Konfidenz.
- Bei Benutzung des NFW Profils kann der Virialradius der Galaxien bestimmt werden. Für leuchtschwache Galaxien oder späte Galaxientypen ergeben sich Werte um $130h^{-1} \text{ kpc}$ und dementsprechend Virialmassen von $1.5 \times 10^{11}h^{-1} M_\odot$. Für leuchtkräftige Galaxien und frühe Galaxientypen ergeben sich Virialradien von ca. $280h^{-1} \text{ kpc}$ und Virialmassen um $1.5 \times 10^{12}h^{-1} M_\odot$.

Ausblick

Die dargestellten Ergebnisse über dunkle Halos von Galaxien schöpfen das Potential von COMBO-17 noch nicht vollständig aus. Daher sind weitere Arbeiten mit diesem Datensatz geplant. Bisher wurde nur der halbe Datensatz verwendet – teilweise aufgrund noch

nicht abgeschlossener Datenreduktion. In Zukunft soll der vollständige Datensatz untersucht werden. Damit wird es auch möglich sein, detailliertere Modelle zur Beschreibung der dunklen Halos von Galaxien anzuwenden. Zwei Verbesserungen der Modellierung sind insbesondere hervorzuheben: die Berücksichtigung der Umgebung von Linsengalaxien und eine verbesserte Anwendung des NFW Profils auf die Daten. Zur Untersuchung des Einflusses der Umgebung von Galaxien können zunächst die Linsengalaxien in zwei Untergruppen aufgeteilt werden. Dann kann festgestellt werden wie sich die Ergebnisse von Galaxien in dichten und weniger dichten Umgebungen unterscheiden. Falls die Grösse des Datensatzes ausreicht, kann ausserdem versucht werden, den Beitrag der Umgebung zum Linsensignal durch ein geeignetes Modell zu parametrisieren. Das angewandte Modell des NFW Profils kann derart verbessert werden, dass ein Zusammenhang zwischen den Parametern des Modells und z.B. der Leuchtkraft oder dem Spektraltyp der Galaxien eingebaut wird.

Ein Vergleich der Ergebnisse von COMBO-17 zu solchen von anderen Datensätzen wie dem Sloan Digital Sky Survey, die Galaxien bei kleinerer Rotverschiebung untersuchen, könnte interessante Erkenntnisse über die Entwicklung der dunklen Halos von Galaxien bringen. Das galaxy-galaxy lensing wurde erstmals erst 1996 gemessen. Seitdem ist es zu einem wichtigen Instrument in der Untersuchung dunkler Halos von Galaxien geworden. Verbesserte Modelle und umfangreichere Datensätze, die auch Rotverschiebungs- und Farbinformation bereitstellen, erlauben es nun, dunkle Halos von Galaxien in Abhängigkeit von deren Leuchtkraft, Spektraltyp oder Umgebung zu untersuchen. Erste Ergebnisse sind inzwischen verfügbar, z.B. von dieser Arbeit oder vom Sloan Digital Sky Survey. Bereits gestartete, grössere Surveys wie z.B. der VIRMOS-Descart Survey oder der CFHT Legacy Survey, aber auch geplante Surveys an z.B. dem VISTA Teleskop oder dem VLT Survey Teleskop werden auch für diese Art von Untersuchung hervorragend geeignet sein. Daher ist zu erwarten, dass sich unsere Kenntniss über die Struktur dunkler Halos von Galaxien in den nächsten Jahren noch erheblich verbessern wird.

Lebenslauf

Name	Martina Kleinheinrich
Anschrift	Wilhelm-Blum Strasse 6 69120 Heidelberg
Geburtsdatum	9. Mai 1974
Geburtsort	Rheda-Wiedenbrück

1980-1984	Grundschule <i>Bolandschule</i> , Herzebrock-Clarholz
1984-1993	Einstein-Gymnasium, Rheda-Wiedenbrück
Juni 1993	Abitur
1993-1998	Studium der Physik und Mathematik an der Universität Bielefeld
November 1998	Abschluss des Studiums mit der Ersten Staatsprüfung für die Lehrämter für die Sekundarstufe II und für die Sekundarstufe I
2000-2001	Beginn der Promotion am Max-Planck-Institut für Astronomie, Heidelberg
2001-2003	Fortführung der Promotion an der Rheinischen Friedrich-Wilhelms-Universität Bonn

